EFFECT OF FORCED CONVECTION AND COMPRESSIBILITY ON TRANSIENT MELTING BEHAVIOR OF PCM IN A CAVITY

A THESIS SUBMITTED TO
THE GRADUATE SCHOOL OF NATURAL AND APPLIED SCIENCES
OF
MIDDLE EAST TECHNICAL UNIVERSITY

BY

HOUMAN FARSHINEH ADL

IN PARTIAL FULFILLMENT OF THE REQUIREMENTS
FOR
THE DEGREE OF DOCTOR OF PHILOSOPHY
IN
MECHANICAL ENGINEERING

AUGUST 2025

Approval of the thesis:

EFFECT OF FORCED CONVECTION AND COMPRESSIBILITY ON TRANSIENT MELTING BEHAVIOR OF PCM IN A CAVITY

submitted by **HOUMAN FARSHINEH ADL** in partial fulfillment of the requirements for the degree of **Doctor of Philosophy in Mechanical Engineering, Middle East Technical University** by,

Prof. Dr. Naci Emre Altun
Dean, Graduate School of **Natural and Applied Sciences** ________________

Prof. Dr. Serkan Dağ
Head of the Department, **Mechanical Engineering** ________________

Assoc. Prof. Dr. Özgür Bayer
Supervisor, **Mechanical Engineering, METU** ________________

Examining Committee Members:

Prof. Dr. Cüneyt Sert
Mechanical Engineering, METU ________________

Assoc. Prof. Dr. Özgür Bayer
Mechanical Engineering, METU ________________

Assist. Prof. Dr. Altuğ Özçelikkale
Mechanical Engineering, METU ________________

Prof. Dr. Murat Köksal
Mechanical Engineering, Hacettepe University ________________

Prof. Dr. H. Tuba Okutucu Özyurt
Energy Institute, ITU ________________

Date: 27.08.2025

I hereby declare that all information in this document has been obtained and presented in accordance with academic rules and ethical conduct. I also declare that, as required by these rules and conduct, I have fully cited and referenced all material and results that are not original to this work.

Name Last name : Houman Farshineh Adl

Signature :

ABSTRACT

EFFECT OF FORCED CONVECTION AND COMPRESSIBILITY ON TRANSIENT MELTING BEHAVIOR OF PCM IN A CAVITY

Farshineh Adl, Houman
Doctor of Philosophy, Mechanical Engineering
Supervisor: Assoc. Prof. Dr. Özgür Bayer

August 2025, 141 pages

Improving heat transfer rates enhances the performance of devices that dissipate excess heat or require heat storage. Among the available options, phase change material (PCM) possesses advantageous thermal properties but exhibits comparatively slow melting rates, a limitation that the present study aims to mitigate. Both experimental and numerical studies are conducted using a cavity (generic domain) filled with PCM to assess forced convection induced by mixing the liquid PCM at rotational speeds of 5, 25, and 100 rpm. The experimental work focuses on the effect of forced convection, while the numerical analyses evaluate the compressibility effect. In numerical analyses, the enthalpy-porosity model is applied, utilizing either the Boussinesq approximation or the volume of fluid (VoF) method. The VoF method models the compressibility effect, enabling observation of the close contact melting (CCM) phenomenon. At higher rotational speeds, the melting duration is reduced by approximately 22%, to 32 hours, and the liquid fraction at steady state is increased by as much as 14%, resulting in complete PCM melting compared to the non rotating case. Mixing also decreased temperature gradients inside the domain, lowering peak temperature from $68°C$ to $45°C$. At lower rotational speeds, melting duration is decreased by only about 10% with a negligible change in liquid fraction at steady state. The effect of compressibility on PCM melting characteristics, when CCM is observable, is studied numerically. Using the Boussinesq approximation instead of the VoF method results in an unrealistic overestimation of the melting time by a factor of eight.

Keywords: phase change material, forced convection, melting time, compressibility

ÖZ

ZORLANMIŞ TAŞINIM VE SIKIŞTIRILABİLİRLİĞİN BİR KAVİTEDEKİ FAZ DEĞİŞİM MALZEMESİNİN GEÇİCİ ERİME DAVRANIŞI ÜZERİNDEKİ ETKİSİ

Farshineh Adl, Houman
Doktora, Makina Mühendisliği
Tez Yöneticisi: Doç. Dr. Özgür Bayer

Ağustos 2025, 141 sayfa

Isı transfer hızının iyileştirilmesi, fazla ısıyı dağıtan veya ısı depolaması gerektiren cihazların etkisini artırmaktadır. Faz değiştiren malzemeler (FDM) avantajlı ısıl özelliklere sahiptir ancak nispeten yavaş erime hızlarına sahiptir ve mevcut çalışma söz konusu dezavantajı en aza indirmeyi amaçlamaktadır. Hem deneysel hem de sayısal çalışmalar, 5, 25 ve 100 rpm dönüş hızlarında sıvı FDM'nin karıştırılmasıyla tetiklenen zorlanmış konveksiyonu incelemek için, FDM ile doldurulmuş bir kavite kullanılarak gerçekleştirilmiştir. Deneysel çalışma zorlanmış konveksiyonun etkisine odaklanırken, sayısal analizler sıkıştırılabilirlik etkisini incelemektedir. Sayısal analizlerde Boussinesq yaklaşımı veya akışkan hacmi (VoF) yöntemi kullanılarak entalpi-gözeneklilik modeli uygulanmıştır. VoF yöntemi, sıkıştırılabilirlik etkisini modelleyerek yakın temas erimesi (CCM) fenomeninin gözlemlenmesini sağlar. Sonuçlar, daha yüksek dönme hızlarında erime süresinin yaklaşık %22 oranında azaltılarak 32 saate düşürülebileceğini göstermektedir. Ek olarak kararlı durumdaki sıvı oranı, tüm FDM'nin erimesiyle, karıştırma olmayan senaryoya kıyasla %20 oranında artmaktadır. Karıştırıcı dahil edildiğinde sıcaklık gradyanları azalarak tepe kritik sıcaklık $68°C$'den $45°C$'ye düşmektedir. Bununla birlikte, düşük dönme hızlarında zorlanmış konveksiyonun etkisi azalmakta, bu da erime süresinde yalnızca yaklaşık %10'luk bir azalma ve kararlı durumdaki sıvı oranında ihmal edilebilir bir değişiklikle sonuçlanmaktadır. CCM’nin gözlemlenebilir olduğu durum için sıkıştırılabilirliğin FDM erime karakteristiği üzerindeki etkisi sayısal olarak incelenmiştir. VoF yöntemi yerine Boussinesq yaklaşımı kullanıldığında, erime süresinin gerçekçi olmayan şekilde sekiz kat fazla tahmin edildiği gözlemlenmiştir.

Anahtar Kelimeler: faz değiştiren malzemeler, zorlanmış taşınım, erime süresi, sıkıştırılabilirlik

To My Father

ACKNOWLEDGMENTS

The author wishes to express profound gratitude to his supervisor, Assoc. Prof. Dr. Özgür Bayer, for the exemplary guidance, consistent support, constructive criticism, and valuable insights offered throughout this research endeavor. His encouragement has been a source of strength during difficult periods, and for this, the author extends sincere appreciation.

The author would like to express his sincere gratitude to his family for their unwavering support. He is profoundly appreciative of his esteemed wife, whose encouragement and love have been instrumental in providing him with the strength he needs throughout this undertaking. Furthermore, he extends his gratitude to his mother and sister, whose prayers and sacrifices have consistently been a source of inspiration.

The technical assistance provided by Mr. Mustafa Yalçin, Mr. Mehdi Dehshat, Mr. Deniz Alp Yilmaz, and Mr. Mohsen Baghaei has been immensely valuable. Their support has significantly contributed to achieving the objectives.

TABLE OF CONTENTS

LIST OF TABLES

TABLES

LIST OF FIGURES

FIGURES

LIST OF ABBREVIATIONS

ABBREVIATIONS

2D	two-dimensional
3D	three-dimensional
AC	alternating current
API	American Petroleum Institute
CCM	close contact melting
CF	correction factor
CFD	computational fluid dynamics
CFL	Courant–Friedrichs–Lewy
CPU	central processing unit
DC	direct current
DSC	differential scanning calorimetry
EV	electric vehicle
FVM	finite volume method
HMI	human-machine interface
LHTES	latent heat thermal energy storage
MU	mixer usefulness
NR	non rotating
O&M	operation & maintenance
PCM	phase change material

PRESTO!	PREssure STaggering Option
R	rotating
SG	specific gravity
SI	international system of units
SIMPLE	semi-implicit method for pressure-linked equations
SSR	solid state relay
STP	stepper motor driver module
TES	thermal energy storage
TGA	thermogravimetric analysis
TMP	thermocouple input module
TMS	thermal management system
VoF	volume of fluid
VP	virtual plane

LIST OF SYMBOLS

SYMBOLS

Symbol	Name	Unit
a	One side dimension of cavity	mm
b	height of air domain	mm
C_{mush}	mushy zone constant	$kg/(m^3.s)$
c_p	specific heat capacity at constant pressure	$kJ/(kg.K)$
D	diameter of expansion tube	mm
f	liquid fraction	$-$
Ω_n	relative uncertainty of n^{th} parameter	$-$
$\boldsymbol{g}$	gravitational acceleration	m/s^2
h	convective heat transfer coefficient	$W/(m^2.K)$
H	height of expansion tube	mm
i	specific enthalpy	kJ/kg
I	current	A
k	thermal conductivity	$W/(m.K)$
L	latent heat	kJ/kg
m	mass	kg
N	rotational speed	rpm
P	pressure	kPa
Q	total heat transferred	kJ
$\dot{Q}$	heat transfer rate	W
R	overall uncertainty, radius of cylindrical domain	$-, mm$

$S_{\boldsymbol{U}}$	source term in momentum equation	$kg/(m^2.s^2)$
t	time, thickness	s, mm
T	temperature	$°C$
U	voltage	V
$\boldsymbol{U}$	velocity	m/s
V	volume	m^3
w	width	m
W	total work	kJ
$\dot{W}$	power	W
$x, y, and\ z$	3D Cartesian coordinate axes	mm
α	volume fraction	$-$
β	thermal expansion coefficient	$1/K$
ρ	density	kg/m^3
δ	thickness	m

LIST OF SUBSCRIPTS

SUBSCRIPTS

aux	auxiliary heater
n	axial position n, n^{th} fluid
c	cavity
et	expansion tube
$expanded$	expanded
h	heater
i	inner
$latent$	latent
l	liquid, liquidus
m	measured
mix	mixer
NR	non rotating
o	outer
ref	reference
R	rotating
$sensible$	sensible
s	solid, solidus
tot	total
w	wall
$water$	water

CHAPTER 1

INTRODUCTION

In light of the global energy crisis, the utilization of devices with higher power densities and efficiencies has become imperative to ensure sustainable energy use [1]. However, an increase in power densities would lead to higher operating temperatures, which, without a properly designed thermal management system (TMS), can cause considerable damage to the operating system [2]. In specific industries, such as electronics, it is essential to remove waste heat from the system to prevent an excessive rise in temperature. Undesirable temperature elevations in such applications lead to increased operation & maintenance (O&M) costs [3–6]. As an example, lithium-ion batteries, which are extensively utilized in electric vehicles (EVs), can produce heat that may cause failure or even explosion [7, 8]. Some methods have been proposed to remove heat, such as using air, water, or hybrid cases [9].

An effective TMS is essential for enabling technologies that can meet rising energy demand and support the transition to sustainable energy sources. By increasing energy demand, the world will face problems such as the energy crisis [10]. Nowadays, switching to renewable energy is a trend to mitigate the energy crisis with minimal shortcomings in energy availability. Switching to renewable energy sources is not without its challenges, including the intermittency in energy provision that is inherent to renewable energy sources. Therefore, researchers have developed the concept of utilizing energy storage to balance energy supply and demand, thereby compensating for the depletion of conventional energy sources [11, 12]. Energy is primarily stored in the form of either electrical or thermal. Although electricity offers a promising outlook, the utilization of batteries imposes a considerably high cost on the overall system [13]. The high price of electrical energy storage units makes them impractical in many applications, especially on a large scale. However, thermal energy storage (TES) units would be cost-effective, with expenses reported to be as low as one-sixth of those for systems of the same size that store energy in electrical form [14]. Among TES options, latent heat storage with phase change material (PCM) has attracted significant interest because it can store large amounts of thermal energy at nearly constant temperatures in small sizes [15].

1.1 PCM Types

PCM, regarding its physical phase transitions, is categorized into four types, namely solid-solid, solid-liquid, solid-gas, and liquid-gas. For simplicity and because of their similar behavior, the solid-gas and liquid-gas PCMs are combined into one section in Figure 1.1, which illustrates the various types of PCMs.

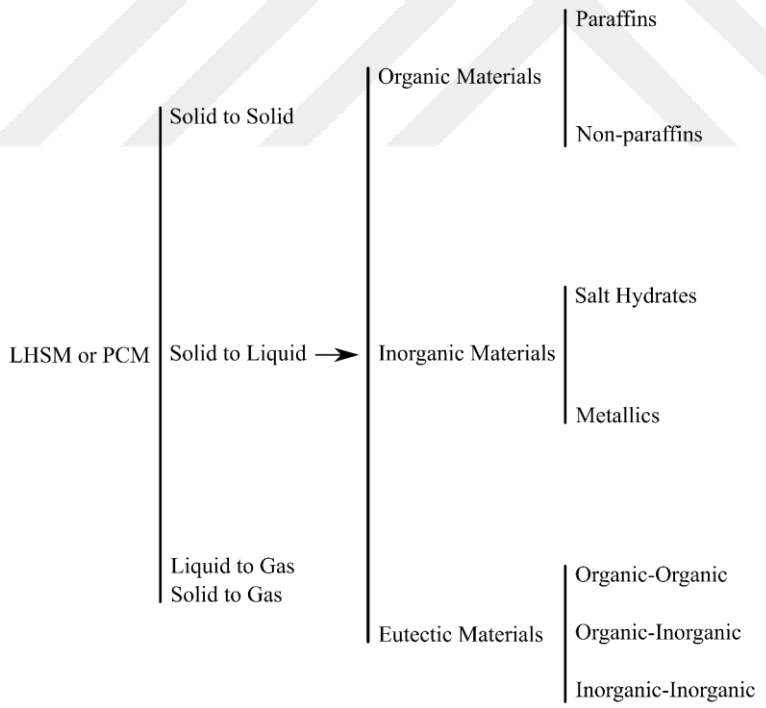

Figure 1.1 Classification of PCMs [16, 17]

Although solid-solid PCMs have more straightforward design requirements and exhibit low expansion rates, tailoring them to meet the specific needs of the end user presents considerable challenges due to the particular transition temperature they necessitate during the phase change from one crystalline form to another [18]. Solid-gas and liquid-gas PCMs possess relatively high latent heat. However, their significant volume change during phase transition renders them impractical and complicated, as they require pressurized containers for operation [19]. Despite their lower latent heat of fusion, solid-liquid PCMs are still economically viable [20].

Solid-liquid PCM falls into two main categories, which are inorganic and organic. Inorganic materials offer relatively high latent heat and thermal conductivity. However, several drawbacks limit their practical use, including corrosiveness, subcooling, and phase segregation [21]. Although organic materials are physically and chemically stable, their low thermal conductivity (approximately 0.2 $W/(m.K)$) slows down the heat transfer [22]. Within the organic category, two primary groups are available. One group includes paraffin-based materials, and the other consists of fatty acids as nonparaffin alternatives. Although paraffins have some drawbacks, such as an undefined melting temperature [23] and lower enthalpy of phase change [24], they cost about one-third of what fatty acids do [11, 25], making paraffins more economically practical. In the current study, considering the comparisons mentioned, paraffin is chosen.

Considering the different thermal properties of PCM like paraffins, salt hydrates, and fatty acids, accurate modeling of phase change behavior is crucial for precise characterization and proper integration into thermal energy systems. Precise representation of melting behavior requires mathematical modeling that can capture heat transfer and phase interface development. Among the available options, analytical models provide closed-form solutions based on simplified assumptions, while numerical models apply computational techniques to resolve complex geometries and dynamic conditions. Both modeling approaches are tools for performance evaluation and design optimization in PCM-based thermal systems.

1.2 Melting Characterization

As a first approach, analytical modeling depends on precise solutions to simplified forms of the governing heat transfer equations. Analytical models typically assume one dimensional heat conduction, constant thermophysical properties, and idealized boundary conditions such as fixed temperature or heat flux. Under such assumptions, it is feasible to derive closed-form solutions that describe the temperature distribution and phase front progression during melting, thereby providing both valuable physical insights and computational convenience. Nonetheless, the accuracy of analytical models diminishes significantly when applied to real-world systems. The primary limitations stem from their inability to account for natural convection, variable material properties, multidimensional geometries, and time-dependent boundary conditions [26]. Consequently, analytical methods are confined to highly idealized scenarios and provide limited predictive power for engineering applications.

To overcome the limitations set by analytical methods, numerical modeling techniques have become the preferred method for simulating PCM melting in real-world environments. Numerical approaches discretize the governing partial differential equations through finite element, finite difference, or finite volume schemes. They can handle complex geometries, non-linear boundary conditions, and the dynamic behavior of the phase interface, offering much greater flexibility and accuracy than analytical models. The most frequently used numerical methods for modeling PCM include the effective heat capacity method, interface tracking techniques, and the enthalpy porosity approach.

The effective heat capacity method captures latent heat by adjusting the specific heat within a certain temperature range, enabling phase change to be modeled in the energy equation without explicitly tracking the interface. Although the effective heat capacity method offers ease of implementation and reduced computational effort, it often results in diffused phase boundaries and limited resolution near the melting front [27]. In contrast, interface tracking methods, such as moving mesh and level set schemes, explicitly follow the solid–liquid boundary, thereby achieving higher accuracy in resolving interface dynamics. However, interface tracking methods require intensive computational effort and are sensitive to mesh quality, particularly in three dimensional (3D) or transient simulations [28].

Similarly, the enthalpy porosity method is extensively employed for simulating phase change, wherein the mushy zone, representing the partially melted region, is modeled as a porous medium. The phase change process is implicitly modeled by adding latent heat into the energy equation via an enthalpy term, and the velocity in the solid region is suppressed using a porosity function [29]. The enthalpy porosity method provides computational efficiency and effectively models conduction and convection without needing explicit interface tracking. However, it can inaccurately simulate solid-body motion and exaggerate convection effects due to mushy zone assumptions and density gradients [30]. To address such limitations, advanced methods have been incorporated, such as the Boussinesq approximation for buoyancy-driven convection modeling and the volume of fluid (VoF) method to capture compressibility effects and dynamic interfacial behavior, which incorporates the volume fraction into the governing equations. The concept of *compressibility* pertains to the temperature-dependent changes in liquid PCM density (thermal volumetric expansion) and does not refer to the density change caused by pressure.

The Boussinesq approximation considers density to be constant in all terms of the momentum equation, except for the gravitational source term, where density varies linearly with temperature. Such an assumption simplifies numerical analysis while still capturing natural convection within the liquid PCM. In contrast, when simulating configurations involving free surfaces, volume expansion (compressibility) or interfacial motion between immiscible fluids, the VoF method becomes critical. In the context of PCM melting, the VoF method is also capable of realizing the close contact melting (CCM) phenomenon, where a thin liquid PCM film forms between a heated wall and the solid PCM, thereby increasing the local heat transfer rate.

1.3 Motivation and Problem Statement

PCM has attracted significant interest as a heat transfer medium due to its capacity to store and release substantial thermal energy at nearly constant temperatures during phase changes. Such thermal behavior is well-suited for applications that require stable temperature conditions, including the thermal regulation of electrical equipment and the storage of excess heat from renewable energy sources for later use.

However, because of the relatively slow thermal response of PCM, especially during the charging (melting) process, its performance in dynamic operating environments can be limited. In equipment and systems exposed to high heat loads, such as power electronics and thermal control components, insufficient melting can lead to performance degradation or even thermal failure. The slow melting rate of PCM is also concerning for heat storage because only the portion of PCM that undergoes phase change actively absorbs latent heat. Therefore, incomplete melting within the available time reduces the effective storage capacity and the system's ability to buffer thermal loads as intended. In some configurations, melting behavior is further influenced by compressibility effects and CCM. While CCM can accelerate local melting, accurately capturing it in simulations typically requires accounting for density variations and fluid compressibility, effects often neglected in common incompressible formulations, such as the Boussinesq approximation, thereby limiting the representation of such phenomena in conventional models.

Over the past decade, numerous studies have proposed design modifications to enhance PCM melting efficiency and mitigate limitations resulting from its low thermal conductivity. The most common modifications include adding fins to increase surface area, utilizing metal foams to create high-conductivity porous networks, and employing cascaded PCM layers to enable multi-stage melting, resulting in a more uniform thermal distribution. Nonetheless, such techniques frequently entail significant material and fabrication costs, as well as complex geometries, which diminish their practicality in large-scale or commercial systems.

To overcome the challenges associated with the low melting rate of PCM, the present study proposes a novel approach combining forced convection with natural convection. A mechanical mixer is employed to induce internal fluid motion during melting, thereby mitigating the limitations associated with the inherently slow natural convection currents in PCM. Stimulating forced convection by incorporating a mechanical mixer is expected to reduce melting time, promote a more uniform temperature distribution, and ultimately improve overall thermal performance. In addition to evaluating the effects of forced convection, the study further compares simulations utilizing the Boussinesq approximation with those employing a VoF-based compressible formulation to investigate how various modeling approaches capture or exclude the CCM phenomenon.

The present study employs a dual methodology that combines both experimental investigation and numerical modeling to ensure the robustness and generalizability of the proposed design. Laboratory experiments are performed to evaluate the heat transfer characteristics of the system under controlled conditions. In parallel, comprehensive numerical simulations are developed not only to replicate the experimental results but also to gain deeper insight into the underlying transport phenomena and to explore aspects of the system that cannot be directly observed during experiments. The proposed integrated approach not only verifies the accuracy of the numerical models but also facilitates the development of a reliable predictive modeling framework that aligns closely with experimental outcomes. Such a framework has the potential to serve as a design tool for optimizing similar systems that utilize PCM across a diverse range of practical applications.

In summary, the current study seeks to address the fundamental limitations imposed by the PCM, particularly its extended melting time, through a cost-effective and scalable design that utilizes mechanically induced forced convection. By aligning numerical modeling with the experimental findings, the study intends to contribute to both the theoretical understanding and practical advancement of PCM-related technologies, with the broader goal of enhancing their viability for use in electrical power systems, renewable energy infrastructure, and other thermally constrained applications. Moreover, the compressibility effect is investigated in cases where constrained and unconstrained melting occurs.

CHAPTER 2

LITERATURE REVIEW

PCMs are valued for their capacity to store and release significant amounts of latent heat at nearly constant temperatures, making them ideal for applications such as thermal buffering in electrical systems, solar thermal energy storage, and battery temperature control. Nonetheless, PCMs' low thermal conductivity and slow melting speeds limit thermal performance in environments with high heat fluxes. Over the last two decades, numerous enhancement methods have been proposed to increase the melting rate of PCM, mostly passive techniques.

Passive strategies to enhance the thermal performance of PCM-based systems include expanding the thermal exchange surface to improve conduction through the use of fins [31], incorporating nanoparticles characterized by high thermal conductivity to increase the heat transfer coefficient [32, 33], and optimizing the convective heat transfer coefficient by tailoring the shape and size of the cavity [34]. Although such methods can boost heat transfer rates, they often lead to increased material costs, added manufacturing complexity, or geometric limitations that hinder scalability in practical applications.

On the other hand, active enhancement techniques, especially forced convection, offer an alternative method to intensify heat transfer without requiring extensive structural changes. Among the options, internal mechanical mixing has demonstrated potential in accelerating melting by initiating earlier natural convection, breaking up thermal stratification, and ensuring a uniform temperature distribution. Such modifications align with the objectives of the current study, which aim to improve the thermal effectiveness of PCM by increasing its melting rate.

The current study focuses solely on the melting behavior of PCM. In solidification, the growth of a solid layer on the cooled surface imposes additional thermal resistance and reduces the temperature gradient, slowing heat transfer [35]. Stabilizing density gradients further suppress natural convection, rendering conduction the dominant mechanism [36]. Although the use of mixing or stirring during solidification can partially enhance heat transfer by promoting fluid motion in the remaining liquid region [37–41], such improvements remain inherently less thermally intensive. In contrast, melting benefits from both CCM, where the solid PCM stays in direct contact with a heated surface to create a thin liquid film for high conductive heat transfer, and strong natural convection, which provides faster and more efficient heat transfer. CCM alone can contribute up to 50% of the melting heat transfer [42], whereas natural convection is considerably stronger during melting than during solidification [43, 44]. These combined phenomena make melting a more thermally intensive process, fully aligned with the goal of achieving quick and efficient heat transfer.

2.1 PCM Melting in the Absence of Forced Convection

Before evaluating forced convection, it is important to establish the baseline melting behavior of PCMs under purely natural convection and conduction. Numerous studies have been performed to examine the behavior of PCM in different cavity shapes, including rectangular, spherical, cylindrical, and annular. According to [45], however, the rectangular cavity deserves more attention than the other geometries, as it encompasses a broader range of applications, including battery packs and electrical transformers.

Hamdan *et al.* [46] theoretically studied the melting behavior of the PCM enclosed in a rectangular cavity. Four distinct stages were observed following the heating of the specified vertical wall. The wall undergoes a period required to reach the temperature of fusion of the PCM, T_f. The next stage involves heat being transferred mainly to the melt front, the interface between solid and liquid, through conduction. Then, there is a shift from conduction-driven heat transfer to natural convection, characterized by the tilt of the melt front, the formation of a hot boundary layer near the hot wall, and a cold boundary layer close to the melt front. In the final stage, reduced convection intensity due to thermal stratification is observed. In their experiments, natural convection usually began once about 45–55% of the PCM mass had melted. Gong *et al.* [47] confirmed the delayed onset of natural convection, noting that it is a significant factor limiting the overall melting rate, a finding directly relevant to the goal of accelerating heat transfer during the early stages.

Several studies, including those by Pal *et al.* [48], as well as Shokouhmand *et al.* [49], have documented the decline of natural convection during the final melting stages. Inside heated rectangular cavities, Pal *et al.* [48] identified four distinct melting regions along the heated wall, with the final stage marked by reduced buoyancy-driven circulation as temperature gradients decreased and the liquid PCM temperature became more uniform. Similarly, Shokouhmand *et al.* [49] observed that once the melt front reached the opposite insulated wall, temperature stratification developed in the upper region, causing a significant decline in convection intensity. The late-stage weakening of natural convection, caused by diminished buoyancy forces and thermal stratification, shifts the process back toward conduction dominance and strongly justifies using internal mixing to maintain fluid motion and delay thermal stagnation until complete melting is achieved.

With the approach of choosing the optimal geometry ratios to confine PCM, Binet *et al.* [50] studied the melting behavior inside a rectangular cavity but with different aspect ratios (ARs). Two modes of vertically oriented walls, heated either uniformly or discretely with a specified constant heat flux, were discussed, with the focus here on uniformly heated walls. It was observed that exceeding an AR of 10 leads to a conduction-dominated heat transfer process to the PCM. Additionally, when the AR is below 0.1, the melting time increases significantly, rendering such configurations impractical for application. Huang *et al.* [51] experimentally studied the effect of heating a vertical wall with constant heat flux in a rectangular cavity full of PCM with different heights. The main observation was that although increasing the AR would strengthen natural convection currents, the melting time would be increased.

Similar studies by Hamad *et al.* [52] and Gobin *et al.* [53, 54] confirmed that an intermediate AR would provide the best balance between rapid convection development and sustained heat flux.

Experimental studies have improved understanding of PCM melting but face challenges like incomplete visualization of internal flow and difficulty measuring quantities such as velocity fields and heat flux. Such drawbacks in experimental studies make theoretical and computational methods crucial for fully understanding the melting process. Hamdan *et al.* [55] developed an analytical model to investigate the melting behavior of PCM in a rectangular cavity. The model effectively represented the initial melting phase dominated by conduction, but did not match observations once natural convection became significant, thereby highlighting a key limitation of analytical methods, namely their difficulty in predicting the dynamic shape of the melt front under convection. While the model aligned well with experimental melt fraction values, it failed to accurately depict the evolution of shape and the progression of the interface. Analytical techniques may thus be inadequate for applications requiring precise melt front tracking, justifying the use of numerical modeling in the present study.

Scanlon *et al.* [56] numerically investigated the effect of putting a heater inside a small rectangular cavity full of PCM. The formation of Benard-type convection rolls and multicellular flow structures penetrating the solid PCM was observed using ANSYS FLUENT, resulting in a wavy and non-uniform melt front. Results indicate the complexity of internal flow patterns and their significant influence on melt front morphology, emphasizing the need for 3D numerical models.

Another notable study on the PCM melting was conducted by Lamberg *et al.* [57], who numerically investigated the process using the enthalpy porosity and effective heat capacity methods. The enthalpy porosity method models phase change by linking enthalpy to temperature and representing the partially melted region, mushy zone, as a porous medium with decreasing permeability during phase change. The effective heat capacity method, on the other hand, accounts for latent heat by increasing the specific heat over the temperature range where phase change occurs. It was reported that as long as the temperature range of melting for PCM is smaller than $2°C$, the effective heat capacity method would be closer to the experimental work. However, in the current study, melting occurs over a wider temperature range ($> 2°C$), making the enthalpy porosity method more appropriate because of its ability to capture the gradual phase transition accurately. The effect of natural convection was also highlighted in the same study. The conclusion was that ignoring natural convection could nearly double the melting time compared to when natural convection is considered. Observations emphasize the importance of maintaining natural convection currents within the domain by avoiding disrupting barriers.

Fadl *et al.* [58] numerically examined the melting behavior of PCM inside a rectangular cavity with different heat fluxes using the enthalpy porosity method. The significance of choosing the correct mushy zone constant (C_{mush}), which governs permeability reduction in the mushy zone, was highlighted because it aligns with experimental data on melt front propagation. It was noted that a lower value of C_{mush} may lead to an overestimation of the melting rate, whereas a higher value may result in its underestimation. These observations underscore the importance of C_{mush} selection in simulations, which remains crucial in the present study to ensure the accurate representation of melting dynamics and consistency with experiments. Modeling techniques enable the visualization and analysis of complex physical phenomena within computational simulations. Among the physical phenomena, CCM stands as a principal mechanism capable of increasing the melting rate.

Moallemi *et al.* [59] pointed out the CCM phenomenon in their studies to be crucial while analyzing PCM melting behavior inside cavities. It has been observed that the inclusion of CCM, which is considered unconstrained melting, increases the melting rate by a factor of seven compared to a similar setup without CCM, which accounts for the constrained melting. Furthermore, it has been observed that, due to the nearly uniform thickness of the melt layer, particularly at the bottom of the cavity housing, heat transfer is mainly controlled by conduction.

In a complementary study, Hu *et al.* [60] considered a hot sphere with a constant temperature above the PCM melting point. The PCM melting behavior and melt thickness around the hot sphere were studied. It was reported that melt thickness remained nearly uniform as the process advanced. Since the current study employs a centrally located heated cavity, in which the heater remains in contact with the solid PCM during melting, a CCM-like behavior is expected to emerge in the later stages of melting, thereby enhancing conduction dominance and increasing the melting rate.

Regin *et al.* [61] considered the effect of putting a spherical capsule full of PCM inside a water bath with a constant temperature above the melting point. The melting behavior of PCM inside the cavity was investigated both numerically and experimentally. The enthalpy porosity and the effective thermal conductivity methods were used in the numerical process. As a final remark, the deviation of numerical results from experimental data is up to 21%, with most of the realized difference attributed to the omission of CCM, highlighting the importance of selecting the appropriate numerical method when simulating the CCM phenomenon.

Benchmark studies performed by Shmueli *et al.* [62] Assis *et al.* [63] that investigate the melting process of a commercially available PCM both numerically and experimentally within cylindrical and spherical PCM cavities subjected to a constant temperature above the PCM melting point. The VoF method was incorporated in ANSYS FLUENT 6.0 software to track fluid interfaces by solving for the fractional volume of each phase, offering an overview of volumetric expansion during PCM melting. Observations on melt front deformation and natural convection development have provided a baseline for validating the numerical simulations in the current study. Tan [64] experimentally considered a sphere full of PCM. The outer wall of the sphere was subjected to a constant temperature exceeding the melting temperature. It can be inferred that two zones are formed, which are the natural convection zone and the conduction-only zone. The natural convection zone at the top of the melt front exhibits two significant currents, which are primarily symmetrical in nature. Another zone, the conduction-only region, accounts for most of the melting rate, facilitating the upward movement of the warm liquid phase of the PCM due to the downward motion of the solid PCM, thereby supporting natural convection. Figure 2.1 provides a detailed depiction of the observed heat transfer mechanisms during PCM melting within a spherical cavity.

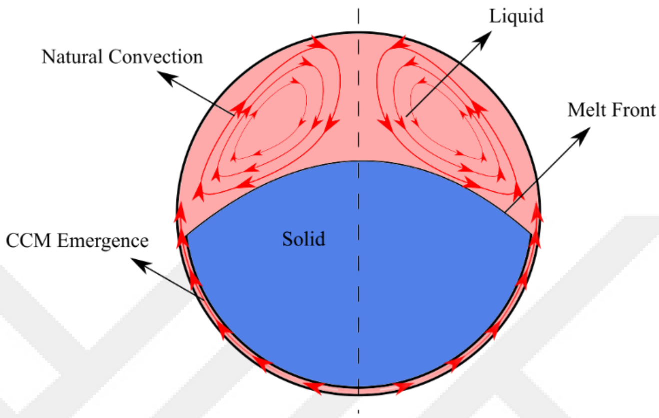

Figure 2.1 Natural convection and heat conduction in unconstrained melting (Adapted from [64])

Archibold *et al.* [65] conducted studies by melting PCM in a spherical cavity. Unlike prior related studies, the vent to the air was closed, treating air as an ideal gas in the VoF modeling method. From the results, it is realized that the pressure inside of the domain can reach up to 220 kPa, exerting a mechanical impact. Observations from the study highlight the importance of design considerations to enable the liquid PCM to be expanded or released within the cavity. Trapping liquid PCM without vents could cause high pressure and even cavity failure.

Sharifi *et al.* [66] studied the effect of vertically putting a hot rod inside a vertical cylinder full of PCM. The evolution of melt front morphology and temperature distribution was investigated as the cavity was tilted at different inclination angles. Observations indicate that using a two dimensional (2D) numerical model can only partially validate the experimental results, since 3D currents within the liquid PCM are visible during the experiments. Also, it is deducted that a larger cavity would allow a more accurate assessment of conjugate heat transfer effects, whereas a cavity that is too small may obscure or diminish the influence of such effects. For improved accuracy, related studies should incorporate 3D simulations and larger experimental domains to capture the spatial dynamics of the melting process more effectively.

During PCM melting, researchers observed some important insights, such as the need to include an expansion tube to monitor the liquid fraction during experiments, considering the density difference between PCM phases [67, 68], and understanding the minor effect of air bubbles on heat transfer and melting rate, which can be trapped inside the solid PCM during studies [69].

The formation of air bubbles during the experiment is clearly depicted in Figure 2.2, which was taken after 18.5 minutes of melting. During the current study, bubbles trapped in the solid PCM mass during pouring and solidification are observed, and it is assumed they would have a negligible effect on heat transfer.

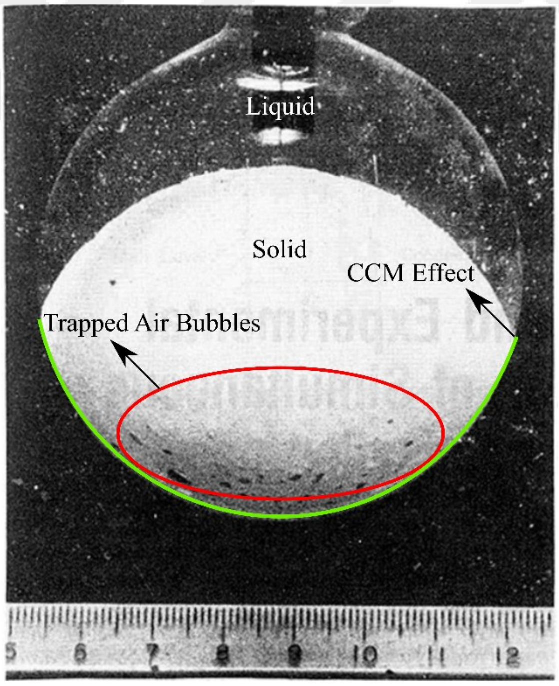

Figure 2.2 Air bubble formation inside spherical geometry (Under courtesy of [68] with written consent)

2.2 Forced Convection-Enhanced Melting of PCM

While natural convection and CCM provide important heat transfer pathways, their intensity diminishes as melting progresses, leading to a decline in heat flux. To overcome such limitations, several studies have investigated the use of mechanical rotation to induce forced convection within PCM domains. Rotational motion enhances internal fluid mixing, disrupts thermal stratification, and accelerates melt front progression by continuously renewing the temperature gradients near the heat transfer surfaces.

Chaboki *et al.* [70] and Geiger *et al.* [71] were among the first researchers to discover the profound effect of rotation on the enhancement of the thermal behavior of PCM. It was inferred that, in certain specific cases, the rotating cavity could potentially reduce the melting time to half that observed without rotation. Khosroshahi *et al.* [72] conducted 2D numerical simulations involving a double-pipe system comprising the PCM between the pipes and an outer shell rotating under two distinct scenarios, which were constant speed and step-by-step. The study demonstrated that natural convection was enhanced, resulting in a 15.5% reduction in melting time in some instances of step-by-step rotational control. Conversely, in the case of continuous speed, the formation of natural convection vortex fronts was impeded, thereby diminishing their observable effects. These contrasting results suggest that not only the presence of rotation but also its control strategy is crucial. Hassanzadeh *et al.* [73] considered a cavity filled with PCM equipped with a rotating cylinder inside, using 2D numerical modeling. Although the focus was mainly on hydrodynamics, it was observed that using a smooth cylinder instead of not using one can increase heat transfer by over 250%, highlighting the impact of forced convection on thermal behavior.

Yang *et al.* [74] considered a shell-and-tube structure and rotated it to examine its thermal behavior under new circumferences. They found that continuously turning in one direction has little effect compared to flip-and-rotate, which can reduce melting time by up to 35%. Zhang *et al.* [75] experimentally examined how mixing affects the melting behavior of PCM inside the shell-and-tube heat exchanger. It was concluded that stirring the PCM could increase the melting rate. Selimefendigil *et al.* [76] conducted a numerical analysis of a rotating adiabatic cylinder embedded within a rectangular cavity filled with PCM. A 2D model characterized by boundary conditions comprising vertically heated walls and horizontally adiabatic walls was utilized. Initially, the cylinder was immersed within the fully liquid PCM side and then rotated. It was observed that an enhancement of up to 22.5% in heat transfer rate could be achieved, with local heat transfer intensities being higher near the rotating cylinder. The schematic of the system and the related boundary conditions are presented in Figure 2.3. The localized enhancement near the rotating component aligns with the hypothesis presented in the current study, which suggests that positioning a mixer adjacent to the heat source enhances thermal transport within the PCM domain.

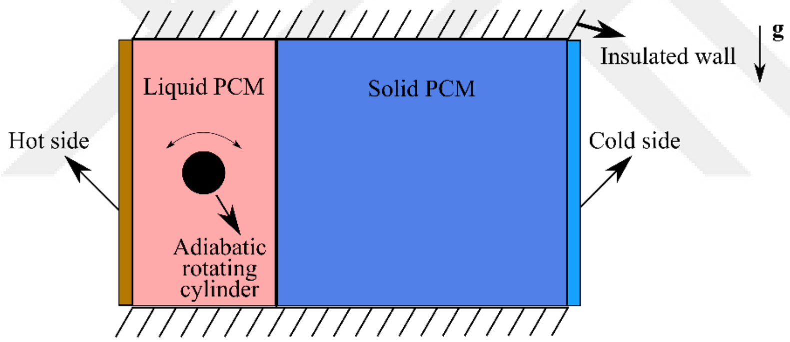

Figure 2.3 Schematic of the system and related boundary conditions (Adapted from [76])

Fathi *et al.* [77] conducted an experimental study to investigate the effect of rotating the tube inside a shell-and-tube PCM system on its melting performance. Paraffin was employed as the PCM, and the tube was rotated at three distinct speeds. The results demonstrate that although rotation causes a slight increase in the melting rate, especially at the highest rotational speed, the overall improvement is minor, with less than an 8% increase at lower speeds. It was concluded that low-speed rotation alone may not substantially improve performance, and better results might be achieved by optimizing rotation speed or using different mixer designs, highlighting the need for detailed parametric analysis, including mixer speed optimization. On the other hand, the mixer geometry design was studied thoroughly to have the optimum flow stimulation. However, they did not evaluate the energy cost of rotation, which remains an important factor to consider.

Kolsi *et al.* [78] investigated melting PCM inside a 3D double T-shaped cavity with openings for fluid to flow in and out. One of the observations was that rotation accelerated the melting process, reducing the melting time by up to 40% even at low flow speeds.

Extensive research has been conducted on passive techniques like fins, nanoparticles, and cavity geometry, as well as active methods such as cavity rotation and magnetic mixing to enhance PCM melting rates. Nonetheless, some gaps still exist. While rotational and magnetic stirring yield some thermal improvements, research on systems with internal mechanical mixers within PCM-filled cavities is still limited. The influence of mechanical stirring on convection patterns and melting efficiency needs more study and experimental verification. Additionally, although active mixing enhances heat transfer, it consumes energy, which is often overlooked. The energy required for mechanical mixers and internal heaters, and its impact on thermal efficiency, lacks detailed analysis. The present study examines the effectiveness of the mixer to balance thermal gains and energy costs. Moreover, PCM research lacks real-time thermal control systems, such as programmable units that adjust based on temperature feedback. Through the current study, a feedback-based thermal management system is introduced. Lastly, although Boussinesq and VoF models are frequently used in PCM melting simulations, few studies have validated such approaches against experimental data or conducted direct comparisons between each other, thereby limiting confidence in their predictive accuracy under practical operating conditions.

In summary, current study aims to address some research gaps, such as (i) the unstudied effect of internal mechanical mixing on PCM melting, (ii) the need to measure power consumption in active PCM thermal enhancement applications, (iii) the unexplored use of active temperature control systems for thermal optimization, and (iv) the limited knowledge on the compressibility effect and comparison of the Boussinesq and VoF methods for evaluating melting behavior under different conditions.

In light of the identified research gap, the present work examines the effects of internal mixing on PCM melting behavior. The study proceeds with an examination of the methodological framework and the main findings, with emphasis on evaluating thermal performance and energy efficiency.

CHAPTER 3

METHODOLOGY

The study employs experimental and numerical methods to examine PCM melting under different conditions. Experiments are conducted in two configurations, non rotating (NR) and rotating (R), to assess how mechanically driven fluid motion affects melting rate, temperature uniformity, and thermal efficiency. The setup, including the cavity housing, heater, and mixer, is detailed to ensure reproducibility, along with measurement techniques, data acquisition, and PCM selection to maintain consistency with numerical analysis. The numerical investigation complements the experiments by providing detailed insight into heat transfer and fluid flow phenomena that are difficult to measure directly.

To capture both constrained and unconstrained melting, two domains are modeled. The Boussinesq approximation treats the PCM as incompressible with buoyancy-driven density variations, while the VoF method explicitly incorporates the compressibility effect. In both cases, the enthalpy porosity method is applied to model phase change via a porous mushy zone. This framework enables direct comparison between models and validation against experimental data, thereby strengthening confidence in the findings for practical applications.

3.1 Experimentation

3.1.1 Experimental Setup

To provide a clear visual reference, Figure 3.1 demonstrates the fully assembled experimental setup in its final configuration. The construction process of the experimental setup is presented in Appendix A.

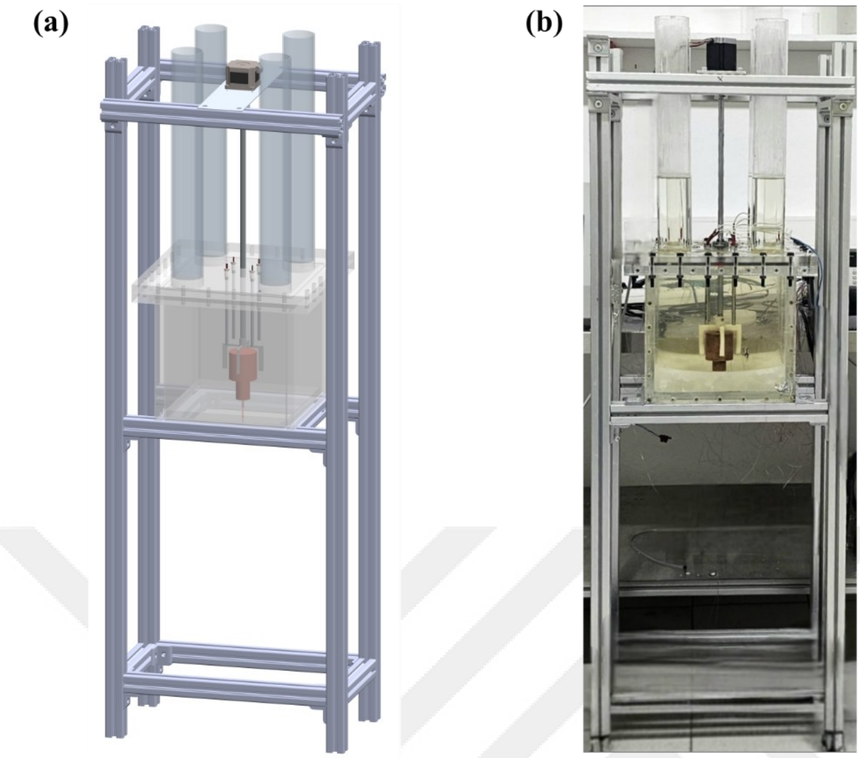

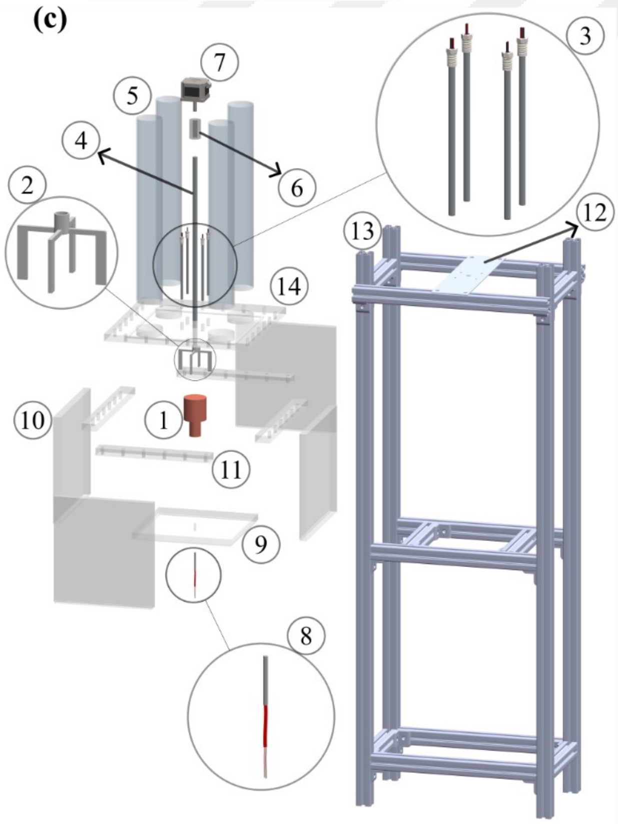

No.	Component name
1	Main heater
2	4-bladed mixer
3	Auxiliary heaters (4 pieces)
4	Rotating shaft
5	Expansion tubes (4 pieces)
6	Shaft union
7	Stepper motor
8	Cartridge heater
9	Lower wall
10	Lateral walls (4 pieces)
11	Higher wall flange
12	Stepper motor bedding
13	Setup platform
14	Higher wall

Figure 3.1 **(a)** Isometric, **(b)** actual, and **(c)** exploded view of experimental setup

The experimental setup is designed to evaluate the thermal performance of PCM under controlled conditions. The configuration includes the cavity housing, heater, mixer, measurement devices, and data acquisition systems, each serving a specific role in establishing boundary conditions, supplying heat, inducing fluid motion, and recording temperature and operational data.

3.1.1.1 Cavity Housing

The cavity housing material used to contain the PCM and conduct the experiments must be optically transparent to allow visualization, while also providing sufficient mechanical strength and thermal stability throughout the melting temperature range.

Acrylic (Plexiglass) [79], polycarbonate (Lexan) [80], and stainless steel [51, 81] are potential materials for use in the setup. The opacity of stainless steel makes it challenging to monitor during experimentation. Among polycarbonate and acrylic, acrylic is generally cheaper and more transparent. Thus, the current study utilizes acrylic with a thickness of 20 mm, offering drill tolerance for thermocouple (TC) installation.

Different geometries, even with identical PCM mass and heat transfer areas, can result in varying melting times [82–85]. The rectangular cavity shape is chosen because it is the most commonly referenced generic configuration in the literature. Furthermore, rectangular shapes cannot be simplified to an axisymmetric 2D domain, which makes them inherently suitable for 3D studies, thereby allowing for a thorough analysis of conduction and thermal stratification in the depth direction, effects at the end-walls and corners, buoyancy-driven plumes, and recirculation patterns.

The dimensions of the cavity housing used are presented in Figure 3.2.

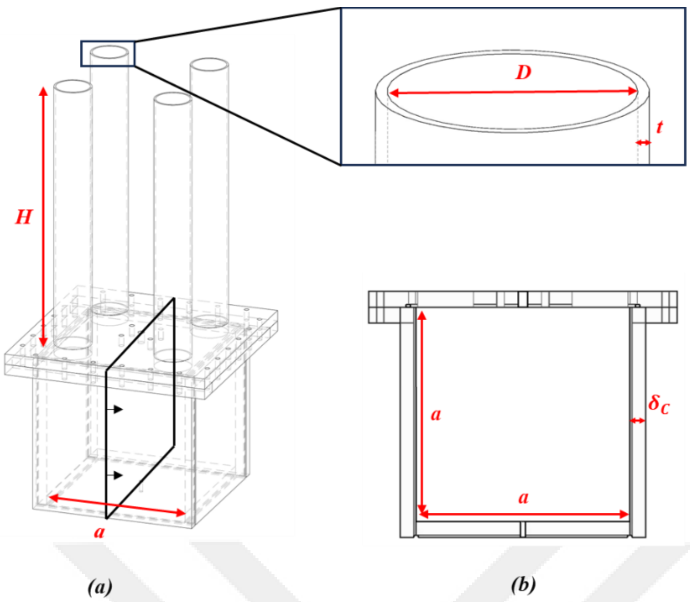

Dimension	Value (mm)
a	270
δ_C	20
D	64
H	500
t	2

Figure 3.2 **(a)** Isometric **(b)** cross-sectional views of the cavity housing

3.1.1.2 Heater

A cartridge heater is utilized to supply heat to the system. To meet the sealing requirements of the cartridge heater and ensure uniform heat dissipation, copper material is chosen due to its high thermal conductivity. A schematic of the heater is illustrated in Figure 3.3, along with the relevant dimensions in mm.

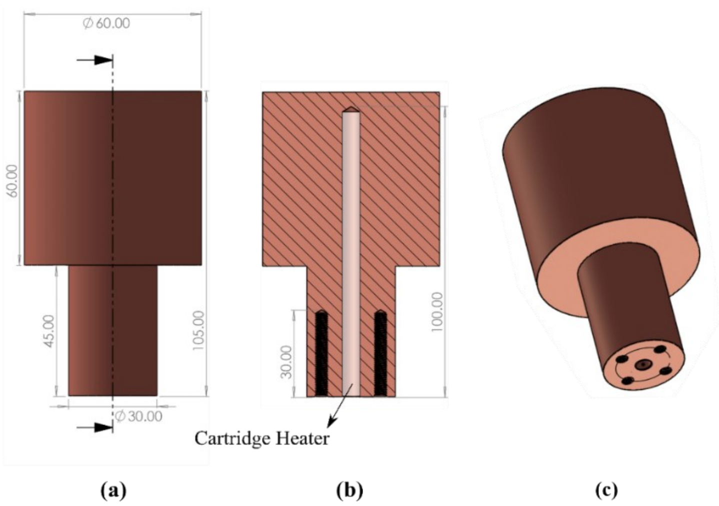

Figure 3.3 **(a)** Front, **(b)** sectional, and **(c)** isometric view of heater

The bottom section of the heater housing is made thinner to minimize heat loss through the lower wall. In contrast, the upper part of the housing is thicker, which increases the surface area in contact with the PCM and consequently reduces the temperature in the adjacent regions under the same power supply. Throughout the preliminary studies, it is observed that liquid PCM could become entrapped within the solid PCM. As the PCM melts and undergoes expansion, it exerts pressure on the cavity housing, thereby risking structural failure. To mitigate the risk, four additional heaters are installed. Additionally, with the implementation of auxiliary heaters, the liquid fraction could be identified at the onset of melting within the cavity.

3.1.1.3 Mixer

A mixer is integrated into the experimental setup to operate during the melting of the PCM. The utilization of the mixer optimizes heat transfer between the heater housing and the PCM by promoting forced convection. An improvement in the heat transfer rate is achieved by decreasing the thickness of the thermal boundary layer [86, 87]. Typically, two varieties of mixers are available, which are axial flow and radial flow mixers. Their operational principles are presented in Figure 3.4.

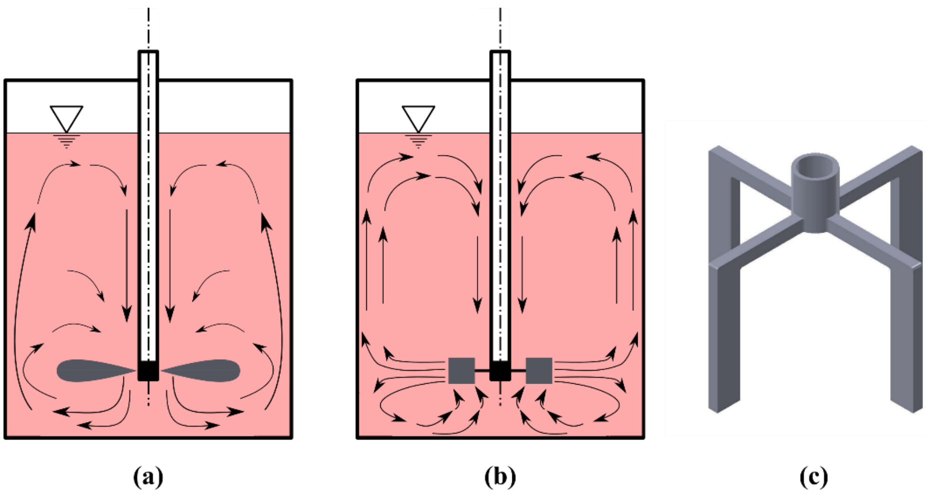

Figure 3.4 Operating principle of **(a)** axial flow mixer and **(b)** radial flow mixer [88], along with the **(c)** utilized mixer

In the lower parts of the cavity where the heater and mixer are located, conduction is more effective than convection. As a result, stirring the fluid greatly enhances forced convection. The radial flow mixer pushes the fluid outward, creating a steeper temperature gradient in that direction. Considering the experimental setup, using the radial flow mixer results in quicker charging and shorter melting times. Also, selecting the radial flow mixer ensures that the heated, melted PCM continuously 'bites' into the solid PCM, accelerating the phase change from solid to liquid.

Considering the high viscosity of PCM, which is about fifteen times that of water [89], effective mixing is essential to ensure uniform melting. To reduce power consumption, the mixer must operate efficiently, and to lower manufacturing costs, a simple design is preferred. Based on these considerations, a four-blade anchor-type mixer is utilized for the current study. The blades of the mixer are configured in a face-down orientation to ensure the mixer initiates at the earliest stage of the melting. Schematics of the chosen mixer is illustrated in Figure 3.4.

3.1.1.4 Measurement Instruments and Data Acquisition Systems

During the experiments, various instruments are employed for measurement and control, including T-type TCs, a datalogger, and an electronic control unit. The TCs used have a relative uncertainty of ±2.5% and are equipped with 0.2 mm diameter cables to minimize thermal disturbances to natural convection. A total of 45 TCs are installed. To maintain clear visibility of the cavity during the experiments, no TCs are placed on the front and back vertical walls. The arrangement of TCs is presented in Figure 3.5. The datalogger (Agilent 34972A) and the electronic control unit have respective uncertainties of ±1.2% and ±3.1%.

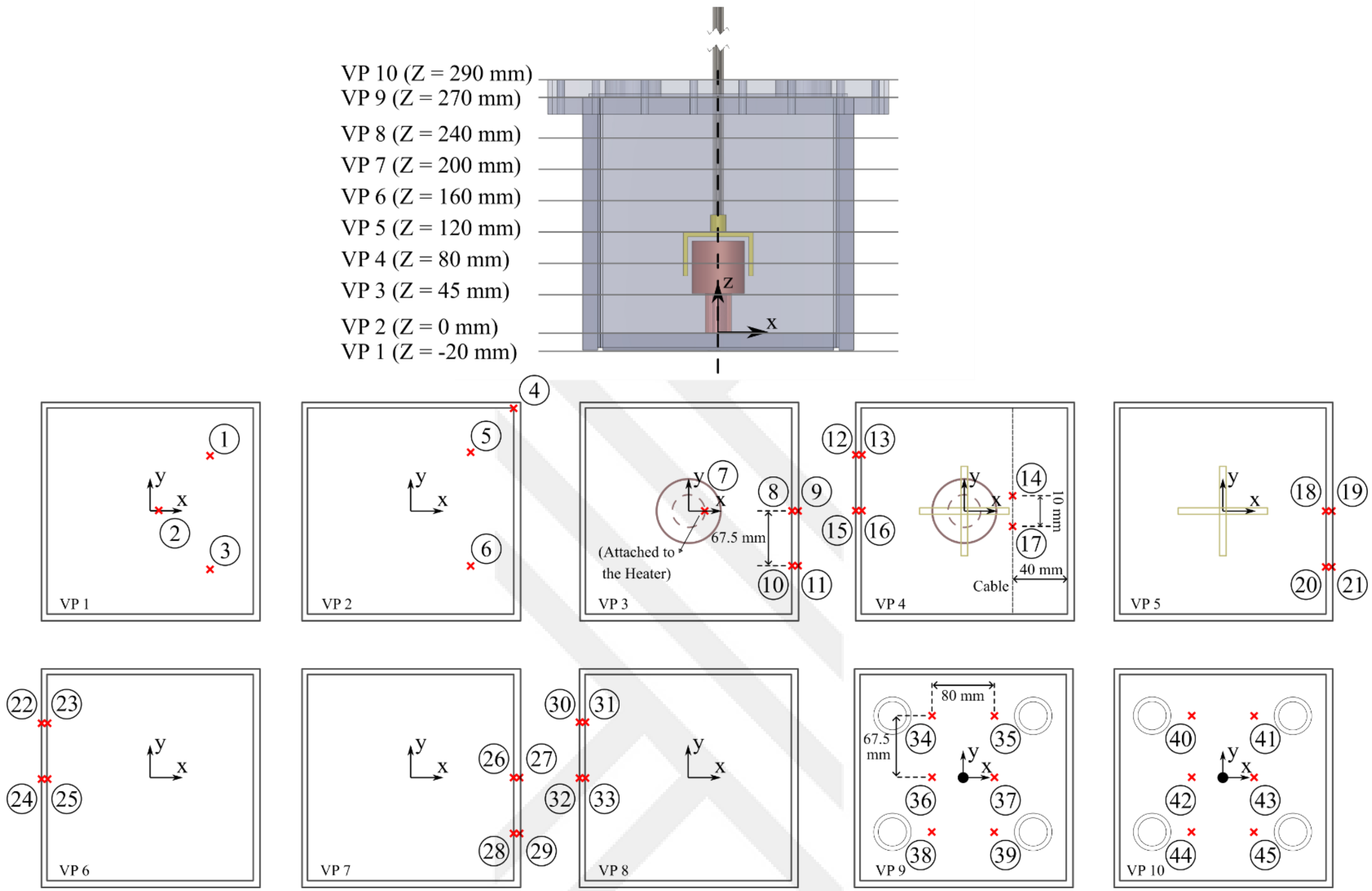

Figure 3.5 Arrangement of thermocouples

Referring to Figure 3.5, TCs are placed on ten virtual planes (VP). Furthermore, to prevent interference with currents, only a slender cable, on which two TCs are mounted for controlling the mixer, is installed within the cavity.

A series of TCs functions as temperature alarms, monitored by the electronic control unit to monitor critical stages of the experiment. One, positioned at the lowest point of the cavity and the furthest from the heater, indicates the completion of melting. Another, mounted on the heater housing, ensures thermal safety by triggering system shutdown at $65°C$ to prevent PCM thermal degradation. TCs placed near the mixer detect the approach of the melt front and activate mixing once the local temperature is adequate. Since the interior of the cavity is not observable during the initial melting phase, such measurements are vital for initiating mixing at an optimal moment, thereby enabling early involvement of forced convection and preventing mechanical damage caused by contact with solid PCM. Further details about the electronic control unit used in the present study are discussed in Appendix B.

3.1.2 PCM Selection

Selecting an appropriate PCM is crucial for effective heat dissipation and storage, as its thermophysical properties directly impact the melting rate, heat transfer performance, and long-term reliability. Literature highlights that the best PCM choice balances thermal performance needs with practical constraints, such as material compatibility and stability. Factors such as melting temperature, latent heat of melting, thermal conductivity, and repeatability of phase change affect the efficiency with which heat is released during operation. Such factors serve as the basis for assessing candidate PCMs in the current study.

PCM with melting temperatures spanning $35–45°C$ have attracted considerable interest owing to their suitability for various practical applications, especially in electronics cooling, passive building design, and solar thermal systems storage. Ghamari *et al.* [90] reviewed a wide range of building-integrated PCM solutions and emphasized that PCMs with the melting temperature range of 35–45$°C$ can decrease indoor temperature fluctuations and reduce energy consumption by up to 90% in hot climates. Within the field of solar energy, Phukaokaew *et al.* [91] demonstrated that PCMs with melting temperatures between 41$°C$ and 44$°C$ are optimal for cooling photovoltaic panels in ambient conditions of approximately 38$°C$. Similarly, Martheleur *et al.* [92] confirmed that PCMs with similar melting ranges are well-suited for managing transient thermal loads in high-powered electronics, thereby enabling the development of more compact and efficient cooling systems. These conclusions are further reinforced by experimental results from Prabhu *et al.* [93], demonstrating that nanocomposite-enhanced paraffin PCMs, melting at approximately 42$°C$, improve both the thermal stability and cooling efficiency of photovoltaic modules.

In selecting the PCM type for the current study, widely studied materials reported in the literature are considered, particularly those applied in batteries [94, 95], transformers [6], and solar or thermal energy systems [96, 97], demonstrating their broad experimental validation and technological relevance across a range of energy-related applications requiring suitable thermal properties.

Taking into account the current laboratory conditions and the required properties of PCMs, including chemical stability, non-toxicity, non-corrosiveness, as well as appropriate specific heat capacity and latent heat, RT-42 from Rubitherm is selected due to its suitability for general PCM-related applications [98]. To verify the parameters obtained from the technical catalog provided by the manufacturer, additional measurements are conducted. This approach aligns with prior findings that reported discrepancies between datasheet values and actual material behavior, as revealed through measurements by equipment such as differential scanning calorimetry (DSC) and thermogravimetric analysis (TGA) [99].

Consequently, the measured thermophysical properties of RT-42 are validated against relevant research articles to ensure accurate integration into the current thermal modeling framework.

The DSC is utilized to examine the thermal properties of the PCM during its phase change, including the quantification of latent and sensible heat. This method functions by measuring the heat flow discrepancy between a reference, an empty aluminum crucible, and the sample under a controlled temperature program. TA Instruments Q2000 DSC is used to characterize the PCM by determining its melting range, latent heat, and specific heat capacity. Prior to analysis, the sample mass is measured using a Precisa XB220A analytical balance with a readability of 0.1 mg.

The PCM is hermetically sealed in aluminum crucibles through a punching mechanism. A temperature range of $20°C$ to $70°C$ is selected to evaluate the phase change behavior of the PCM thoroughly, in accordance with guidelines recommending analysis within $\pm 20°C$ of the melting point to capture the entire DSC curve [100–102]. Two fixed heating rates of 1 K/min and 10 K/min are chosen, where the slower rate provides accurate thermal measurements, and the faster rate enhances resolution and aids in the detection of overlapping or closely spaced thermal transitions [103, 104].

Density measurements are carried out for both the solid and liquid phases of the PCM. The density of the solid PCM is measured to be 852 kg/m^3. For the liquid phase, a TAG Hydrometer is employed to measure density at various temperatures. The PCM is heated to $70°C$ in an oven, utilizing two T-Type TCs and a human-machine interface (HMI) to monitor the temperature. The setup for liquid density measurement is illustrated in Figure 3.6.

After removal from the oven, the temperature decreases due to heat loss. Since the hydrometer conforms to American petroleum institute (API) standards, a conversion to the international system of units (SI) is required.

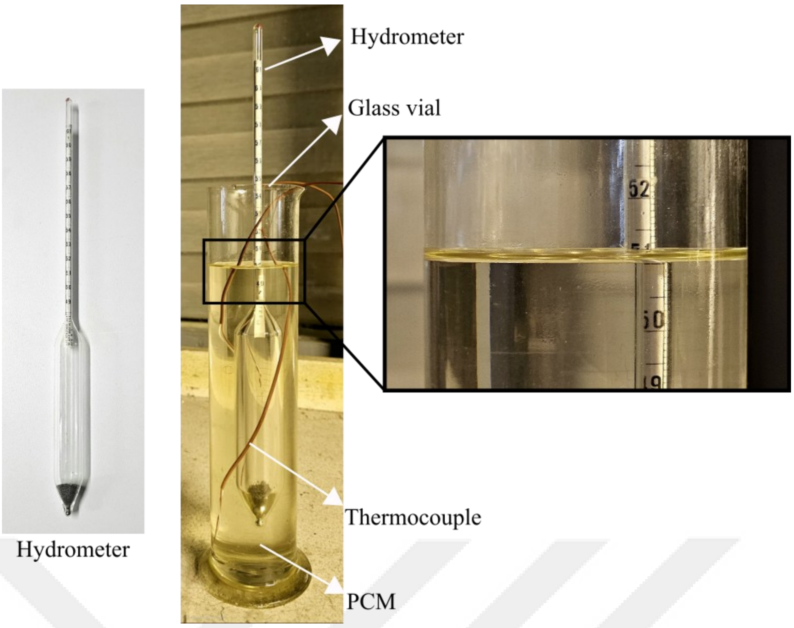

Figure 3.6 Density measurement of liquid PCM

The reading from the hydrometer is referred to as "API Gravity at 60°F". First, the corrected API gravity, which is correlated with the hydrometer reading, is derived using the Eqn. (3.1).

$$Corrected\ API\ Gravity = API\ Gravity\ at\ 60^oF + \left[CF \times \left(T_m - T_{ref}\right)\right] \qquad (3.1)$$

To adjust the actual temperature, the corrected API gravity must be calculated using the correction factor (CF) for each measurement. CF is a parameter used to account for changes in the measured temperature relative to the reference temperature. The unit of CF is $°API/°F$. Although CF is not standardized for RT-42, it is estimated as 0.0025 $°API/°F$ at 43°C and 0.0015 $°API/°F$ at 70°C. The values for CF are derived from the ASTM D1250-08 Standard [105]. It is assumed to be linearly interpolated for other CFs at any temperature between the two ends. T_m and T_{ref} are the measured and reference temperatures, respectively. Specific gravity (SG) is calculated using the Eqn. (3.2).

$$SG = \frac{141.5}{Corrected\ API\ Gravity + 131.5} \tag{3.2}$$

The density of the PCM is obtained using the Eqn. (3.3).

$$\rho = SG \times \rho_{water} \tag{3.3}$$

where ρ_{water} is taken to be 999.01 kg/m^3 at $60°F$. The variation in liquid density of PCM with temperature is illustrated in Figure 3.7.

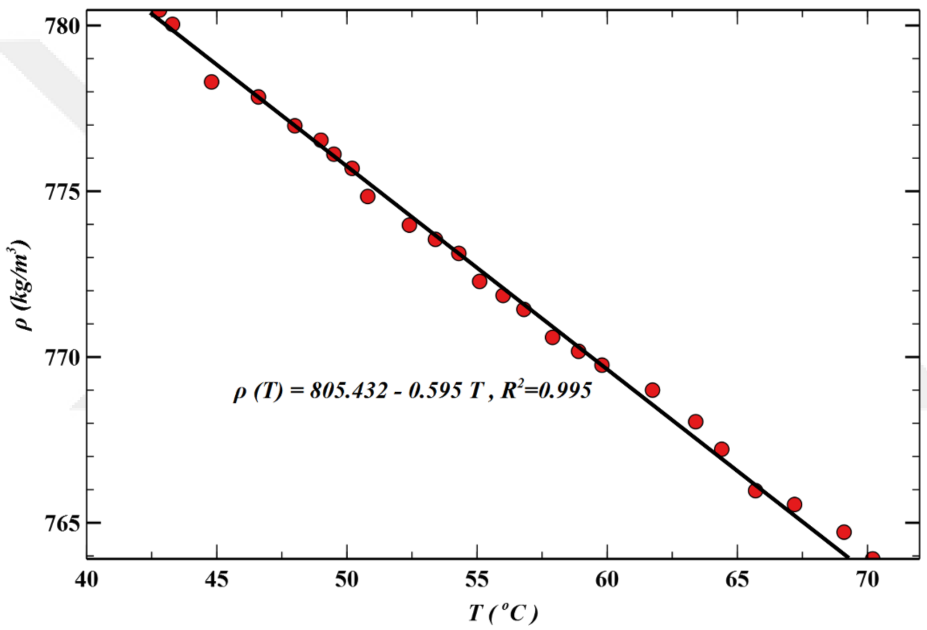

Figure 3.7 Measured liquid RT-42 density

The volumetric thermal expansion coefficient is defined as the relative change in volume per unit change in temperature. β indicates how a material expands or contracts in response to temperature variations, as outlined in the Eqn. (3.4).

$$\beta = -\frac{1}{\rho}\left(\frac{\partial \rho}{\partial T}\right)_P \tag{3.4}$$

Considering Figure 3.7, the value of 7.54 × 10^{-4} $1/K$ is obtained for β. Reported values for β is between 1 × 10^{-4} $1/K$ and 8 × 10^{-4} $1/K$ [51, 89, 106]. However, through numerical studies, it is deduced that using 1 × 10^{-4} $1/K$ would provide better accuracy. The reason behind such a modification in the β value, which controls the natural convection intensity inside the domain, is the melting progress overestimation while being modeled at higher values of β. The measured values are provided in Table 3.1.

Table 3.1 Measured and reported properties of chosen PCM

Material name	**RT-42**	
	Ref. [98]	**Measured values in present study**
T_s (°C)	38	39.4
T_l (°C)	43	43
L (kJ/kg)	165	165.4
ρ_s (kg/m^3)	880	852
ρ_l (kg/m^3)	760	Figure 3.7
μ $(kg/(m.s))$	0.02351	-
$c_{p,s}$ $(kJ/(kg.K))$	2	1.5
$c_{p,l}$ $(kJ/(kg.K))$	2	2.1
k *(both phases)* $(W/(m.K))$	0.2	-
β $(1/K)$	10^{-4} to 8 × 10^{-4}	7.5 × 10^{-4}

3.1.3 Experimental Procedure

To ensure the proper sealing of the experimental setup, first, some water leak-tightness tests are performed. In parallel, PCM mass is measured using a precision balance with an accuracy of 0.1 mg. After being molten in the industrial oven, it is carefully poured into the domain, 1 kg at a time, in batches. To minimize the formation of air bubbles inside the cavity, each PCM batch is allowed to solidify, and then the next 1 kg batch of liquid PCM is poured. This process continues until the pre-specified weight is reached.

At the first stage of the experiment, the PCM is melted when the temperature adjacent to the heater reaches the melting point of the PCM. Due to natural convection, weak currents form, causing the boundary of the melted section to be thicker in the upper part of the heating element. As time passes, more PCM melts, and the mixing process starts immediately after the mushy zone, a transitional range consisting of both solid and liquid phases, touches the outer part of the mixer.

Figure 3.8 illustrates the schematic of the setup as melting and mixing have started. The black cross represents the location of the TCs, indicating the optimal time to employ the mixer.

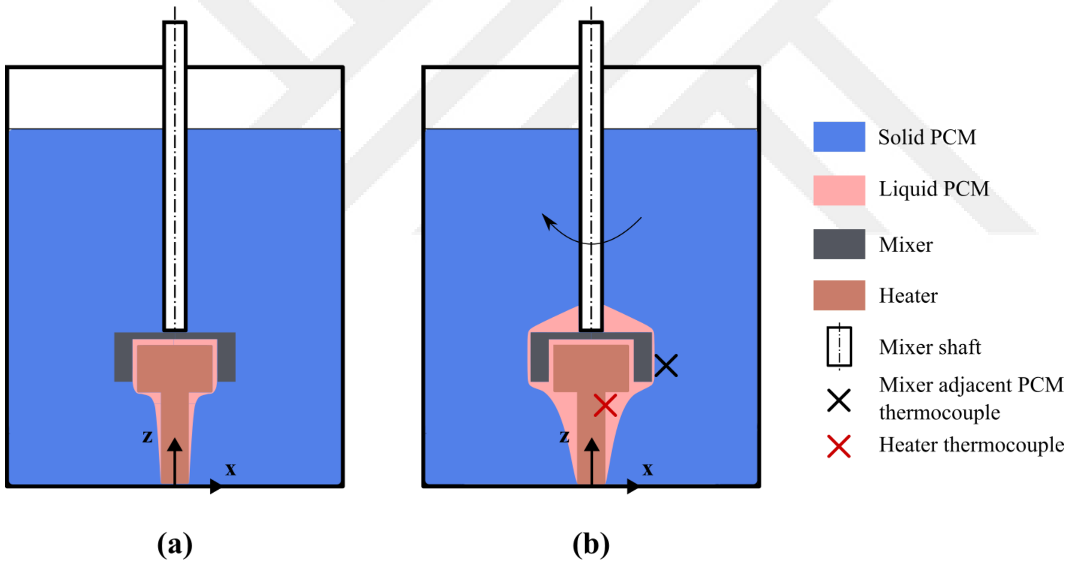

Figure 3.8 Schematic of the setup at **(a)** melting onset and **(b)** mixing initiation

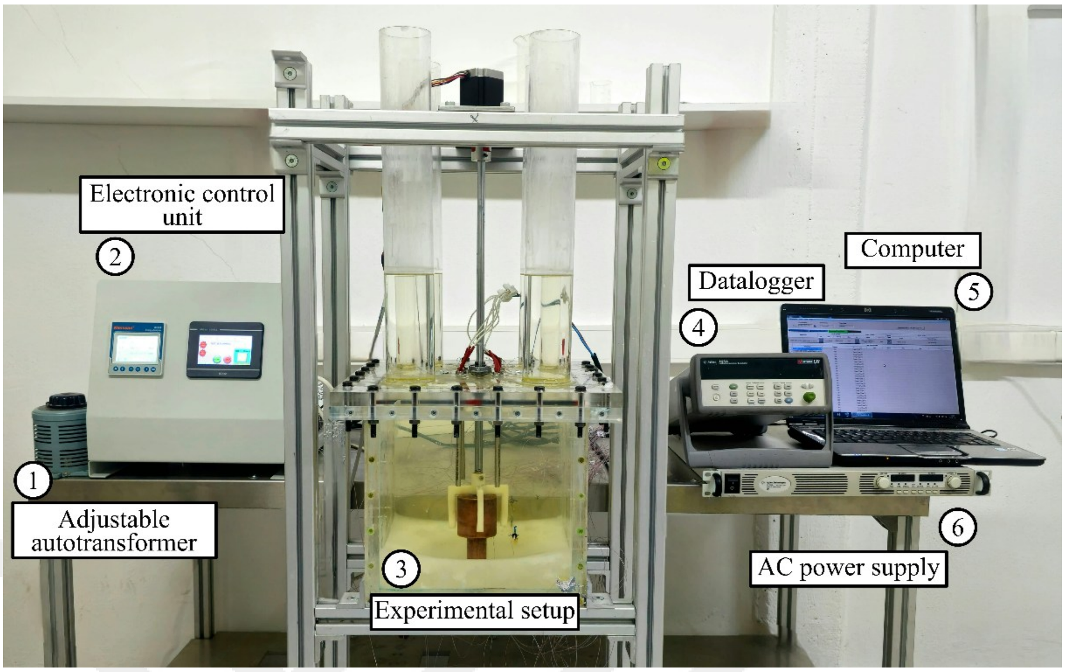

Figure 3.9 Components of experimental setup

An electronic control unit (No. 2 in Figure 3.9) is designed and built to reduce errors during experiments and improve the safety of the setup, thus preventing the PCM from undergoing chemical decomposition. The electronic control unit includes numerous components, details of which are presented in Appendix B. Readings from four TCs are fed into the electronic control unit. Based on these readings, the heater and motors are controlled to either turn on or off.

An adjustable autotransformer (No. 1 in Figure 3.9) is used to adjust the preferred voltage for the main heater and the auxiliary heaters. As mentioned earlier, 45 TCs are installed in the experimental setup (No. 3 in Figure 3.9). Some of them are redirected to the electronics control unit, while the remaining are connected to the datalogger (No. 4 in Figure 3.9). Readings are taken from both the HMI of the electronics control unit and a laptop (No.5 in Figure 3.9) connected to the datalogger. Although experiments are conducted with a constant power supply, an energy analyzer (No. 2 in Figure 3.9) is used to monitor the energy usage of the heaters. The electrical energy required for the electrical systems is supplied by an alternating current (AC) power supply unit (No. 6 in Figure 3.9).

Five experiments are conducted, with their configurations indicated in Table 3.2. Two different heat transfer rates, $\dot{Q}_h$, of 20 W and 40 W are selected to evaluate the impact of thermal input on the melting behavior of the PCM, including the initiation and progression of natural convection, as well as the time required for complete melting. Subsequently, three additional experiments are performed at the $\dot{Q}_h$ of 40 W, incorporating mechanical mixing at three different rotational speeds, N_{mix}, of 5, 25, and 100 rpm. Rotating configurations enable the evaluation of how different levels of forced convection impact heat transfer enhancement within the PCM during melting. Using a consistent heat input for the mixing trials ensured comparability across rotational conditions. It is worth noting that, due to the limitations of the geometry, all experiments inevitably involve auxiliary heaters heated at a rate of 4 W each.

Table 3.2 Experiment matrix

Experiment identification code	$\dot{Q}_h$ (W)	N_{mix} (rpm)
NR-20	20	0
NR-40	40	0
R-5	40	5
R-25	40	25
R-100	40	100

To ensure accuracy and reproducibility, all experiments are carried out in a temperature-controlled laboratory, where the ambient temperature is held steady at $21 \pm 1°C$. This procedure helps minimize external thermal fluctuations that could influence convection patterns or PCM melting behavior. Prior to each trial, the PCM is allowed to fully solidify and reach thermal equilibrium with the environment to ensure consistent initial conditions. Each experimental configuration is replicated at least twice, and the resulting data are averaged to enhance statistical reliability. Variations in TC readings across trials remained within $\pm 1°C$, indicating good repeatability. The electronic control unit and data acquisition system recorded one measurement every 5 seconds, providing sufficient temporal resolution to capture transient thermal behavior throughout the experiment duration.

3.1.4 Data Reduction

The data reduction process aims to convert raw measurements into key performance indicators that accurately describe the system's effectiveness. These include the evolution of liquid fraction, the release of heat to the environment, and the power consumption of the mixer, each calculated independently using appropriate physical models and definitions. Together, these parameters provide a comprehensive basis for evaluating the melting behavior and system efficiency.

<u>Liquid fraction</u>: The installation of expansion tubes is designed to quantify the liquid fraction. By positioning four expansion tubes around the topmost area of the cavity, the precision of the measurement is preserved.

The operational principle involves melting a greater amount of PCM within the cavity, consistent with the expanded volume, which causes additional melted PCM to be diverted towards the expansion tubes. To measure the height variations of the melted PCM inside the tubes, a ruler with 1 mm precision is employed. Additionally, the elevation of the melted PCM in each expansion tube is recorded to ensure reliable and consistent measurements. Variations in these readings could suggest blockage caused by solid PCM.

An illustration demonstrating the functioning of the expansion tubes is provided as Figure 3.10.

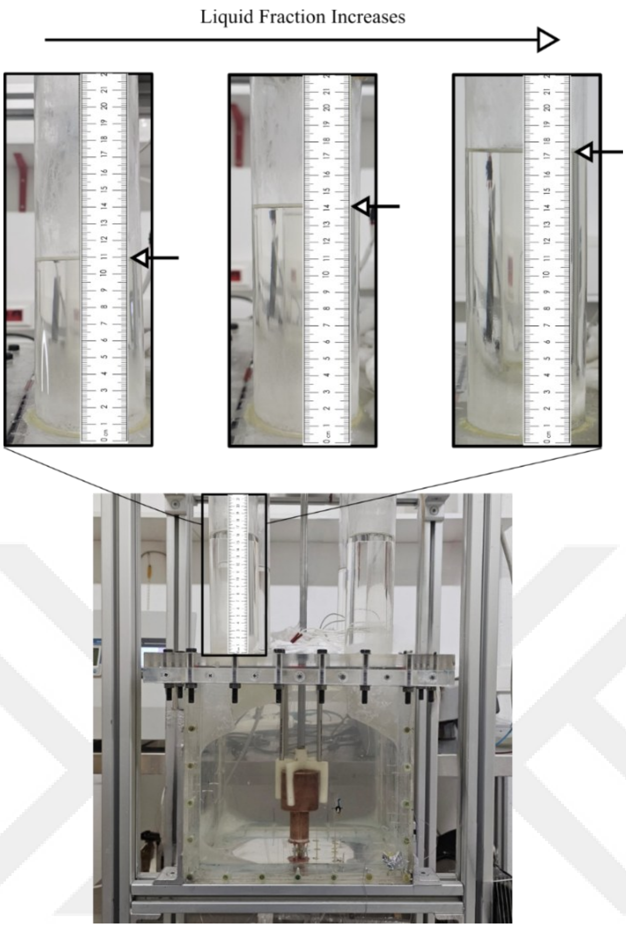

Figure 3.10 Determination of the PCM liquid fraction in experiments

Analyzing the liquid PCM progression in the expansion tubes enables the development of a method to determine the liquid fraction by measuring the height of the liquid PCM in each tube.

$$f = \frac{m_l}{m_{tot}} \tag{3.5}$$

In the Eqn. (3.5), f represents the liquid fraction of the PCM while m_{tot} and m_l are the total mass of the PCM and the part of the PCM that is melted, respectively. As a rule of thumb, the total volume of the PCM is the sum of the cavity volume, V_c, and the volume of the part of the expansion tube that is filled by PCM, V_{et}, which is related to the total mass of the PCM, m_{tot}.

$$V_c + V_{et} = \frac{m_l}{\rho_l} + \frac{m_{tot} - m_l}{\rho_s} \tag{3.6}$$

In the Eqn. (3.6), ρ_s and ρ_l are densities of the solid and liquid PCM, respectively. Eqns. (3.5) and (3.6) are harmonized to yield the Eqn. (3.7) for calculating the liquid fraction.

$$f = \frac{\rho_l \rho_s (V_c + V_{et}) - \rho_l m_{tot}}{(\rho_s - \rho_l) m_{tot}} \tag{3.7}$$

However, to prevent the cavity from failing, PCM is poured to provide some allowance on top of the cavity. The reason for doing so is to minimize the risk of cavity failure during the melting of the PCM. Additionally, the main shaft is highlighted with different heat-resistant markers to determine the liquid fraction from the onset of melting. Figure 3.11 illustrates the schematic of the marked mixer shaft. Each marked step represents 5 mm, totaling 20 mm.

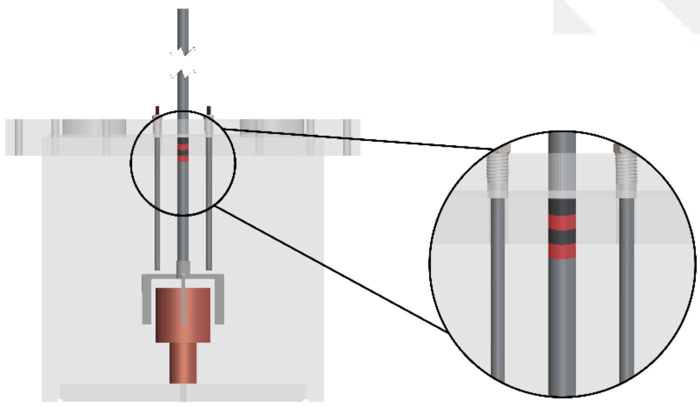

Figure 3.11 Schematic of the highlighted shaft

It is worth noting that before initiating the melting process, a 10 mm segment of the main shaft is observed, indicating a 10 mm gap beneath the top wall. However, the profile is not linear. Consequently, additional points are identified to determine the profile of the solid PCM. Two supplementary points are obtained via the expansion tube, and the volume of the empty space is calculated using SolidWorks software.

<u>Release of heat to the environment:</u> For the numerical analysis, the convective heat transfer coefficient on the outer surface of the cavity walls, h, is extracted. The mentioned quantity is embedded into the numerical model as the time-dependent profile to be accurately validated with the results extracted from the experimental study. Heat transfer through the walls due to conduction is equal to the heat transfer from the cavity wall to the environment, which is explained mathematically via Eqn. (3.8).

$$k_c \frac{T_{i,n} - T_{o,n}}{\delta_C} = h\left(T_{o,n} - T_{amb}\right) \tag{3.8}$$

k_c and δ_c are the thermal conductivity and thickness of the cavity wall, respectively. $T_{i,n}$ and $T_{o,n}$ represent the local temperatures measured at the inner and outer surfaces of the cavity wall, respectively, at the axial position n. The points are aligned in space, with $T_{i,n}$ located one the PCM-facing side and $T_{o,n}$ on the ambient-facing side of the cavity wall. Corresponding temperatures are recorded by the datalogger utilized during the experiments. h profiles are presented in Appendix C.

<u>First Law of Thermodynamics Analyses:</u> During the experiments, energy conservation was consistently monitored via the electronic control unit, and the following procedures are employed to study the energy balance.

Heat input to the system is categorized into three subsections. Q_h is the heat supplied by the main heater, which is monitored by the energy analyzer. Q_{aux} is the heat supplied by the auxiliary heaters. W_{mix} is the mixer shaft work delivered, having the assumption that no mechanical losses are in the shaft and motor that rotate the mixer, under the idealization of lossless transmission between the motor and mixer.

The heat released from the system is considered in two regions. Q_w is the heat release through the side walls, upper wall, and the lower wall that are calculated based on the TCs installed on them. Q_{et} is the heat release through the expansion tubes and are calculated based on the immersed liquid PCM and the temperature difference between the inner and outer sides of the tube. In this term, the heat loss through the higher part of the expansion tube, which has a free surface exposed to air, is also considered.

The heat retained within the system is categorized into two items. $Q_{sensible}$ is the heat stored in the system in the form of sensible heat. The specific heats incorporated in this term differ between the solid and liquid phases. Therefore, it is divided to $Q_{sensible,s}$ and $Q_{sensible,l}$, which are sensible heat stored in the solid and liquid phases, respectively, and is presented in the Eqn. (3.9).

$$Q_{sensible} = Q_{sensible,s} + Q_{sensible,l} = \int_{T_{ref}}^{T_s} m_s c_{p,s}(T) dT + \int_{T_l}^{T} m_l c_{p,l}(T) dT \quad (3.9)$$

$c_{p,s}$ and $c_{p,l}$ are the specific heat capacities of the solid and liquid PCM, respectively. Q_{latent} is the latent heat content of the system and is estimated based on Eqn. (3.10).

$$Q_{latent} = f \times m_{tot} \times L \quad (3.10)$$

The general equation satisfying the energy balance is presented in Eqn. (3.11).

$$Q_h + Q_{aux} + W_{mix} - (Q_w + Q_{et}) = Q_{sensible,s} + Q_{sensible,l} + Q_{latent} \quad (3.11)$$

Mixer usefulness (MU): During the rotating experimental studies, the mixer operates for a designated period. While in operation, the mixer consumes electrical energy, which is considered as additional work on the system that needs to be evaluated. Therefore, a multimeter is employed in parallel with the circuit to measure the current passing through.

Table 3.3 Power consumption of mixer

N_{mix} (rpm)	I_{mix} (A)	$\dot{W}_{mix}$ (W)
5	0.128	3.1
25	0.140	3.4
50	0.165	4.0
90	0.205	4.9
100	0.220	5.3

In reference to Table 3.3, an increase in rotational speed consequently results in a higher power consumption rate of the mixer. The mixer power and mixer shaft work delivered are quantified using the Eqn. (3.12a) and (3.12b), assuming the source of energy is provided via a direct current (DC) power supply at 24 V.

$$\dot{W}_{mix} = V_{mix} \times I_{mix} \tag{3.12a}$$

$$W_{mix} = \dot{W}_{mix} \times t_{mix} \tag{3.12b}$$

V_{mix}, I_{mix} and t_{mix} are the voltage and the current of the mixer, and the mixer operating time, respectively. To incorporate the effect of the melting rate, the MU is utilized as a representative metric, presented in Eqn. (3.13).

$$MU = \frac{(f_{NR} - f_R) \times m_{tot} \times L \times 10^3}{W_{mix}} \tag{3.13}$$

f_{NR} and f_R represent the liquid fraction at a given time in the non rotating and corresponding rotating configurations, while m_{tot} and L are the total mass and latent heat of PCM, respectively.

3.1.5 Uncertainty Analysis

Measurement equipment inevitably introduces various uncertainties into the conduct of experiments, which can significantly impact the reliability and validity of the results obtained. These uncertainties, which can arise from both the precision of the measurement instruments and the calculation methods employed, are critical factors that researchers must consider in their analyses.

To effectively estimate the uncertainties associated with measured and calculated quantities, scientists commonly utilize the Gauss error propagation law [107]. This mathematical formula is designed to assess how uncertainties in individual measurements can propagate through calculations involving multiple variables. The Gauss error propagation law specifies that if a quantity, denoted as R, is dependent on a set of independent variables, each with its own associated uncertainty, then the overall uncertainty in R is determined by a systematic approach that quantifies how these individual uncertainties interact and affect the final result.

$$R = \psi\ (x_1,\ x_2,\ x_3, \dots x_n) \tag{3.14}$$

Considering Eqn. (3.14), the total uncertainty of R is calculated as presented in Eqn. (3.15).

$$\Omega_R = \sqrt{\left(\frac{\partial R}{\partial x_1}\Omega_1\right)^2 + \left(\frac{\partial R}{\partial x_2}\Omega_2\right)^2 + \left(\frac{\partial R}{\partial x_3}\Omega_3\right)^2 + \cdots + \left(\frac{\partial R}{\partial x_n}\Omega_n\right)^2} \tag{3.15}$$

Ω_n is the uncertainty of the n^{th} independent variable. Table 3.4 illustrates the relative uncertainty, which is the ratio of the total uncertainty to the measured value, for both the measured and reduced parameters.

Table 3.4 Relative uncertainty analysis of measured and reduced parameters

Parameter	Relative uncertainty (%)
Liquid PCM density, ρ_l (kg/m^3)	0.79
Solid PCM density, ρ_s (kg/m^3)	0.64
Total mass, m_{tot} (kg)	0.12
Expanded volume, $V_{expanded}$ (m^3)	1.63
Cavity volume, V_c (m^3)	0.92
Mixer power, $\dot{W}_{mix}$ (W)	5.04
Mixer rotational speed, N_{mix} (rpm)	0.48
Total heat transfer rate, $\dot{Q}_{tot}$ (W)	2.51

3.2 Numerical Work

A series of numerical simulations is developed to thoroughly analyze the complex melting dynamics and effectively distinguish the distinct roles of convection and conduction. The developed models mimic the experimental setup to observe behaviors not visible in experiments, provided they are validated by experimental findings.

Additionally, comparing simulation outputs with experimental data helps evaluate whether the numerical model with similar configurations can accurately predict complex phase change behaviors without the need for experimental studies.

To validate the experimental findings, a 3D numerical domain is created, which resembles the dimensions and materials of the experimental setup. As the CCM effect has not been observed in the experimental data, the Boussinesq approximation is considered to be an adequate approach, and there would be no need to employ the VoF method to model melting dynamics [108, 109].

The Boussinesq approximation simplifies buoyancy-driven convection by assuming constant density except in the gravity term, which efficiently captures natural convection but neglects volumetric expansion during melting. To address limitations arising from not considering volumetric expansion, the VoF method monitors the evolving liquid–solid interface and captures displacement effects, rendering it more suitable for the CCM phenomenon, where a solid PCM block melts against a heated surface under the effect of gravity and forms a dynamic melt film. Nevertheless, VoF is computationally demanding owing to the requirement for high-resolution interface reconstruction and the simultaneous solution of multiple coupled phases, both of which substantially elevate the demands on grid and solver resources [110, 111]. Both methodologies are integrated within the enthalpy porosity framework, which treats the mushy zone as a porous medium, facilitating seamless modeling of conduction, convection, and phase transition phenomena. However, the reliability of the enthalpy porosity method mostly relies on accurately determining the C_{mush}, since incorrect values could lead to substantial errors, especially in estimating the time needed for the PCM to melt. Therefore, C_{mush} studies have also been conducted during the current study.

Given that CCM behavior is not observed in the validated 3D simulations, a 2D numerical domain is used to explore potential compressibility effects under conditions in which the CCM phenomenon can be observed. The transformation from 3D to 2D computational domain is primarily driven by computational efficiency, as 3D VoF simulations require a much finer mesh discretization and more solver resources to capture melt interfaces and coupled phase boundaries accurately. Previous studies reveals that 2D models can adequately replicate key thermal behaviors in PCM systems when geometries and boundary conditions are symmetric [112, 113]. Since the 3D model has already been validated, applying the same boundary conditions, C_{mush}, and material properties within a 2D framework allow for an efficient and reliable examination of melt front dynamics. Additionally, to verify the robustness of the VoF-based simulations used, two benchmark cases from existing literature are successfully reproduced.

Two 2D numerical models examined boundary effects on melting and CCM. The first, enclosed in a plexiglass container, emulated experimental conditions and did not incorporate CCM effects, serving as a baseline for comparing Boussinesq and

VoF methods without melt film dynamics. The second, housed in stainless steel and maintained at $45°C$, allowed the formation of melt films under gravity, representing practical scenarios. These models support method benchmarking and the study of material impacts on the initiation of CCM.

3.2.1 Computational Domain

As mentioned earlier, the 3D numerical domain is created to attain a holistic view of the melt front in the third dimension, facilitating more accurate validation against the experimental results obtained. To optimize computational resources while maintaining the accuracy of the findings, the numerical domain has been reduced to 1/8 of its original size. Symmetric planes at both ends are considered, allowing for a more efficient analysis without compromising the ability to represent behaviors realistically. Figure 3.12 illustrates the numerical domain and its reduced version.

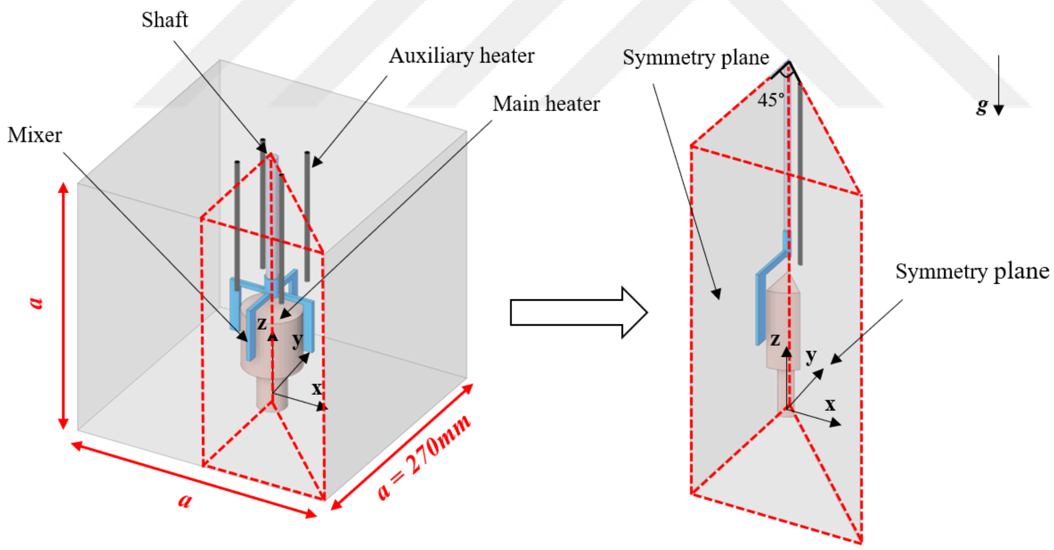

Figure 3.12 Computational domain for 3D studies

For the 2D model, two computational domains are created. To incorporate the effects of compressibility within the VoF method, a region of air above the PCM is included, as illustrated in Figure 3.13.

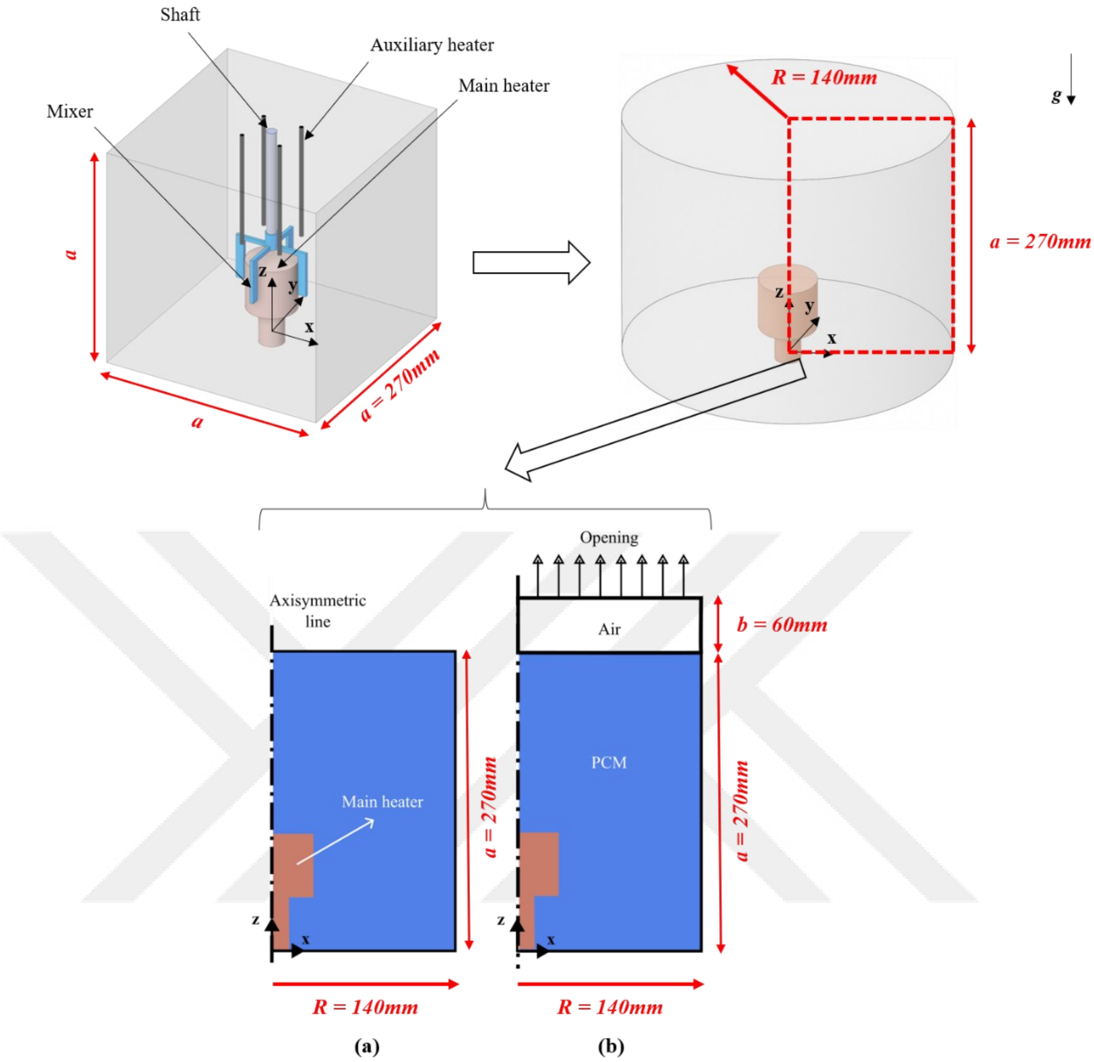

Figure 3.13 Computational domain for 2D studies **(a)** Boussinesq approximation, **(b)** VoF method

With the implementation of the axisymmetric line, the cavity assumes a circular shape. Consequently, to compensate for the volume reduction caused by the geometric change, the radius of the cavity is adjusted accordingly. Additionally, incorporating auxiliary heaters in the specified configuration would result in a shell structure rather than four separate tubes, thereby altering the realistic melting behavior observed in the experiments. Therefore, the auxiliary heater is omitted, and the voided volume is deducted to modify the radius of the cavity. The heating rates of the auxiliary heaters are incorporated in the main heater to maintain the overall melting time.

3.2.2 Governing Equations, Initial and Boundary Conditions

The analyses conducted rely on several underlying assumptions that form the foundation of the entire analysis process. Assumptions listed below are crucial for ensuring that the conclusions drawn from the analyses are valid and applicable. In the Boussinesq approximation, the liquid PCM is modeled as a transient, incompressible, laminar, and Newtonian fluid. In contrast, the VoF method treats the liquid PCM as a compressible fluid, making its volumetric expansion significant and thus included in the analysis.

- Viscous dissipation is neglected [114].

First, the enthalpy porosity method, incorporating the Boussinesq approximation, is discussed. Based on the mentioned assumptions, the governing equations are described in Eqns. (3.16), (3.17), and (3.18).

Continuity equation:

$$\nabla . \boldsymbol{U} = 0 \tag{3.16}$$

Momentum equation:

$$\rho \frac{\partial \boldsymbol{U}}{\partial t} + \rho(\boldsymbol{U}.\nabla)\boldsymbol{U} = -\nabla P + \mu \nabla^2 \boldsymbol{U} + \rho \boldsymbol{g} \beta (T - T_{ref}) + S_{\boldsymbol{U}} \tag{3.17}$$

Energy equation:

$$\rho \frac{\partial (i)}{\partial t} + \rho \nabla . (\boldsymbol{U} i) = \nabla . (k \nabla T) \tag{3.18}$$

$\boldsymbol{U}$ is the velocity vector, T is temperature, P is the pressure, and all of them are time-averaged. μ, ρ, $\boldsymbol{g}$, and k represent the dynamic viscosity, density, gravitational acceleration vector, and thermal conductivity of the fluid, respectively. The term $\rho \boldsymbol{g} \beta(\mathrm{T} - T_{ref})$ is the Boussinesq approximation in which T_{ref} is the mean value of the solidus (T_S) and liquidus (T_l) temperatures of the PCM and β is the volumetric thermal expansion coefficient.

$S_{\boldsymbol{U}}$ is the source term for the momentum equation. When the cell is in the solid phase, the velocity should approach zero in the presence of a pressure gradient. In other words, $S_{\boldsymbol{U}}$ should dominate the remaining terms in the momentum equation. If the cell is fully liquid, $S_{\boldsymbol{U}}$ should be zero to avoid eliminating the convection and diffusion terms in the Eqn. (3.17). Brent mimicked the Carman-Kozeny equation [115] for flow through a porous medium to come up with a term named as a source term, $S_{\boldsymbol{U}}$.

$$S_{\boldsymbol{U}} = C_{mush} \frac{(1-f)^2}{f^3 + \varepsilon} \boldsymbol{U} \tag{3.19}$$

In Eqn. (3.19), C_{mush} is the mushy zone constant and is defined considering both the literature and the experimental findings, such as [116]. ε is a small constant (0.001) to prevent division by zero. Values of liquid fraction are derived from the linear relationship between the solidus and liquidus temperatures of the PCM [117], which is given in Eqn. (3.20).

$$f = \frac{T - T_S}{T_l - T_S} \quad , \qquad T_S < T < T_l \tag{3.20}$$

T_S and T_l are the temperatures in which PCM is completely solid and liquid, respectively. Considering the energy equation, i denotes enthalpy and accounts for the sensible and latent heat contents, which is defined in Eqn. (3.21).

$$i = i_{sensible} + i_{latent} = \int_{T_1}^{T_2} c_p dT + fL \tag{3.21}$$

On the other hand, while analyzing using the VoF method, some equations need modification. Before delving into the revised governing equations, a new parameter must be introduced that is utilized in the VoF method. α_n is the volume of the fluid, which is obtained by dividing the volume of the n^{th} phase by the volume of the whole cell. In the current study, two fluids are involved. Respectively, air is represented with $n = 1$ and PCM is presented with $n = 2$. For instance, if the cell does not contain any air, then $\alpha_1 = 0$, and if the cell is completely filled with air, then $\alpha_1 = 1$. For interface cells, the value of α_1 lies between 0 and 1. A similar approach is applied to the PCM phase. Considering the same assumptions, the governing equations require some modifications, which are expressed in Eqns. (3.22), (3.23), and (3.24).

Continuity equation:

$$\frac{\partial(\alpha_n \rho_n)}{\partial t} + \nabla.(\alpha_n \rho_n \boldsymbol{U}_n) = 0 \tag{3.22}$$

Momentum equation:

$$\frac{\partial(\alpha_n \rho_n \boldsymbol{U}_n)}{\partial t} + (\boldsymbol{U}_n.\nabla).(\alpha_n \rho_n \boldsymbol{U}_n) = -\alpha_n \nabla P_n + \alpha_n \mu_n \nabla^2 \boldsymbol{U}_n + \alpha_n \rho_n \boldsymbol{g} + S_{\boldsymbol{U}} \tag{3.23}$$

Energy equation:

$$\frac{\partial(\alpha_n \rho_n i)}{\partial t} + \nabla.(\alpha_n \rho_n \boldsymbol{U}_n i) = \alpha_n k_n \nabla^2 T_n \tag{3.24}$$

α_n, $\boldsymbol{U}_n$, μ_n, P_n, ρ_n, $\boldsymbol{g}$, k_n, and T_n represent the volume fraction, velocity vector, dynamic viscosity, pressure, density, gravitational acceleration vector, thermal conductivity, and temperature of the n^{th} fluid, respectively.

PCM and air are initially at rest. The initial temperature is set to $21°C$, matching the experimental conditions established by the temperature controller fans in the experiment room. At the initial temperature, the PCM is completely solid. The heat transfer rate of main heater is set to 40 W in one case (NR-40) and 20 W (NR-20) in another. However, in both cases, the heat transfer rate of the auxiliary heaters is maintained at 4 W each.

The governing equations, along with the defined initial and boundary conditions, are discretized through the finite volume method (FVM). A second-order upwind discretization scheme is used for the momentum and energy equations, whereas the pressure field is discretized with the PREssure STaggering Option (PRESTO!) method. The coupling of pressure and velocity is resolved by the Semi-Implicit Method for Pressure-Linked Equations (SIMPLE) algorithm, and time advancement is performed using a first-order implicit time-stepping scheme.

To ensure convergence, the residuals for all variables, except energy, must be lower than 10^{-4}, while a stricter limit of 10^{-6} is required for the energy equation. Generally, convergence is achieved within 10 iterations per time interval. The geometry modeling, meshing, and numerical solutions are conducted using ANSYS SpaceClaim, ANSYS Meshing, and ANSYS FLUENT 2022 R2, respectively.

3.2.3 Grid and Time Step Independence Analyses

Analyses on the grid size and time step sizes aim to ensure precise and reliable results by examining how variations in grid size and time step influence the computational outcomes within the more complex 3D framework.

Sensitivity analyses are conducted in the 3D model for three different quantities of mesh elements and three distinct time step sizes, and their results are reported in Figure 3.14.

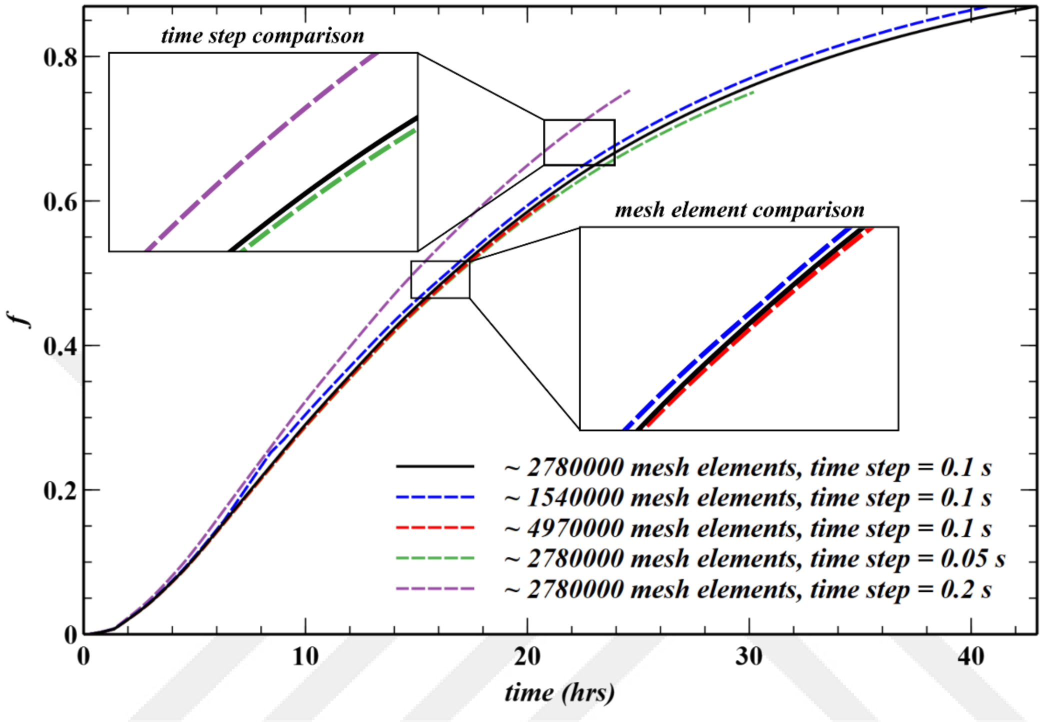

Figure 3.14 3D Mesh element and time step independence study

There is a notable effect on the simulation results when varying the number of mesh elements. When transitioning from a coarse arrangement, which consists of approximately 1540000 elements, to a fine arrangement that contains around 4970000 elements, the results exhibit consistency. Specifically, there is no significant change in the observed outcomes, which leads to the conclusion that all three mesh arrangements are considered to be in a converged state. However, it is worth noting that within the coarse mesh arrangement, a subtle fluctuation exists that diverges from the prevailing trend of the melting process. While not substantial enough to alter the overall conclusions, such slight discrepancies indicate that even with variations in mesh density, certain distinctions in the melting dynamics can be detected, thereby emphasizing the importance of mesh refinement in capturing detailed behaviors in complex simulations.

Considering the time step size employed in the analysis, it becomes evident that there is a significant discrepancy in the results encountered when transitioning from a time step of 0.2 seconds to 0.1 seconds. Nevertheless, the error is less than 1% when the time step size is further reduced from 0.1 seconds to 0.05 seconds.

Although it is known that utilizing a fine mesh arrangement in conjunction with the smallest possible time step size yields the highest level of accuracy in the computed outcomes, it is important to note that opting for a moderately fine mesh arrangement, encompassing approximately 2780000 elements, paired with a time step size of 0.1 seconds, strikes an adequate balance.

The chosen meshing arrangement for the 3D computational domain is depicted in Figure 3.15.

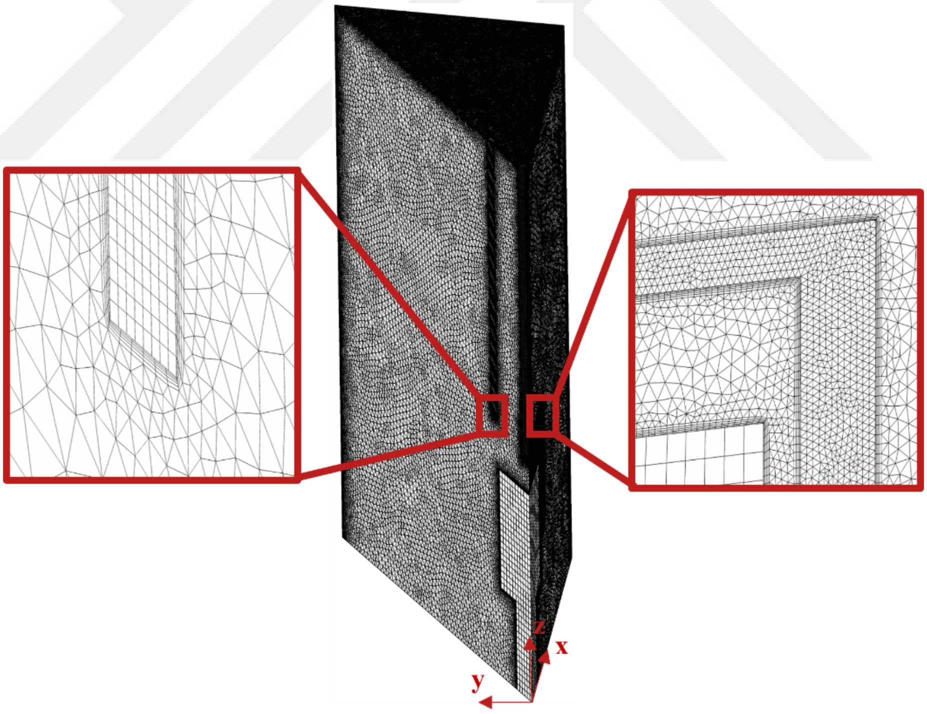

Figure 3.15 Chosen mesh for the 3D computational domain

For the 2D numerical study, an axisymmetric line is used to simplify the analysis without sacrificing accuracy. Numerical precision is verified with a mesh of 89632 cells and a time step of 0.01 s. Increasing mesh density and temporal resolution caused changes of less than 0.05% for mesh refinement and under 0.02% for time step adjustments compared to higher-resolution simulations. In the 2D simulations, the time step is set lower than in 3D primarily because the finer spatial resolution in 2D reduces cell size, which tightenes the stability and accuracy limits set by the Courant–Friedrichs–Lewy (CFL) criteria. A finer mesh is feasible in 2D due to its significantly lower computational cost compared to 3D, enabling smaller cell sizes to better capture the melting front and gradients. A smaller time step allows for more precise tracking of interface movement, reducing temporal discretization errors. Additionally, the simpler flow patterns and restricted melting front in 2D result in smoother gradients and less complex convection than in 3D. Consequently, as illustrated in Figure 3.16, mesh and time step independence analyses for the 2D case exhibit lower percentage differences between successive refinements, indicating smaller numerical errors than those found in the 3D analyses.

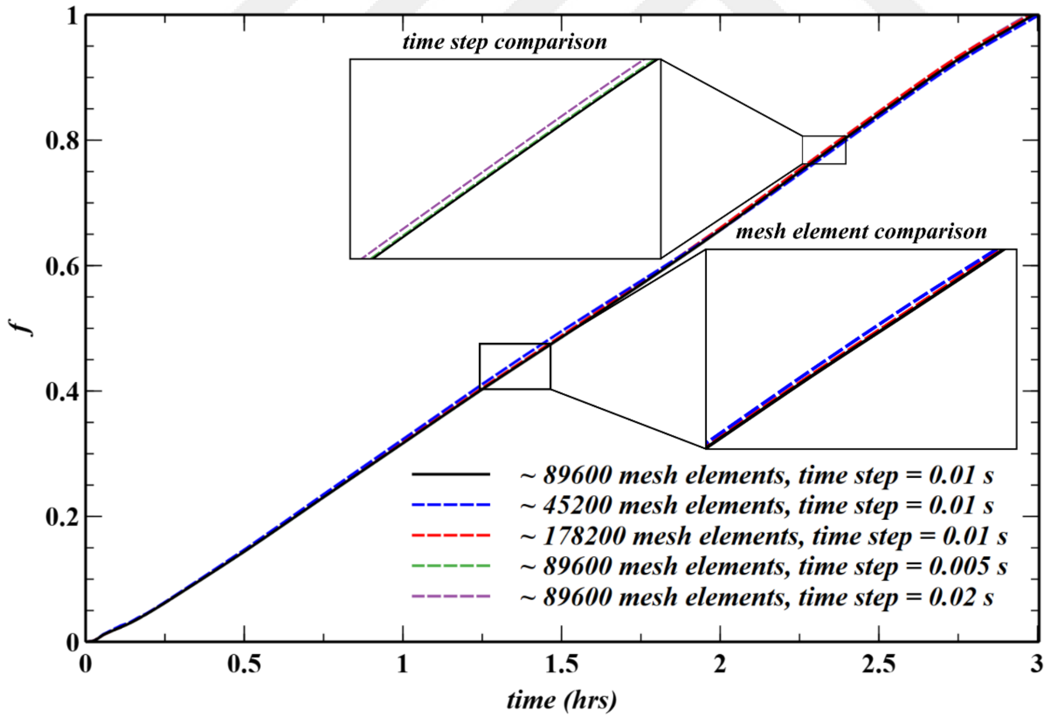

Figure 3.16 2D Mesh element and time step independence study

A total of 89632 and 74393 elements are employed for the discretization of domains for the VoF and Boussinesq methods, respectively. Simulations operate with a time step of 0.01 seconds for 2D cases. The selected mesh for the numerical analysis, utilizing the Boussinesq method, is depicted in Figure 3.17.

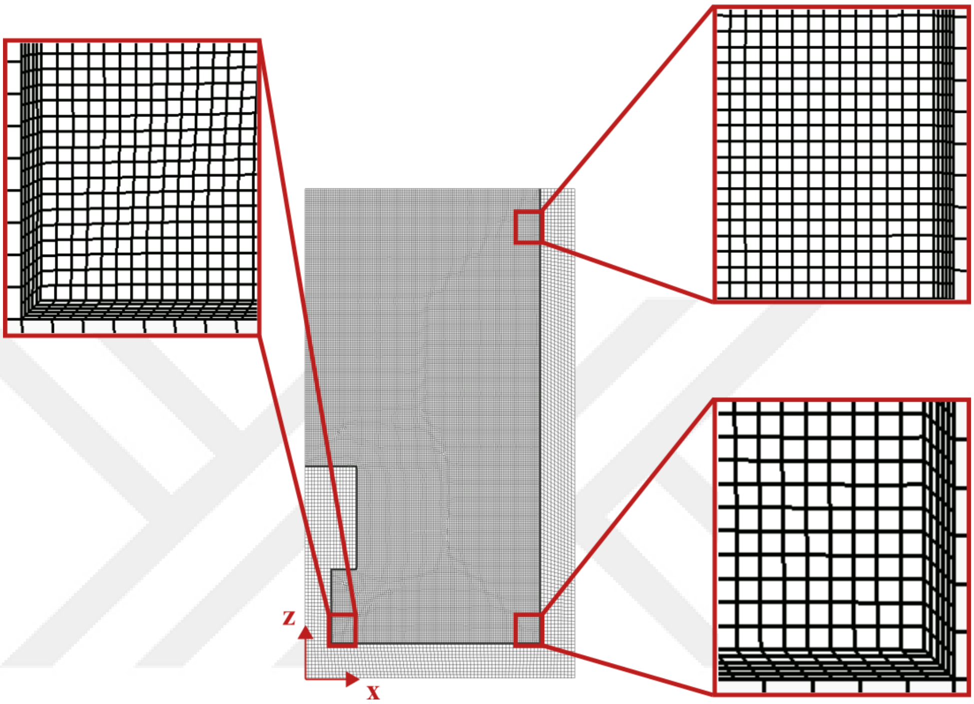

Figure 3.17 Chosen mesh for the 2D computational domain

The mesh quality is assessed using the skewness metric, which measures the deviation of mesh elements from their ideal geometry. The maximum skewness recorded is approximately 0.5, and the average skewness is 0.02, with a standard deviation of about 0.08. These values indicate that most elements are of excellent quality, with only a minor fraction exhibiting moderate skewness, remaining well within the acceptable limits for precise and stable simulations. The presence of moderate skewness in localized regions is primarily attributable to the method tackled by ANSYS Meshing in the corners when inflation layers are utilized.

CHAPTER 4

RESULTS AND DISCUSSION

The present chapter reports the experimental and numerical results of the study and provides a detailed discussion of their implications. The analysis is framed within the context of the research objectives and problem statement, with particular focus on the influence of mechanical mixing on PCM melting behavior relative to purely natural convection, and on the extent to which different numerical modeling approaches capture or neglect the CCM phenomenon.

4.1 Experimental Results

For clarity, the experimental results are presented in two principal configurations, non rotating and rotating cases. In the non rotating configuration, experiments are conducted at two distinct heating rates of the main heater to evaluate thermal response and melting progression under purely natural convection. In the rotating configuration, the study extends to three mixer rotational speeds to quantify the influence of mechanical agitation on various aspects, including melting performance and temperature uniformity.

4.1.1 Rotation-Excluded Analyses

Two different case studies are conducted for the non rotating configuration. Figure 4.1 specifies the liquid fraction and melting time at which the system reaches steady state conditions for both studies. Error bars indicate the measurement uncertainty caused by bias in the measurement devices.

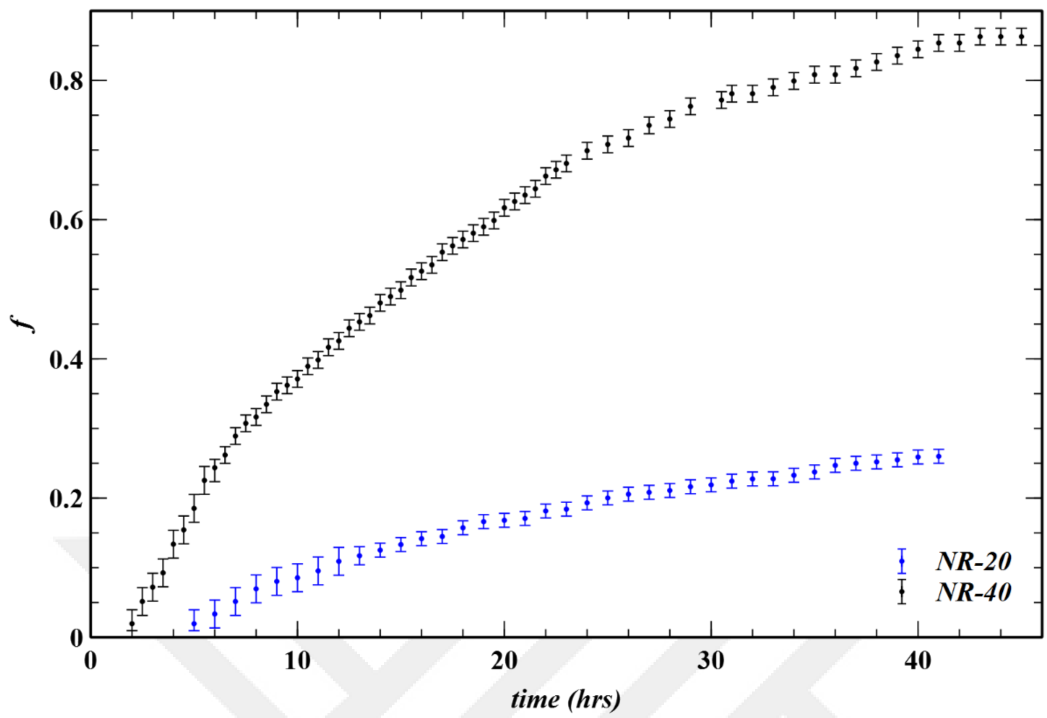

Figure 4.1 Liquid fraction of non rotating configurations

Both experiments reveal that when the mixer is not rotating, it reaches a steady state condition where the heat provided into the system equals the heat loss to the environment adjacent to the system. For the NR-40 case, the system reaches the steady state condition when 86% of the solid has been liquefied.

In contrast, the steady state condition is attained when 28% of the solid PCM is molten in the NR-20 case. In other words, in both NR-20 and NR-40 case studies, the energy balance is reached at steady state conditions prior to the complete melting of the PCM.

The schematics of the melt front for both cases are depicted in Figure 4.2.

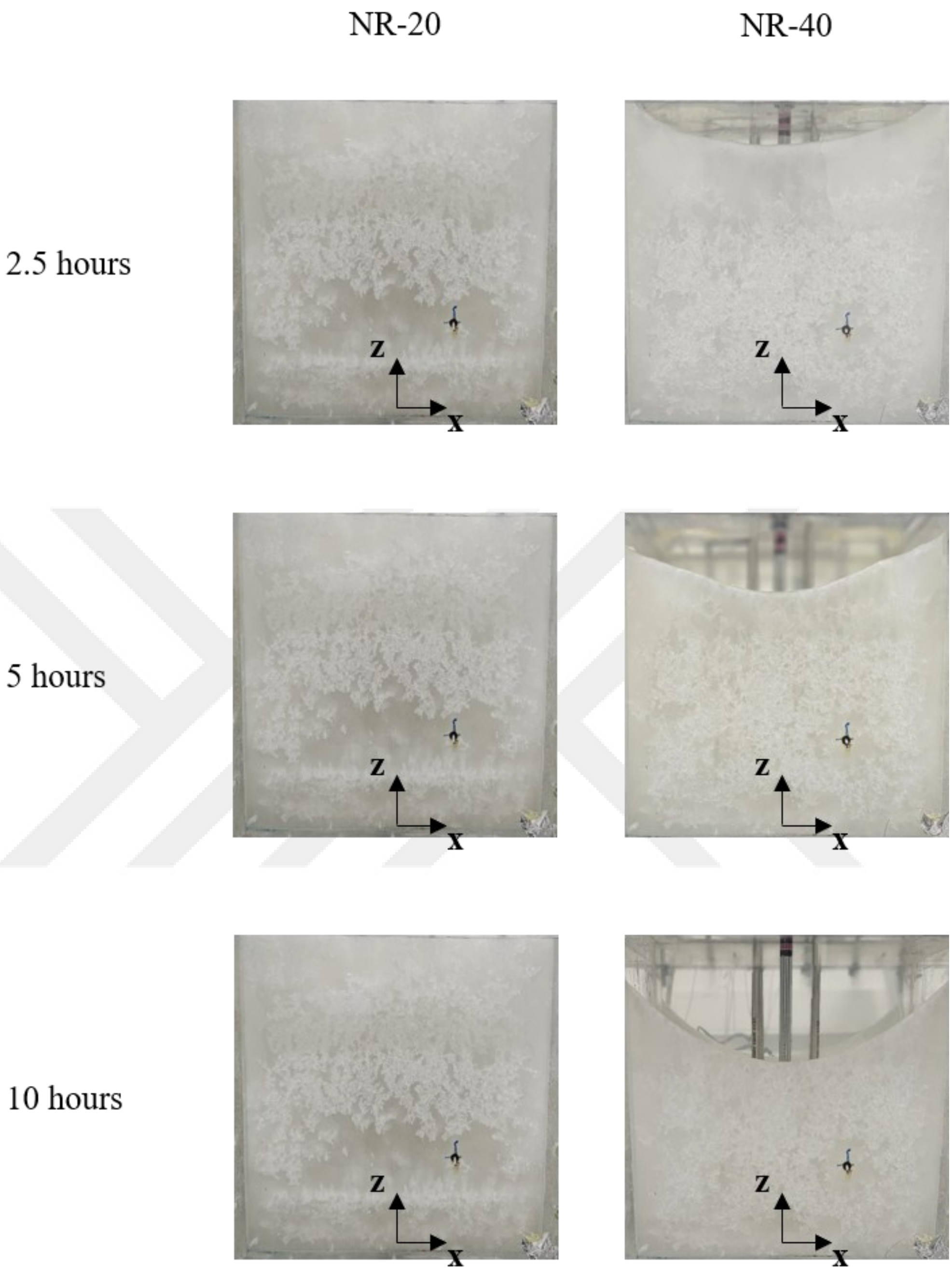

Figure 4.2 Melt front evolution for the non rotating configurations

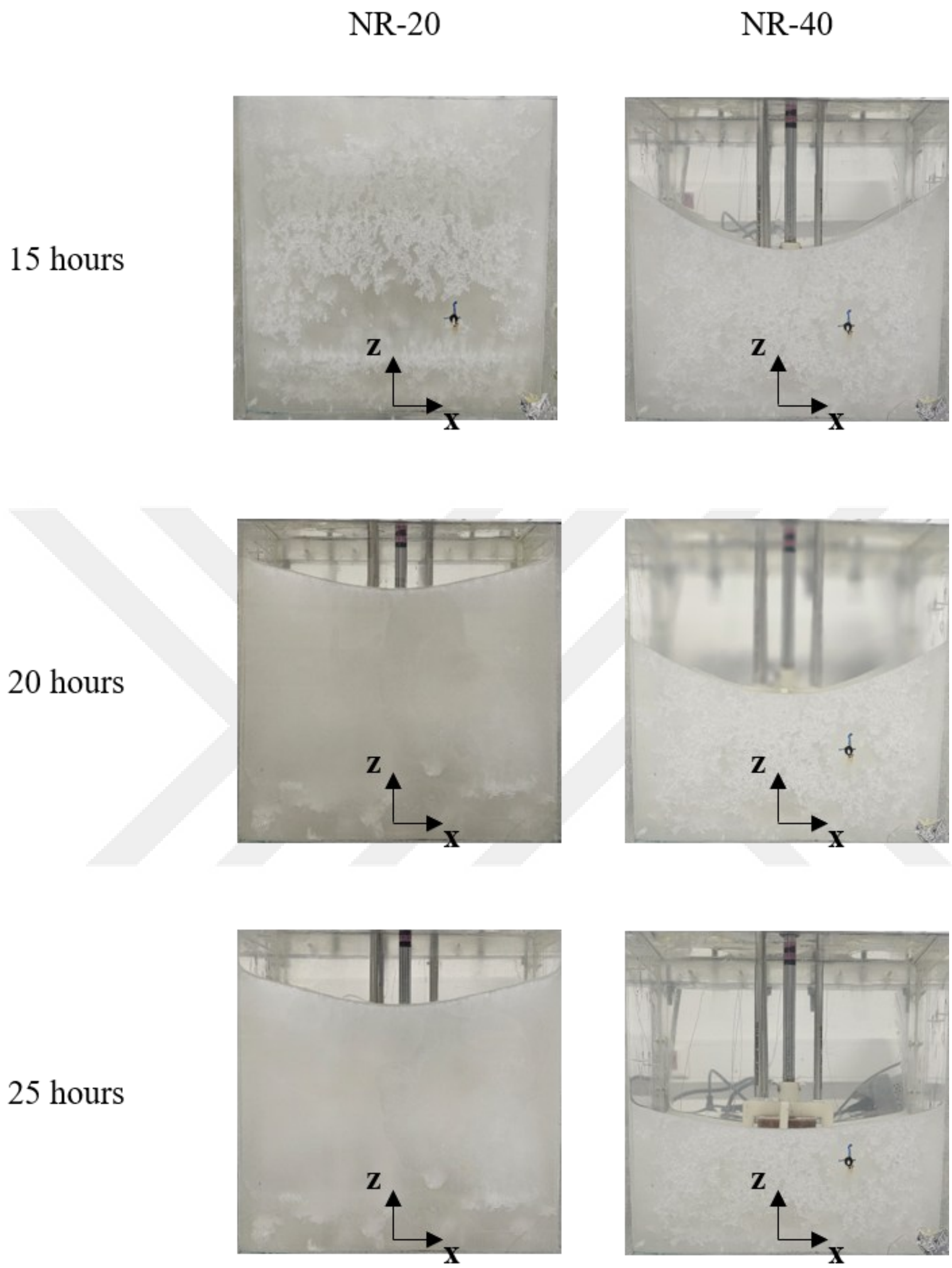

Figure 4.2 (continued) Melt front evolution for the non rotating configurations

NR-20 NR-40

30 hours

35 hours

40 hours

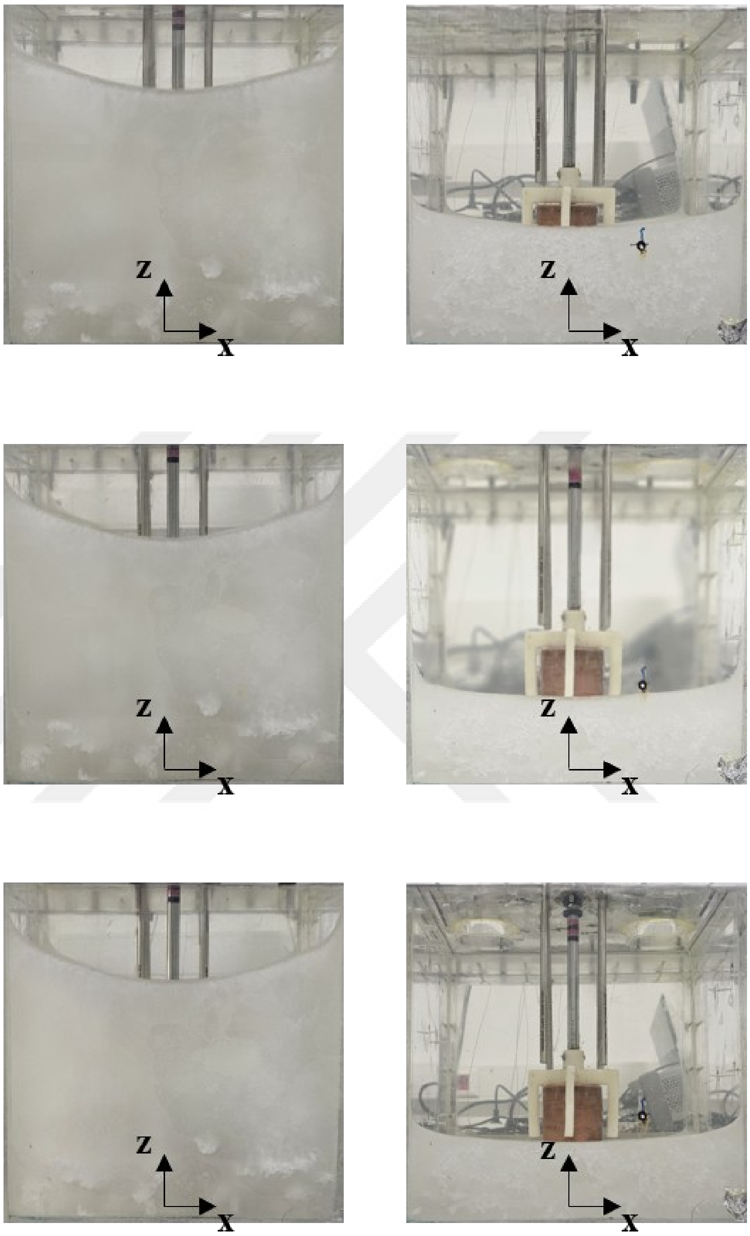

Figure 4.2 (continued) Melt front evolution for the non rotating configurations

Opting for a heat transfer rate of 40 W would significantly reduce the melting time, allowing 86% of the solid PCM to become liquid in 43 hours. The temperature profiles of some key points inside the cavity are also analyzed and presented in Figure 4.3.

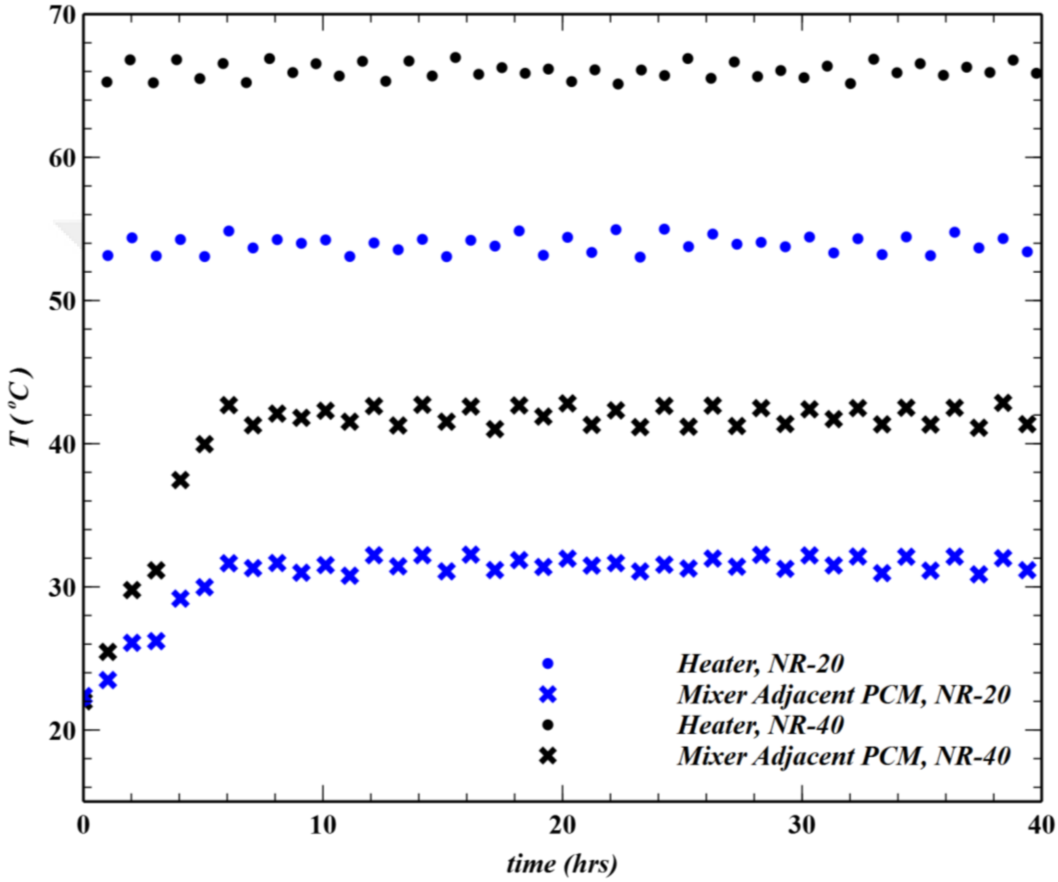

Figure 4.3 Temperature variations of key points for non rotating configurations

As mentioned earlier, to minimize any disturbance to the convection currents inside the domain, a limited number of TCs are placed. One of the TCs is located near the main heater, indicating the peak temperature of the cavity, and another is installed near the mixer to optimize the timing of rotation. According to Figure 4.3, for the NR-40 case, the temperature of the heater is raised to about 66°C after 5 hours of being heated at 40 W, whereas the heater temperature is 54°C for the NR-20 case. It is worth mentioning that mixer employment in the current arrangement for the case of NR-20 is not possible, as the temperature adjacent to the mixer blades never reaches the melting range of the PCM.

4.1.2 Rotation-Included Analyses

For the rotating cases, three different cases with rotational speeds of 5, 25, and 100 rpm for the mixers are studied, and their results are presented herein.

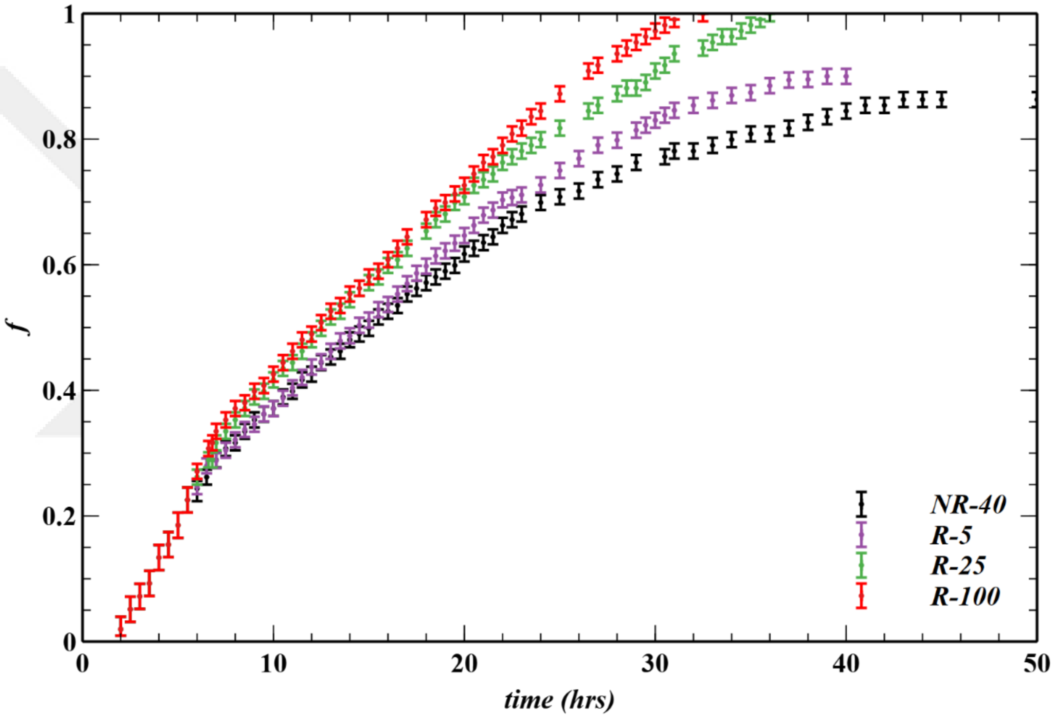

Figure 4.4 Liquid fraction of rotating configurations

The differences between the liquid fraction in rotating studies are not significant compared to those in non rotating configurations, as the heat transfer rates of the heater for all rotating studies are the same. Comparing Figure 4.1 and Figure 4.4 reveals that the R-100 case demonstrates a reduction in total melting time by 22%, to 32 hours, compared with the non rotating configurations. Another notable observation is the effect of utilizing the mixer even at the lower rotational speed, R-

5 case, which yet increases the liquid fraction at steady state by 4%, to nearly 90%. Only the mixer rotational speeds, which are representative of the intensity of forced convection, are altered. The evolution of liquid fractions remains nearly identical until 5.5 hours, as the mixer has not been rotating until that point. After the mixer starts to rotate, some differences become apparent.

As the rotational speed increases, melting accelerates noticeably due to improved convective mixing. R-25 fully melts in about 36 hours, while R-100 takes nearly 32 hours, confirming a reduction of around 4 hours or 22% at the higher speed. Although both R-25 and R-100 reach complete melting, their paths differ at intermediate times, where convection dominates heat transfer. In R-100, the liquid fraction surpasses R-25 by as much as 5%, indicating a nonlinear boost in convective transport. Conversely, the R-5 case melts much more slowly and does not reach full liquefaction, leveling off with a final liquid fraction of roughly 0.9. The inability of R-5 to undergo a complete phase change highlights that low-speed rotation cannot overcome conduction-dominated heat transfer, which is the final stage of melting. Given the current boundary conditions and setup, R-25 is the most suitable case to achieve complete PCM melting with the presented characteristics in Figure 4.5.

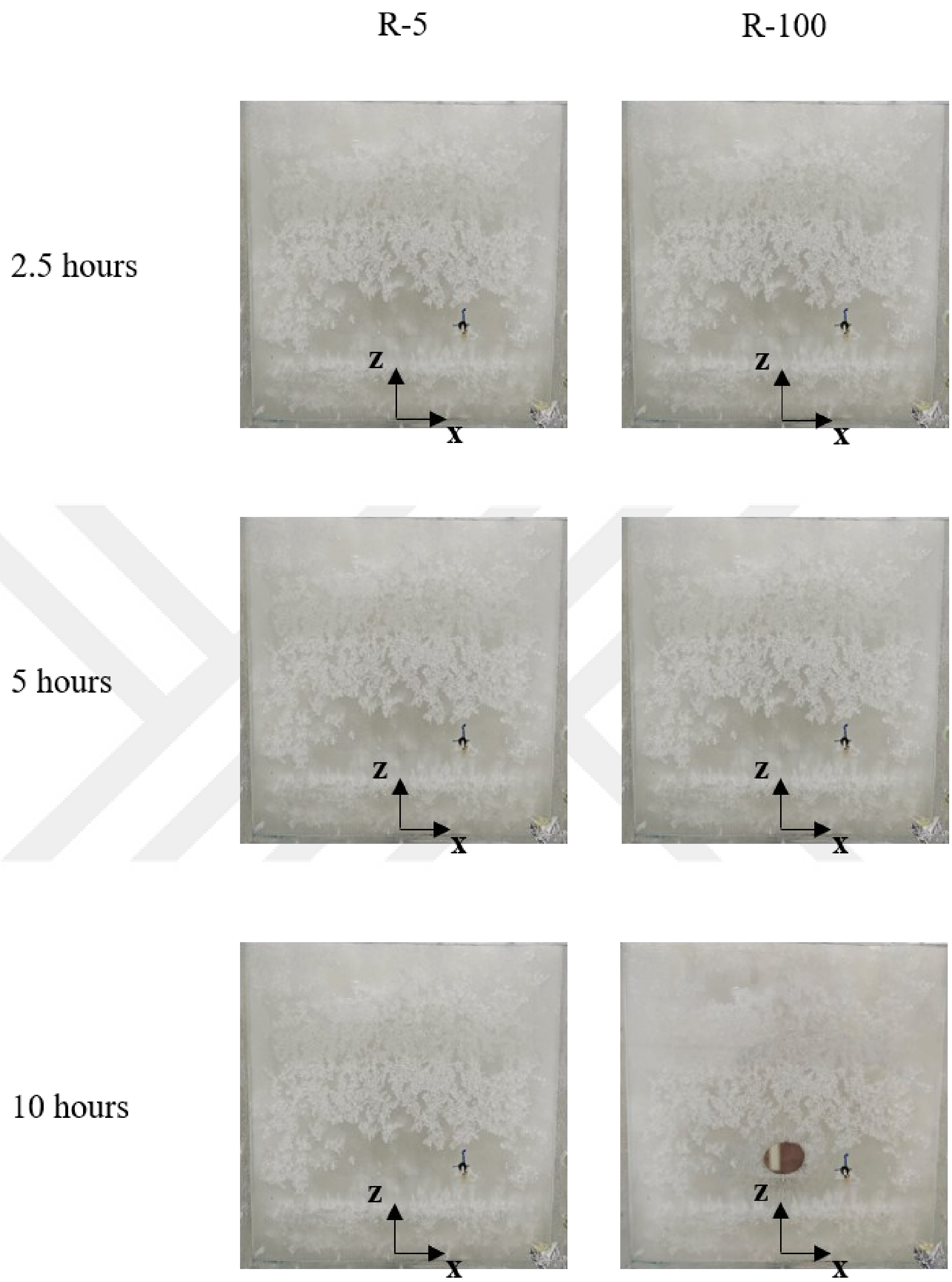

Figure 4.5 Melt front evolution for the rotating configurations

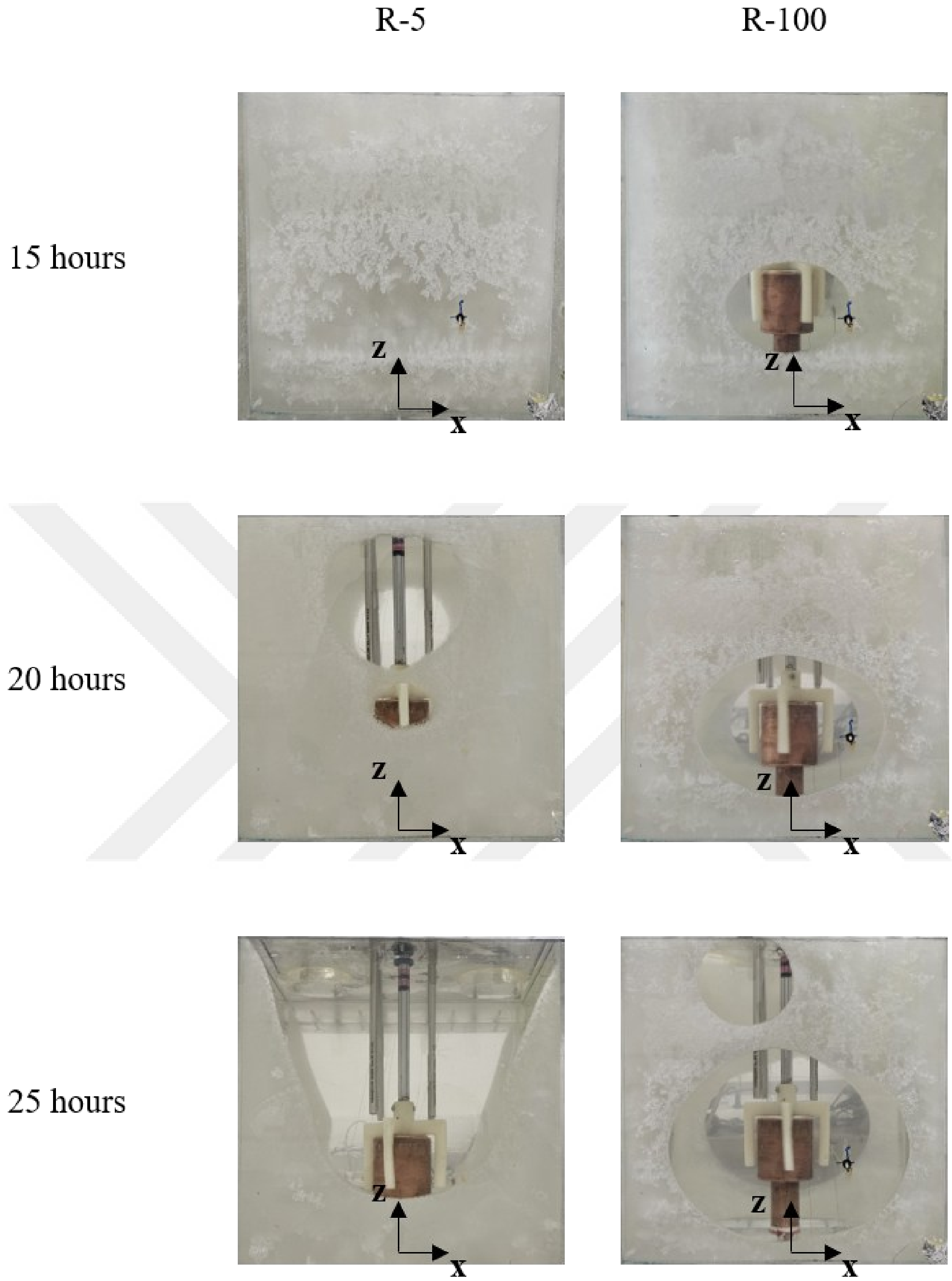

Figure 4.5 (continued) Melt front evolution for the rotating configurations

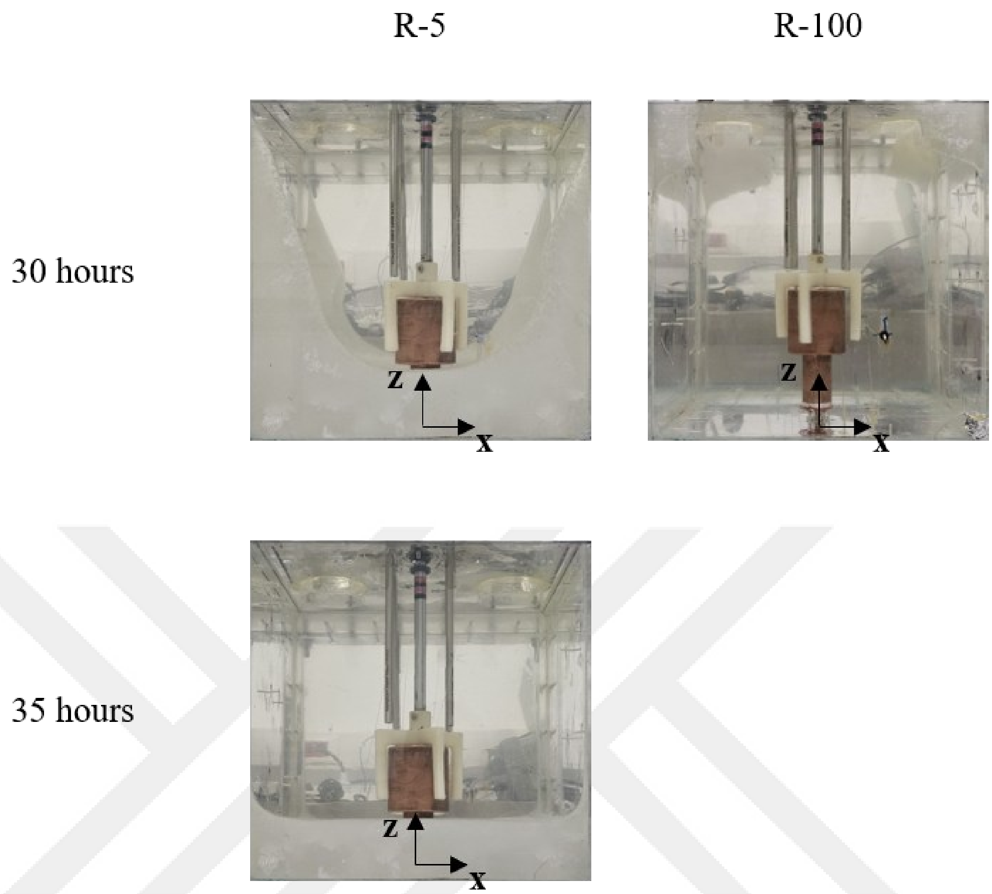

Figure 4.5 (continued) Melt front evolution for the rotating configurations

The rotational speed of the mixer could determine the melt front behavior along with the melting time. Reducing the rotational speed decreases the effect of forced convection, leading to a smaller visible hole of the melt front on the front wall compared to when the mixer rotates faster. Such observation indicates that the forced convection caused by the mixer is insufficient to melt more solid PCM adjacent to the front wall.

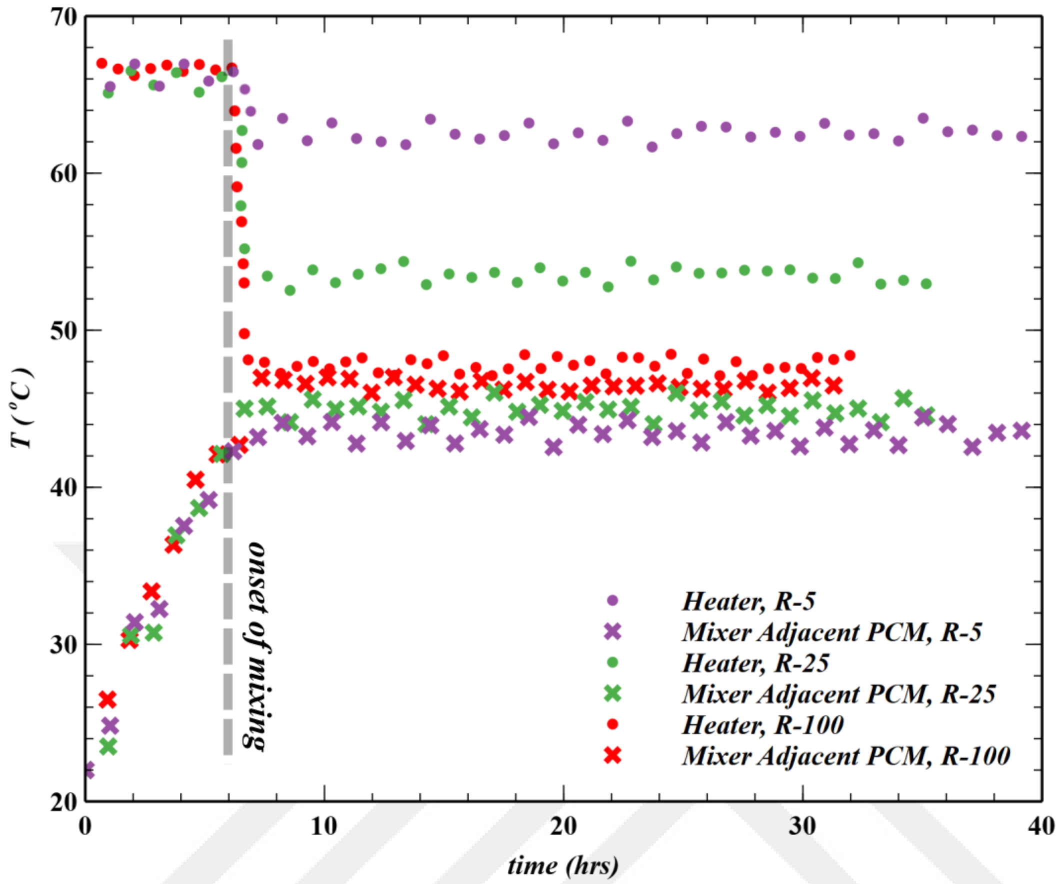

Figure 4.6 Temperature variations of key points for rotating configurations

Another aspect that needs to be discussed is the effect of forced convection on the homogenization of temperature in the melted PCM domain. As illustrated in Figure 4.6, in the R-5 case, the temperature readings indicate a lower impact of mixing compared to those observed at higher rotational speeds. The mean temperatures recorded at designated points of the heater and mixer adjacent are only altered to $63°C$ and $44°C$ from $66°C$ and $42°C$, respectively.

However, in the R-25 case, the mean temperatures for the heater and mixer adjacent locations shift to $54°C$ and $45°C$, indicating that increased speed contributes further to the homogenization of temperature profiles. When examining the R-100 case, temperature measurements reveal further adjustments, with $48°C$ at the heater and $46°C$ at the mixer adjacent points.

As the rotational speed of the mixer increases, the disparity in temperature between the heater and mixer adjacent points diminishes. By having smaller gaps between two key points inside the cavity, it is inferred that the possibility of sensible heat augmentation near the heat source is lower, allowing for higher heat transfer rates without the risk of reaching the temperature at which the PCM would chemically degrade. Additionally, the behavior of the liquid fraction, as depicted in Figure 4.4, exhibits a consistent pattern with the temperature profiles observed across the three rotational cases, thereby reinforcing the link between the liquid dynamics and temperature equilibrium within the system.

Having discussed the thermal enhancement resulting from the rotation of the liquid PCM, it is necessary to examine the power consumption of the mixer at varying rotational speeds. The parameter of MU is introduced, which is a dimensionless quantity used to quantify power consumption across various rotational configurations, where a higher MU indicates higher efficiency.

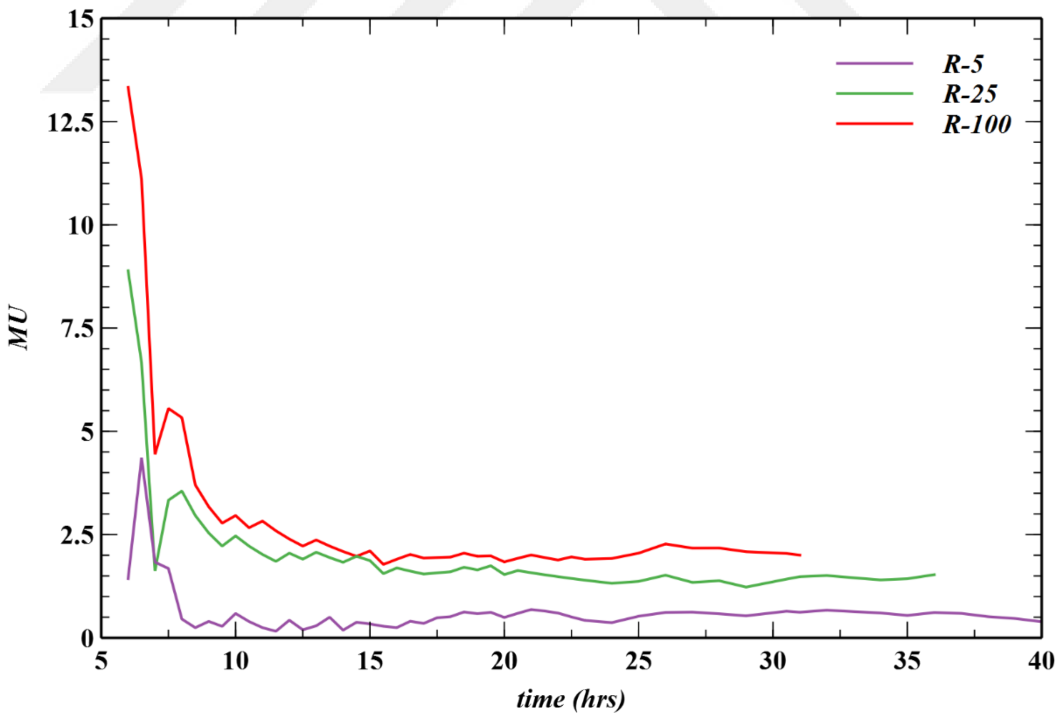

Figure 4.7 Mixer usefulness for rotational configurations

The MU value, depicted in Figure 4.7, for the R-5 case is considerably lower and can be up to one-tenth lower than the R-25 case. Conversely, in the case of R-100, MU values tend to be as high as 65% of the R-25 case. Higher MU values are attributed to the increased usefulness of the mixer, which enhances convective heat transfer during melting. However, it would be inferred that the option of higher rotational speeds would be more advantageous, especially during the first and last stages of melting. Prior to the convection-dominant stage and complete melting of the PCM, conduction is prominent, leaving more room for the convective currents to improve the thermal behavior. Utilization of the mixer at higher rotational speeds becomes more advantageous after approximately 80% of the PCM has been melted. Another subject examined during the experiments is the energy balance of system. For the calculations, Eqns. (3.9), (3.10), and (3.11) are employed. The derived values are presented in Table 4.1.

Table 4.1 Energy balance calculation in experiments

Case	**NR-20**	**NR-40**	**R-5**	**R-25**	**R-100**
$Q_h\ (kJ)$	2124	5378	4752	5472	5357
$Q_{aux}\ (kJ)$	1699	2151	1901	2189	2143
$W_{mix}\ (kJ)$	0	0	307	363	354
$Q_w\ (kJ)$	910	1853	1673	2094	2050
$Q_{et}\ (kJ)$	304	495	447	559	548
$Q_{sensible,s}\ (kJ)$	1114	2021	2066	2245	2245
$Q_{sensible,l}\ (kJ)$	168	481	492	535	535
$Q_{latent}\ (kJ)$	1280	2450	2505	2723	2723
Relative error (%)	**1.3**	**3.1**	**3.4**	**1.7**	**3.3**

The non rotating cases exhibit the expected trend in which a lower heater input is associated with a smaller error. Lower errors are attributed to uncertainties being mainly caused by convection, which scales with the temperature gradients and contributes less at lower input, along with decreased sensitivity to variations in PCM properties. In contrast, in the rotating configurations, which have similar heater inputs, the closure error does not change consistently with speed. The variability of error in the rotating configurations is due to additional uncertainties from the motor, shaft, and mixer itself, as well as estimates from electrical measurements, torque and speed fluctuations, and speed-dependent changes in the external heat transfer coefficient and free surface losses, factors that increase with mixing and are more difficult to quantify accurately. Across the experimental runs, the relative error between the left and right sides of the energy equation remained below ±3.4%, with an average closure error of 2.6%.

4.2 Numerical Results

This chapter begins with the validation of the numerical model through comparison with experimental findings. Subsequently, a comprehensive discussion is provided regarding parameters that could not be directly measured during the experimental studies. The chapter also examines the impact of compressibility on the melting dynamics of the PCM. Finally, benchmark studies are employed to further validate the accuracy and reliability of the numerical model.

4.2.1 3D Model Validation & Visualization of Phase Change Dynamics

First, 3D case studies are discussed, which consist of two different case studies differing in the heat transfer rate of the main heater. The discussion begins with the NR-40 case, and the evolution of its liquid fraction is illustrated in Figure 4.8.

The evolution of the liquid fraction during PCM melting is analyzed by comparing experimental data with numerical results across different C_{mush}. Among the evaluated values, C_{mush} of 10^6 stands out as the most suitable and validated option. However, it is important to note that during the initial stages of melting ($f < 0.3$), there are noticeable deviations, with mean errors reaching up to 30%. These discrepancies are primarily linked to the experimental setup's lower accuracy at the initial stages of the melting process.

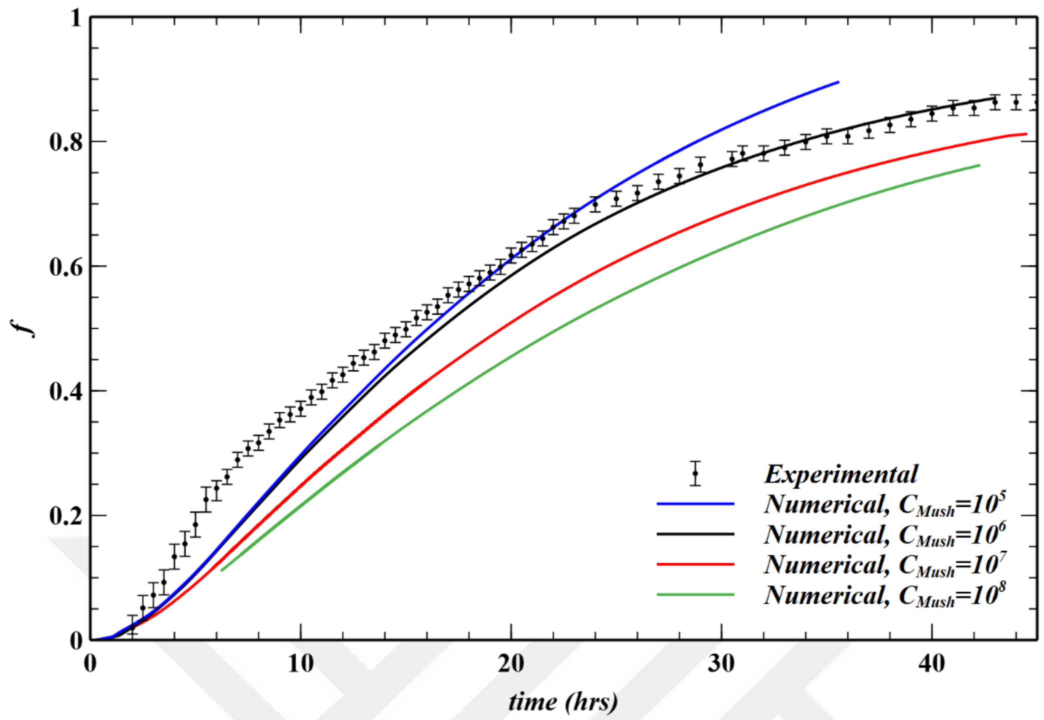

Figure 4.8 Liquid fraction evolution for NR-40

However, the mean error for the chosen C_{mush} is about 6% over the whole period. To narrow down the discrepancy specifically at the early stages, the use of the Boussinesq approximation, which assumes constant density except in buoyancy terms, can be addressed instead of compressive models such as the VoF method. Although the PCM has about a 12% expansion rate, it cannot be captured during modeling using the Boussinesq approximation method. As PCM expands, the natural convection currents are altered accordingly, leading to an underprediction of the experimental results [118, 119].

In the early stage, all curve patterns, including those with varying C_{mush} values, are closely aligned, as heat transfer is primarily influenced by conduction, with convection effects being minimal. As the process progresses and natural convection becomes more pronounced, the choice of C_{mush} has a significant impact on the results. For example, the C_{mush} of 10^5 starts to diverge during the final stages, overestimating the steady state liquid fraction by about 7% due to excessive convection arising from inadequate resistance in the mushy region. This overestimation results in a more rapid and complete melting than what is observed experimentally, which is not a physically accurate representation. Consequently, despite indicating reasonable agreement during intermediate phases, the C_{mush} of 10^5 is not chosen. Conversely, the C_{mush} of 10^6 consistently stays within an acceptable error margin throughout the melting process. When considering the experimental results with confidence bars, the numerical predictions for C_{mush} of 10^6 align closely, further supporting its choice as the validated solution.

By selecting the most suitable C_{mush} for the computational domain, the visual outcomes of the numerical results are compared with an emphasis on the melt front from the front view, as presented in Figure 4.9.

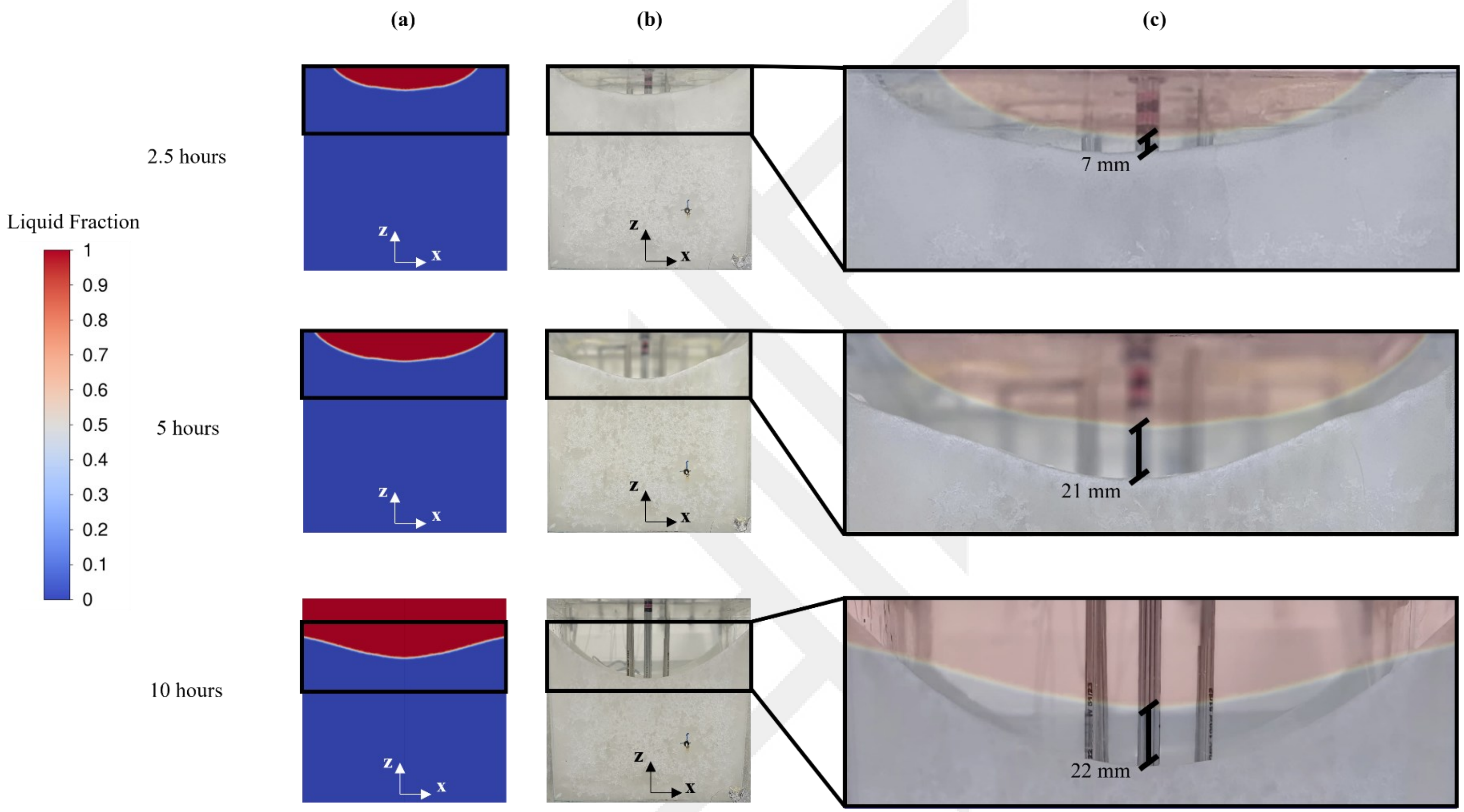

Figure 4.9 Melt front evolution **(a)** numerical, **(b)** experimental, and **(c)** overlay for NR-40

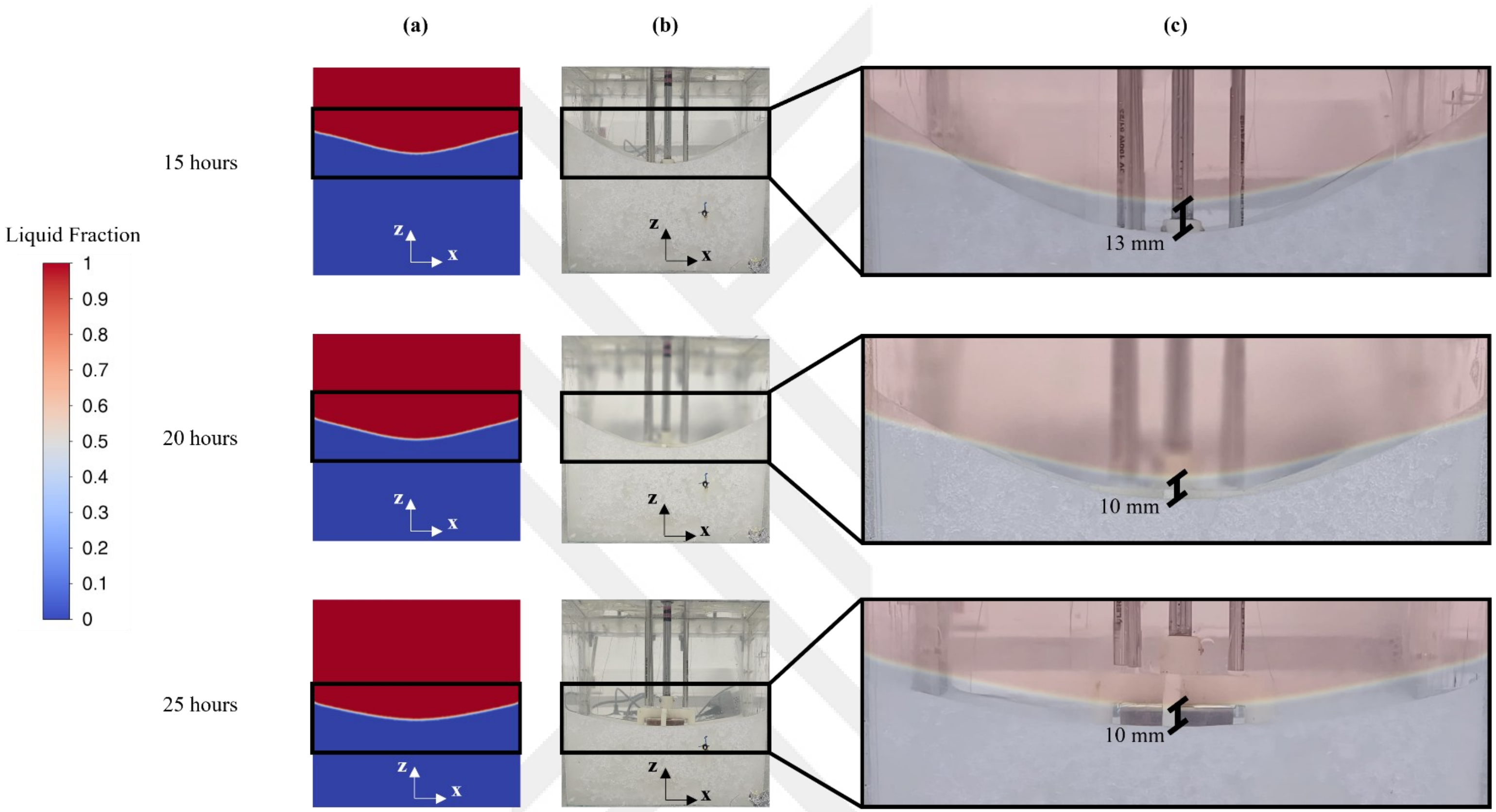

Figure 4.9 (continued) Melt front evolution **(a)** numerical, **(b)** experimental, and **(c)** overlay for NR-40

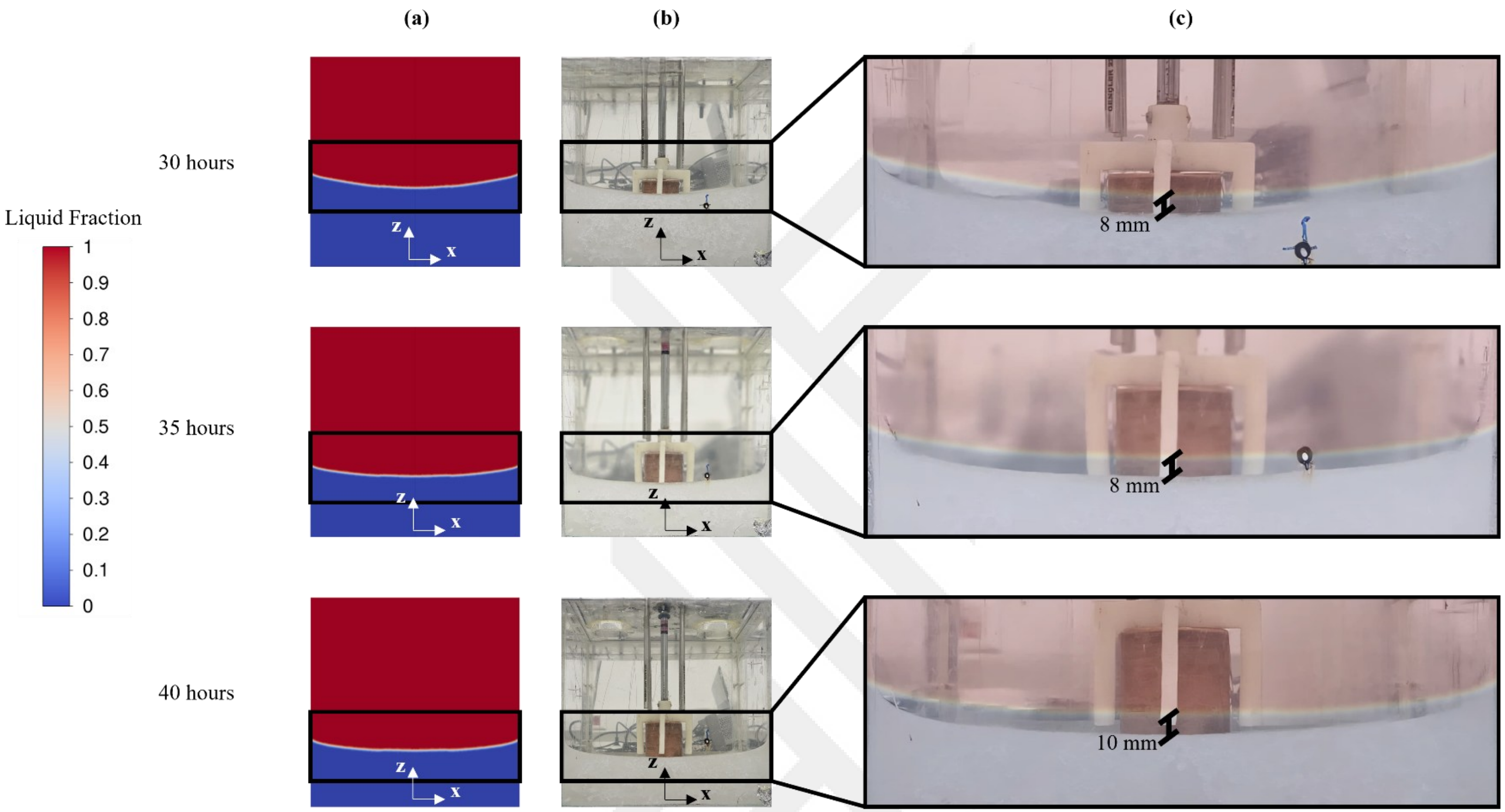

Figure 4.9 (continued) Melt front evolution **(a)** numerical, **(b)** experimental, and **(c)** overlay for NR-40

The numerically rendered results are in acceptable agreement with the melting front of the experimental study results. For the first 10 hours of the experiment, there are some errors within the acceptable range, which stem from the inaccuracies of the experimental setup itself. Considering the difference between the lower end of the melt front, at the 10th hour of the experiment, a 22 mm difference is observed, which accounts for 7.8% of the relative error.

It is crucial to understand that the differences in liquid fraction percentages between numerical simulations and experimental results cannot be solely attributed to the comparison of the melt front. Such a discrepancy in the liquid fraction primarily arises from a third-dimensional factor, the depth of the cavity. Figure 4.10 is presented to understand the effect of 3D melting behavior better, which is recorded 25 hours after initiation of the NR-40 experiment.

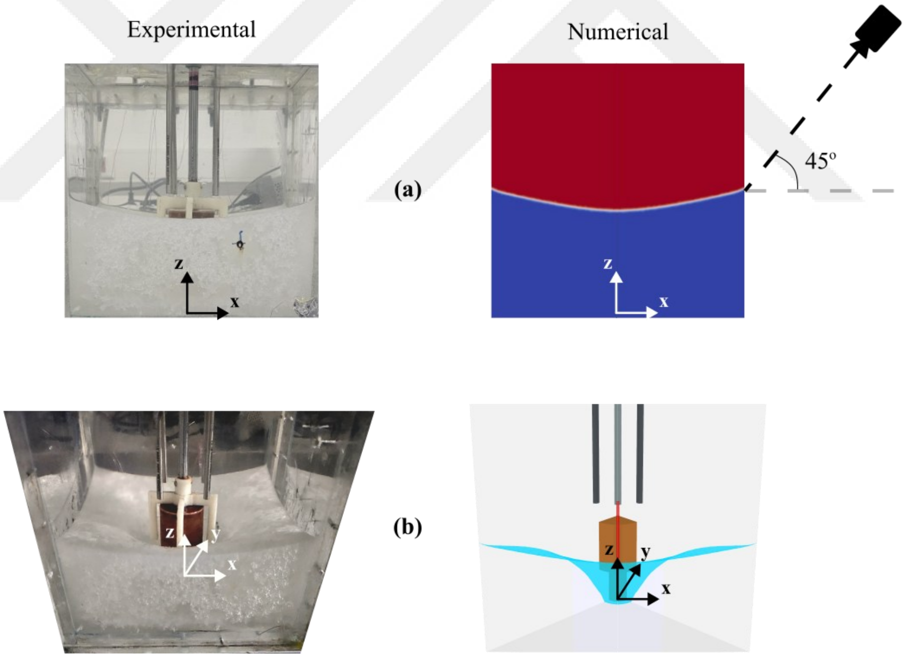

Figure 4.10 Melt front in 3D representation **(a)** front and **(b)** lateral views

It is observed that the melt front profile in the y-direction is quite complex. Nevertheless, the numerical results align closely with the experimental findings. Close to the main heat source at the center of the cavity, the melting depth (in the z-direction) is significantly greater than that at the walls. Such trend arises from the prominence of natural convection in the non rotating configurations, leading to a deeper liquid PCM than what is found near the walls. Experimental results confirm the occurrence of natural convection, as depicted in Figure 4.11.

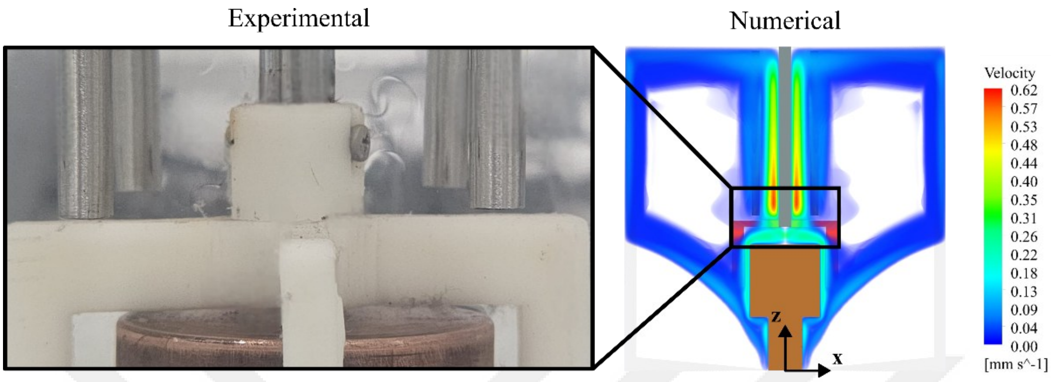

Figure 4.11 Observation of natural convection currents

The velocity values of the numerical results confirm the higher melting rate near the main heater. As illustrated in Figure 4.11, which is captured 25 hours after the experiment has begun, the velocity in the specified location can reach up to $0.5\ mm/s$. Additionally, natural convection currents, which move upward through the cavity, are visually identified by the formation of thermal plumes.

The temperature profiles of the domain depicted in Figure 4.12 indicate that the melt front appearing on the wall has a temperature near the end of the melting range, about $43°C$.

Similar temperature readings are recorded during the NR-40 case experiment, and the measurements from TC No. 26, located inside the vertical wall of the cavity and marked with a black cross, are validated. In a similar manner, temperature readings of heater and mixer adjacent PCM are compared with numerical results, which are illustrated in Figure 4.13. The first 1.5 hours are presented as the temperature variations are comparatively higher. Relative arrangement of the TCs is represented in Figure 3.5. When considering the temperature readings of the TC, it should be noted that $\pm 1°C$ is the relative uncertainty of the TC utilized during the experiments.

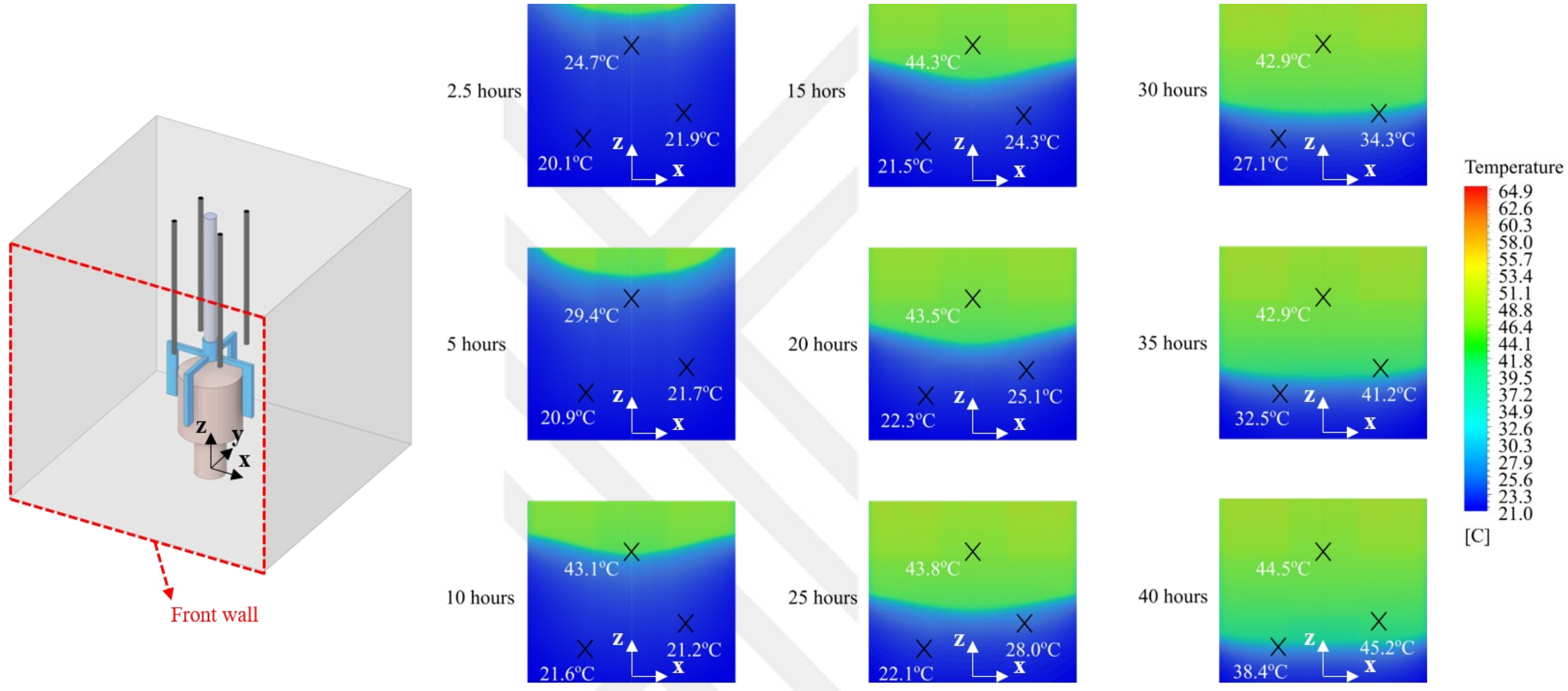

Figure 4.12 Temperature profiles of front wall for NR-40

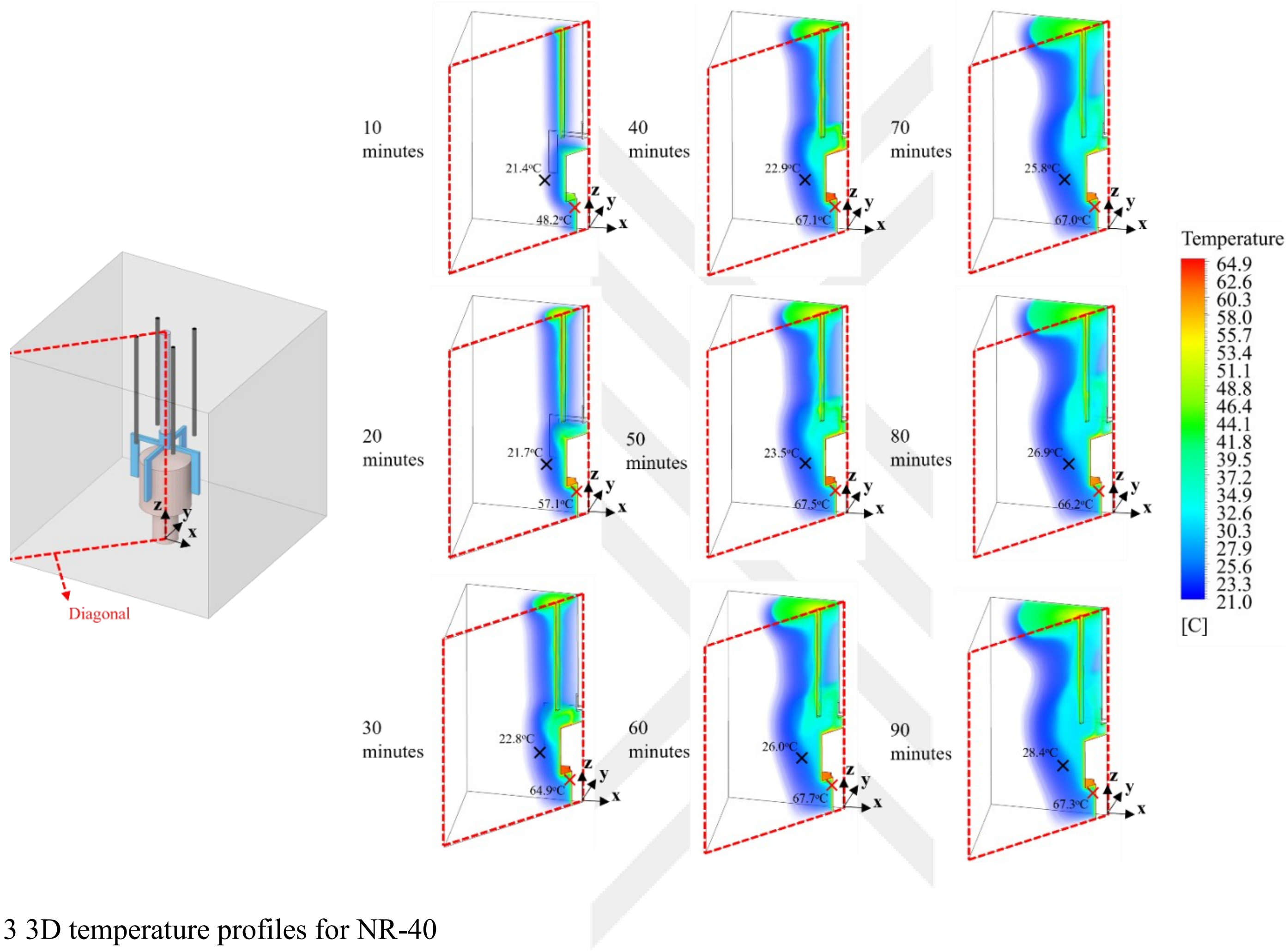

Figure 4.13 3D temperature profiles for NR-40

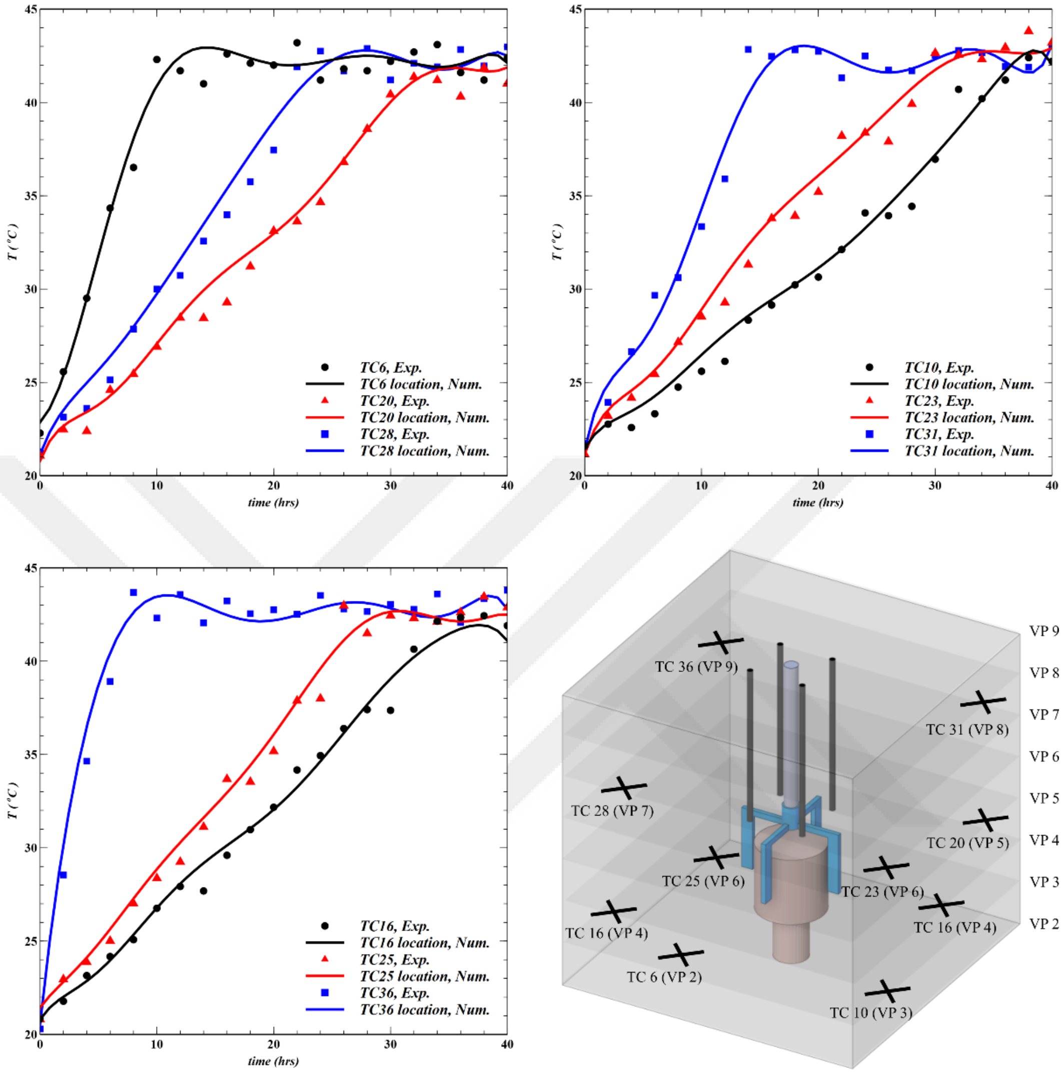

Figure 4.14 Temperature evolution for NR-40

TC readings in NR-40 experiments, as presented in Figure 4.14, had a relative error of up to 6.3% compared to the corresponding numerical simulation results. Such error is attributed not only to uncertainties in measurement devices but also to the assumptions made during the numerical studies. In the second case of the 3D study, a heat transfer rate of 20 W is assigned to the main heater. NR-20 case builds upon the findings and considerations from the previous case (Figure 4.15). Consistent with the earlier analysis, C_{mush} of 10^6 has been selected to ensure precision in analyses and validation with the corresponding experimental findings.

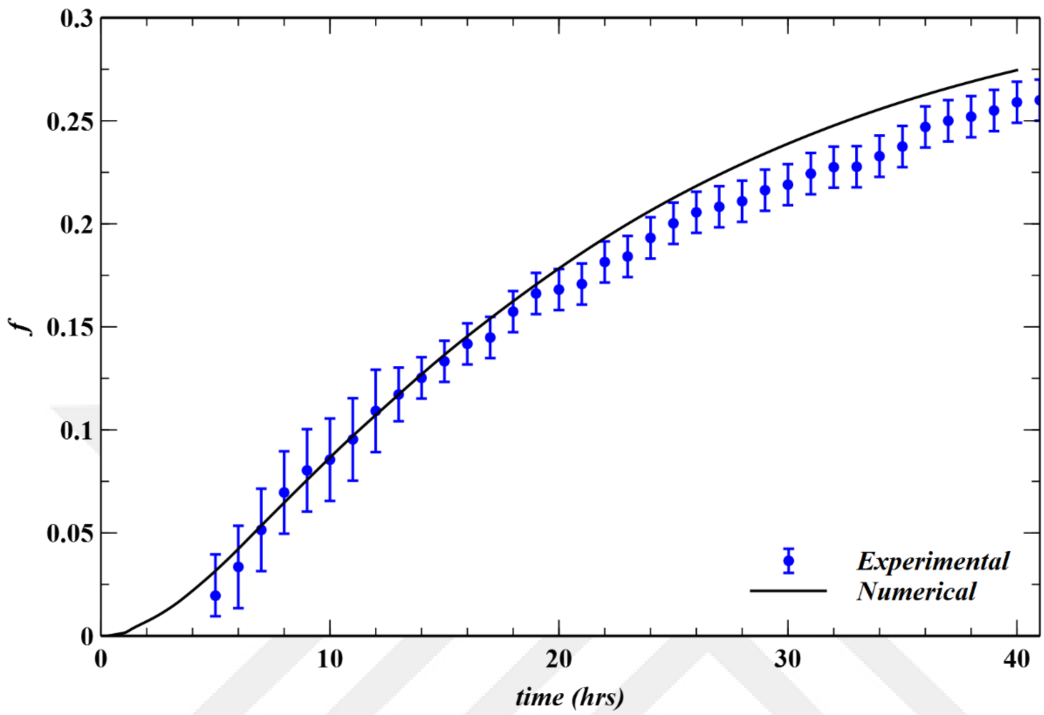

Figure 4.15 Liquid fraction evolution for NR-20

The disparity between the numerical simulations and the experimental results is significantly reduced when compared to the NR-40 case. Notably, the relative error observed can reach as high as 11% during the later stages of the melting process. Although the tendency to underpredict the experimental results while utilizing the Boussinesq approximation, the relatively minor discrepancy between the experimental and numerical results at lower heat transfer rates is attributed to the diminished influence of natural convection, coupled with the comparatively greater impact of conduction [118–120]. When the heat transfer rate for the main heater is halved, the necessary heat input to melt the entire cavity is not produced. Consequently, at a liquid fraction of approximately 0.28, the system achieves a steady state condition, which also corresponds with the numerical findings. To facilitate the analysis, the visualization of the melt front is presented in Figure 4.16.

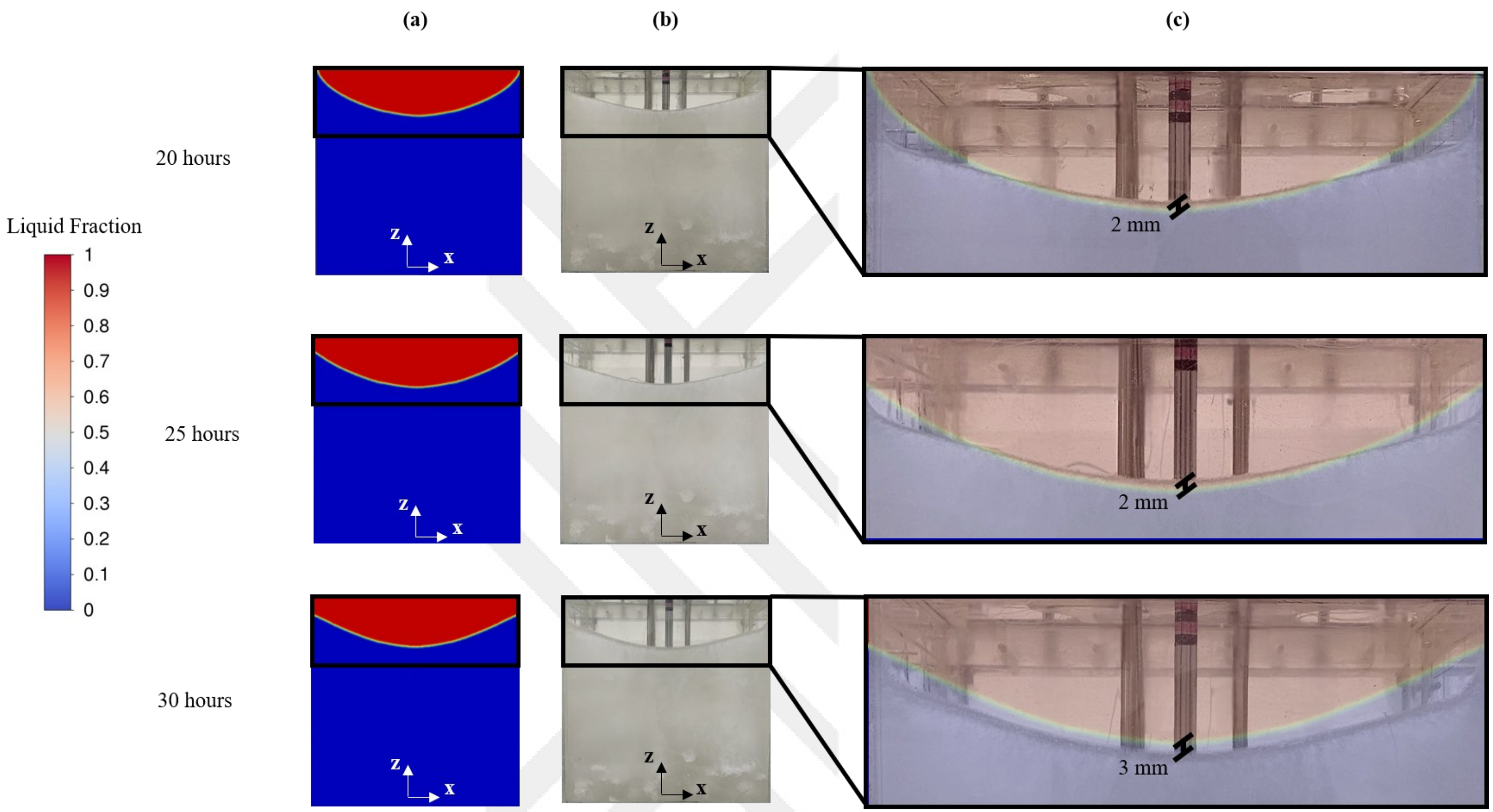

Figure 4.16 Melt front evolution **(a)** numerical, **(b)** experimental, and **(c)** overlay for NR-20

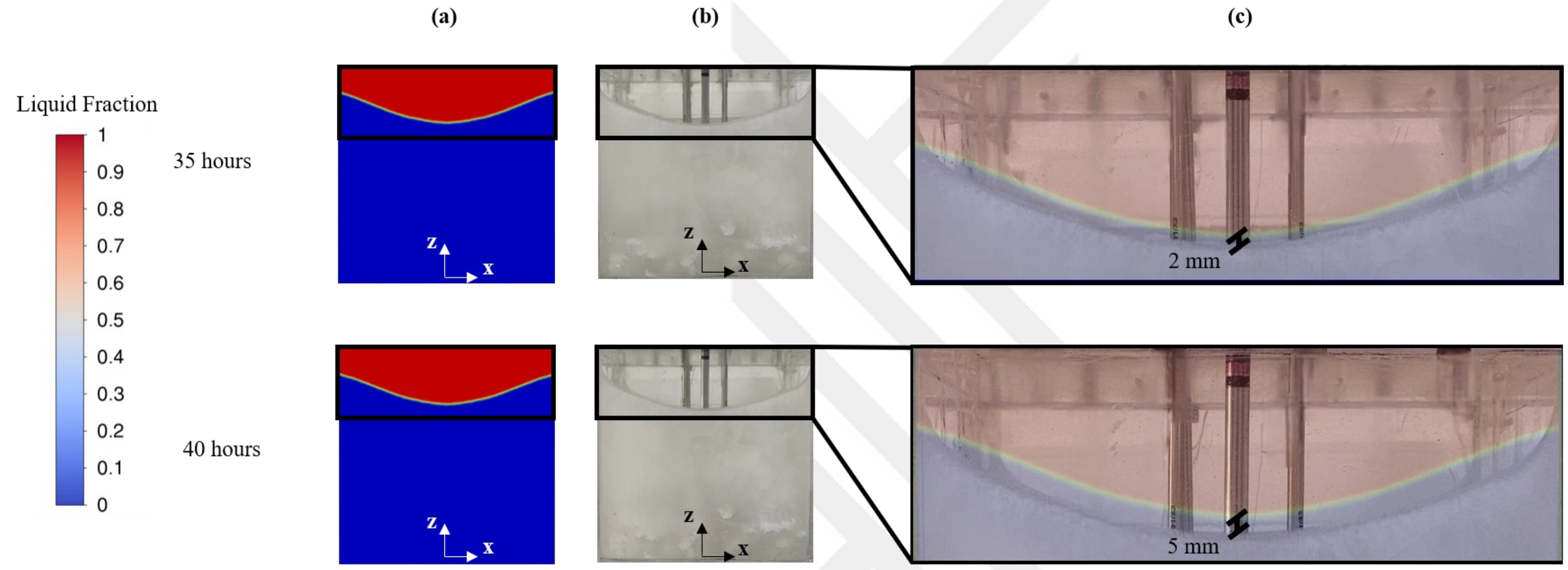

Figure 4.16 (continued) Melt front evolution **(a)** numerical, **(b)** experimental, and **(c)** overlay for NR-20

The discrepancy in the simulation results is significantly lower compared to cases that utilize a higher heat transfer rate, which aligns with the findings of the liquid fraction evolution plot. The enhancement in simulation accuracy at lower heat transfer rates is attributed to the reduced intensity of natural convection currents present. These currents tend to increase the complexity of numerical simulations at elevated heat transfer rates. Furthermore, during the experiments, a maximum relative error of only 2.4% is observed, which becomes most noticeable after 40 hours from the start of the experiment.

Once validated against both experimental measurements and established benchmark studies, the numerical models gain the credibility needed for broader use. They might be used to examine parameters that are difficult or impossible to measure experimentally, such as detailed local velocity fields, phase distribution, or transient thermal gradients within the PCM. Additionally, these models allow for analysis of operating conditions and design setups that are impractical, too costly, or not yet studied experimentally. Such capability not only broadens the scope of analysis beyond physical testing limits but also offers a predictive tool to guide future experiments and improve system performance.

The velocity contour series in Figure 4.17 illustrates the development of natural convection throughout the entire melting process. In the early stages, a confined flow region forms next to the auxiliary heater, where localized melting begins. The flow remains highly asymmetric, with higher velocities, approximately 0.4 mm/s, on the right side due to faster melting caused by a thinner PCM layer. Convection is mainly vertical and laminar there, driven by steep thermal gradients near the heating surface. As melting continues, the liquid PCM increases, and the flow becomes more complex and spread out. The convective plume widens, and secondary circulation cells start to form in the lower corners, indicating the start of recirculating flow loops that enhance mixing.

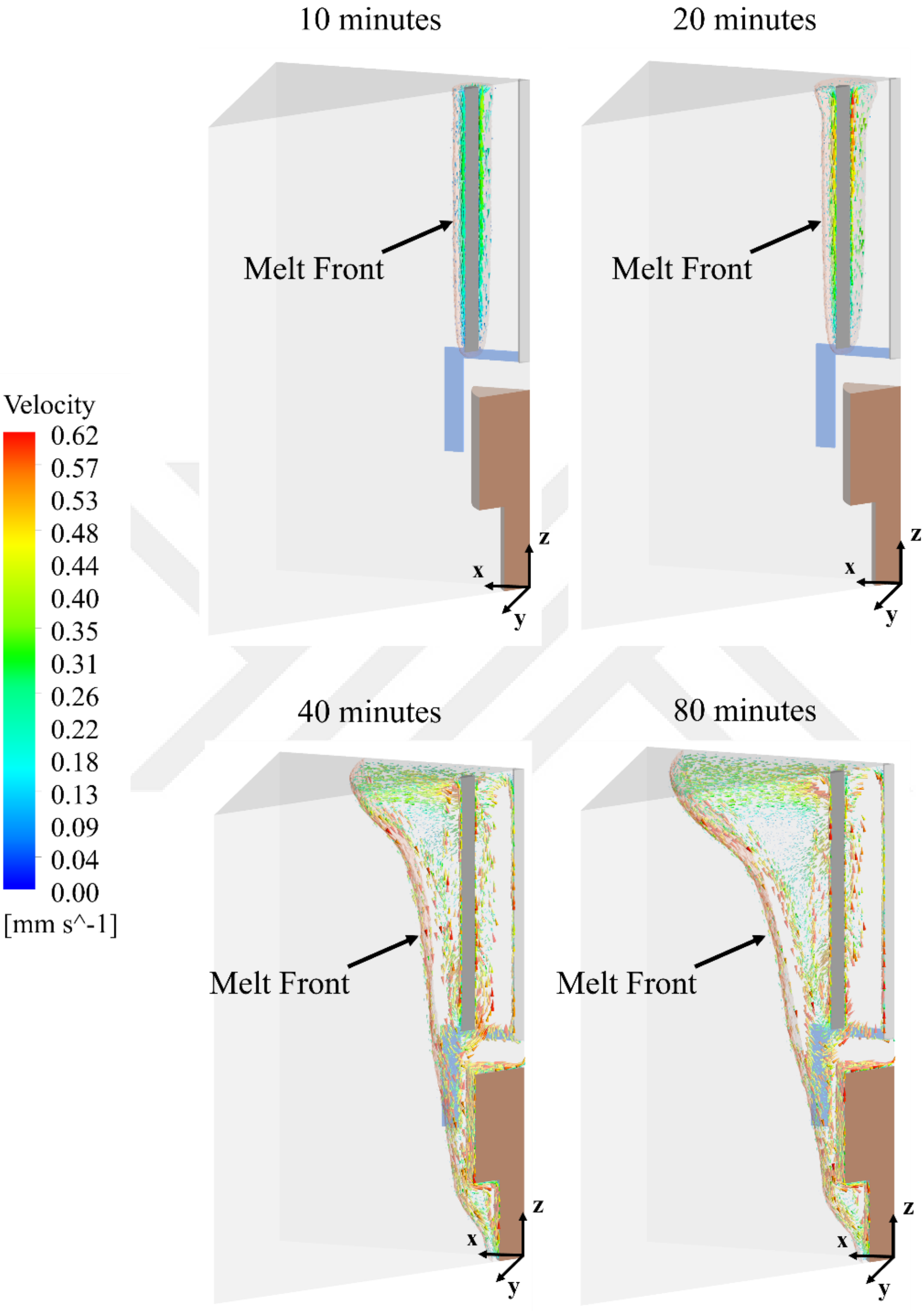

Figure 4.17 3D melt front evolution and velocity contours for NR-40

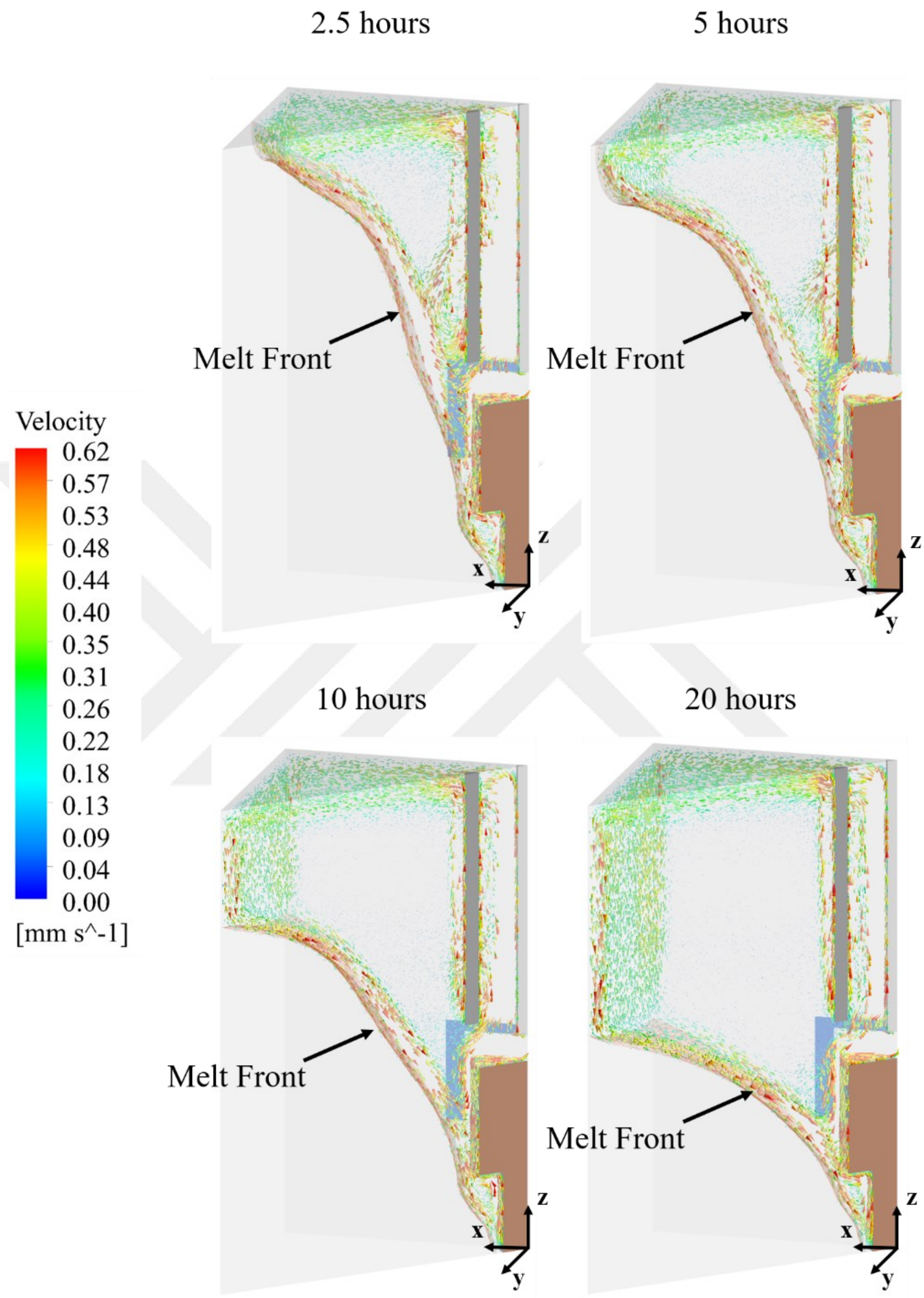

Figure 4.17 (continued) 3D melt front evolution and velocity contours for NR-40

To clarify the flow behavior and phase interface development, Figure 4.18 illustrates the detailed convective structure near the heater, the stagnant zones in the lower cavity, and the circulation patterns influenced by the cavity shape and boundary conditions.

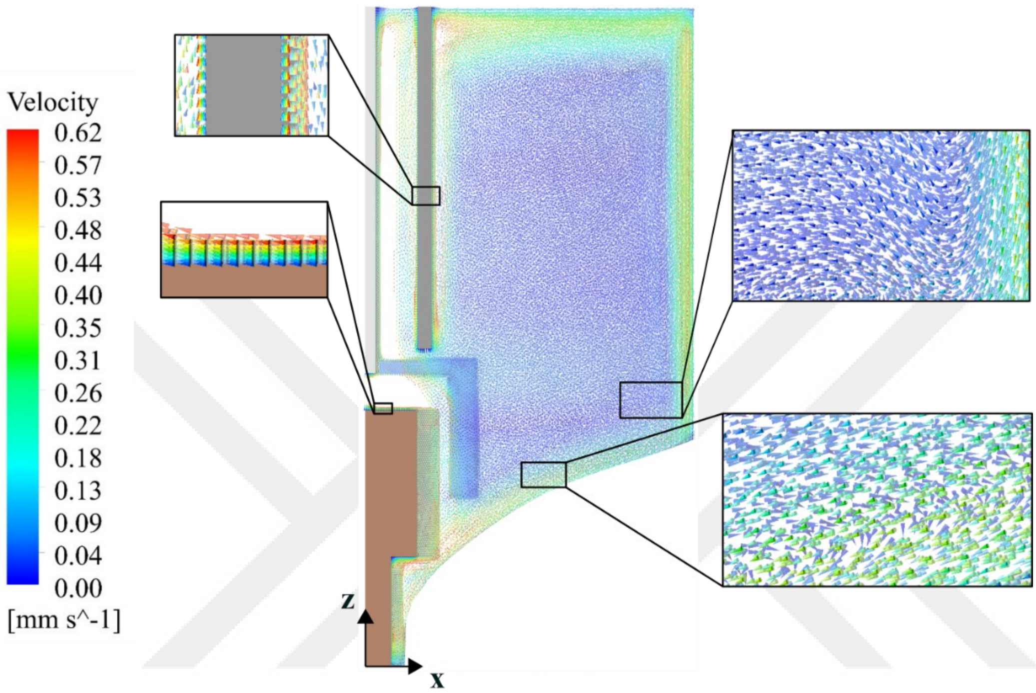

Figure 4.18 Cross-sectional view of normalized velocity vectors for NR-40

The top-left inset confirms the asymmetric flow behavior around the auxiliary heater, but conversely to the first stages of melting, which accounts for the weak convection currents on the left-hand side due to the lower thermal stratification. Considering the middle-left inset, in the melted region adjacent to the heated lower wall, a horizontal flow layer develops, with velocities reaching up to 0.6 mm/s, because the warmer fluid cannot ascend readily through the cooler, denser liquid above. This phenomenon is attributable to thermal stratification, which diminishes buoyancy forces. Consequently, the heated fluid propagates laterally along the bottom, forming a thin shear layer. The descending flow deviates from its vertical path near the cavity base due to thermal stratification and decreasing buoyancy forces. Lateral redirection becomes more pronounced near the vertical location of the main heater, where the downward flow balances the upward flow along the heated surface. The right-hand side insets illustrate the early development of a secondary recirculation cell, characterized by horizontal turning and upward return, confirming localized convective looping caused by flow imbalance and cavity shape.

As illustrated in Figure 4.19, with a reduced heat input of 20 W, the velocity field stays weak and confined, reaching a peak of about 0.17 mm/s, much lower than in the higher heat rate case of 40 W. The flow remains closely attached to the auxiliary heater, forming a narrow, buoyant plume with minimal sideward spread. The limited thermal forcing observed delays the development of large-scale convective structures, keeping fluid motion mainly near the heat source.As a result, natural convection remains underdeveloped, and thermal stratification persists across most of the domain. Secondary circulations, observed in the higher heating rate case, are missing here due to insufficient buoyancy strength. The system remains in a conduction-dominated stage for a longer period, resulting in slower melt front progress and reduced convective heat transfer. Comparison between the NR-40 and NR-20 cases highlights the strong dependence of flow morphology and phase change dynamics on the applied heat flux. Furthermore, another property that can be visualized through numerical studies is the temperature distribution behavior of PCM within the cavity.

Comparing Figure 4.3 and Figure 4.12, which present experimental data and 2D numerical temperature profiles, with Figure 4.20 reveals some discrepancies in readings. 3D numerical simulations typically predict lower peak temperatures and exhibit delayed thermal responses compared to experimental observations. This discrepancy arises from the inherent simplifications in numerical models, such as uniform initial conditions, constant thermophysical properties, and idealized boundary conditions, which may not accurately reflect the actual conditions. In 3D domains, heat can dissipate through more spatial directions, resulting in greater thermal losses and lower local temperatures. The observed peak temperatures of 67.3°C in the experiment, 66.2°C in the 2D model, and 64.9°C in the 3D model illustrate how dimensionality influences the thermal behavior of PCM systems.

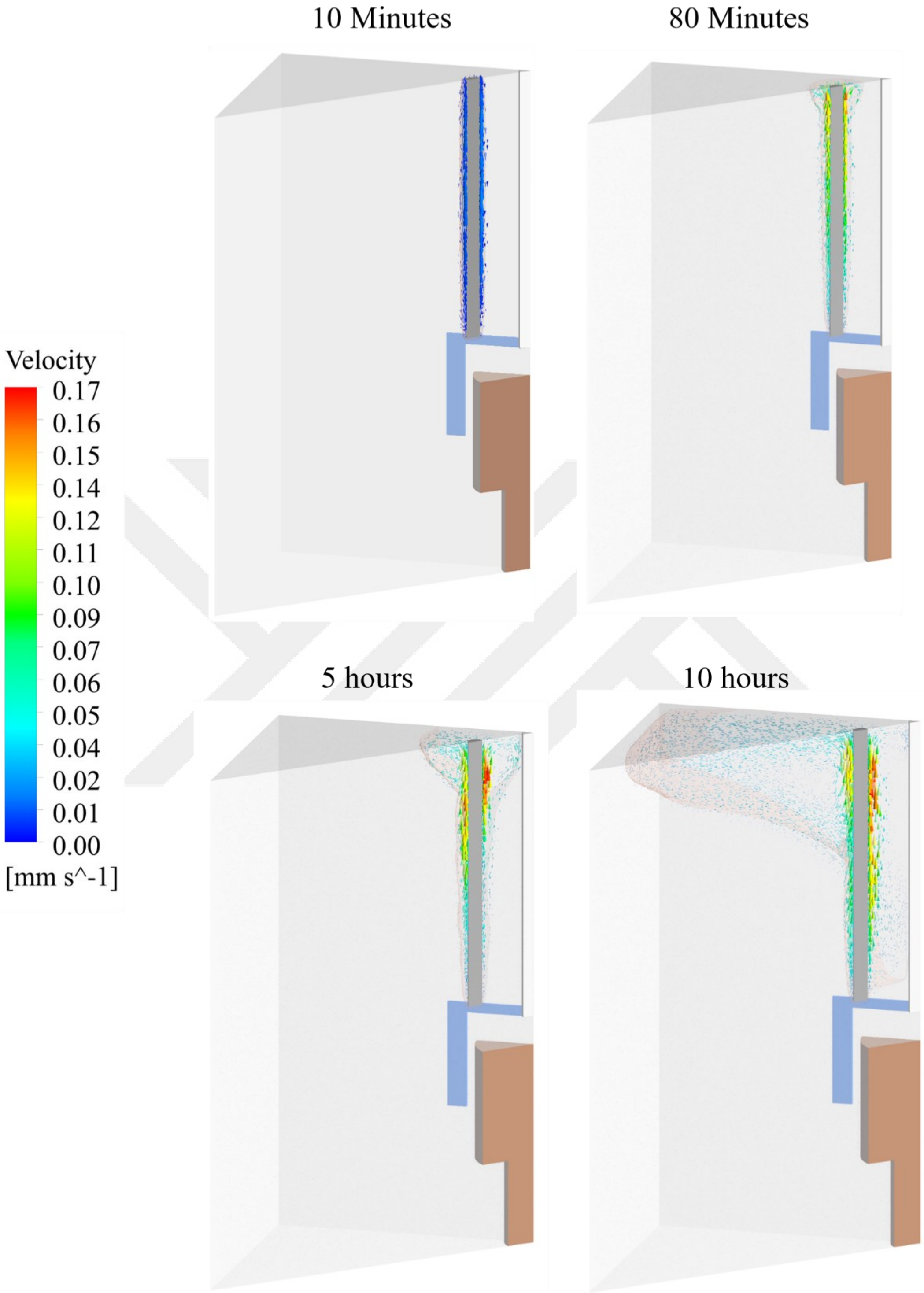

Figure 4.19 3D melt front evolution and velocity contours for NR-20

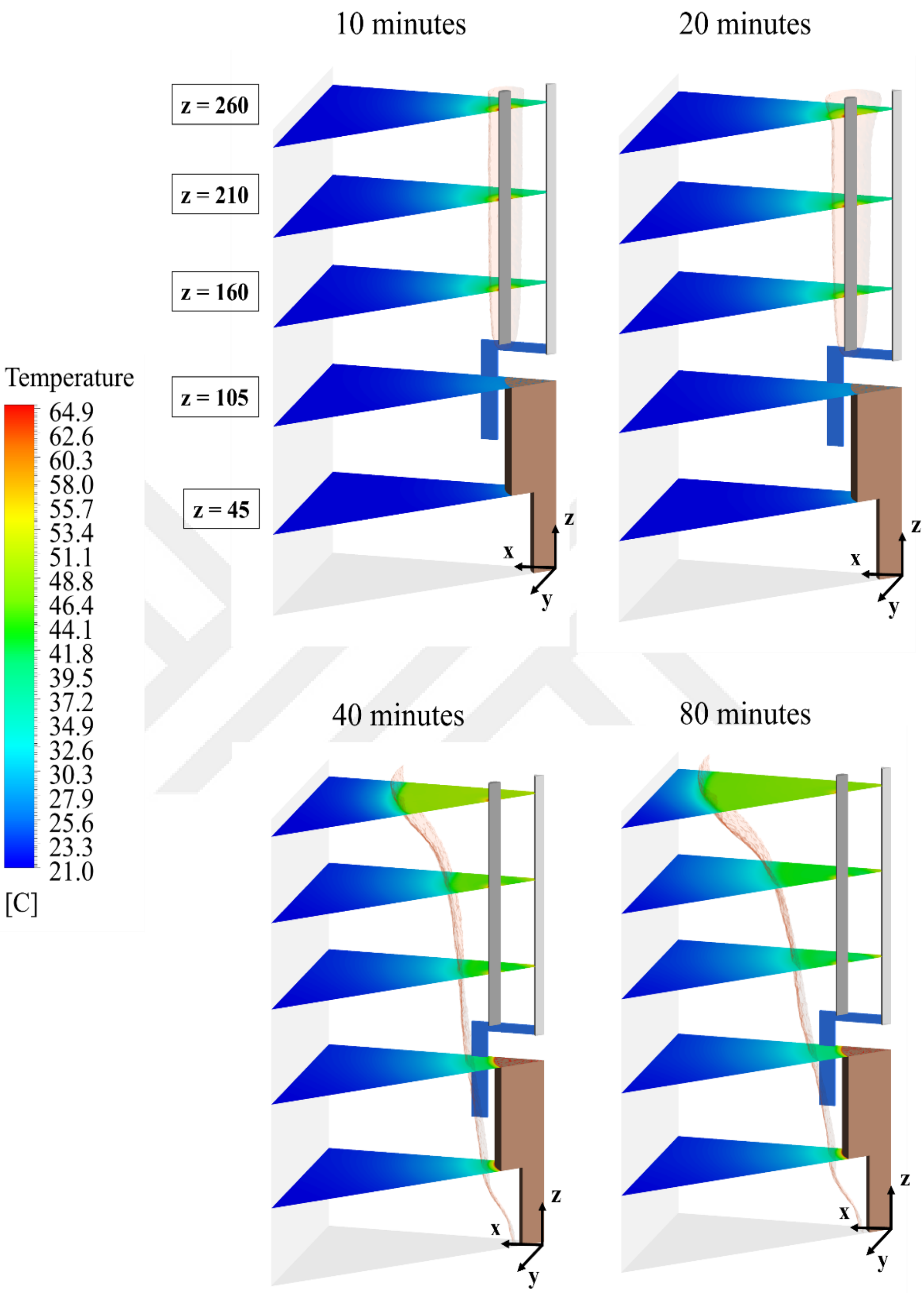

Figure 4.20 Temperature profiles for NR-40

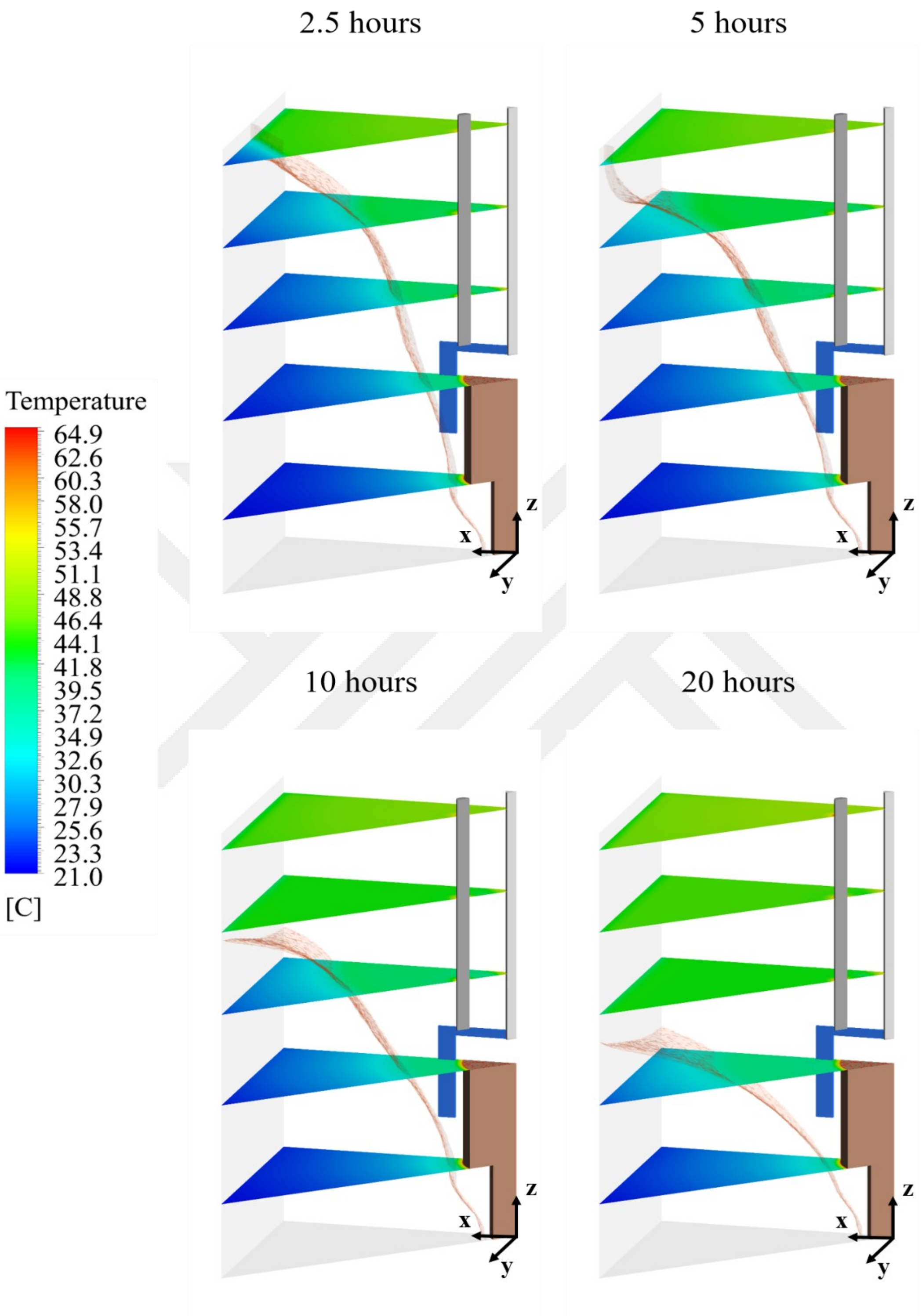

Figure 4.20 (continued) Temperature profiles for NR-40

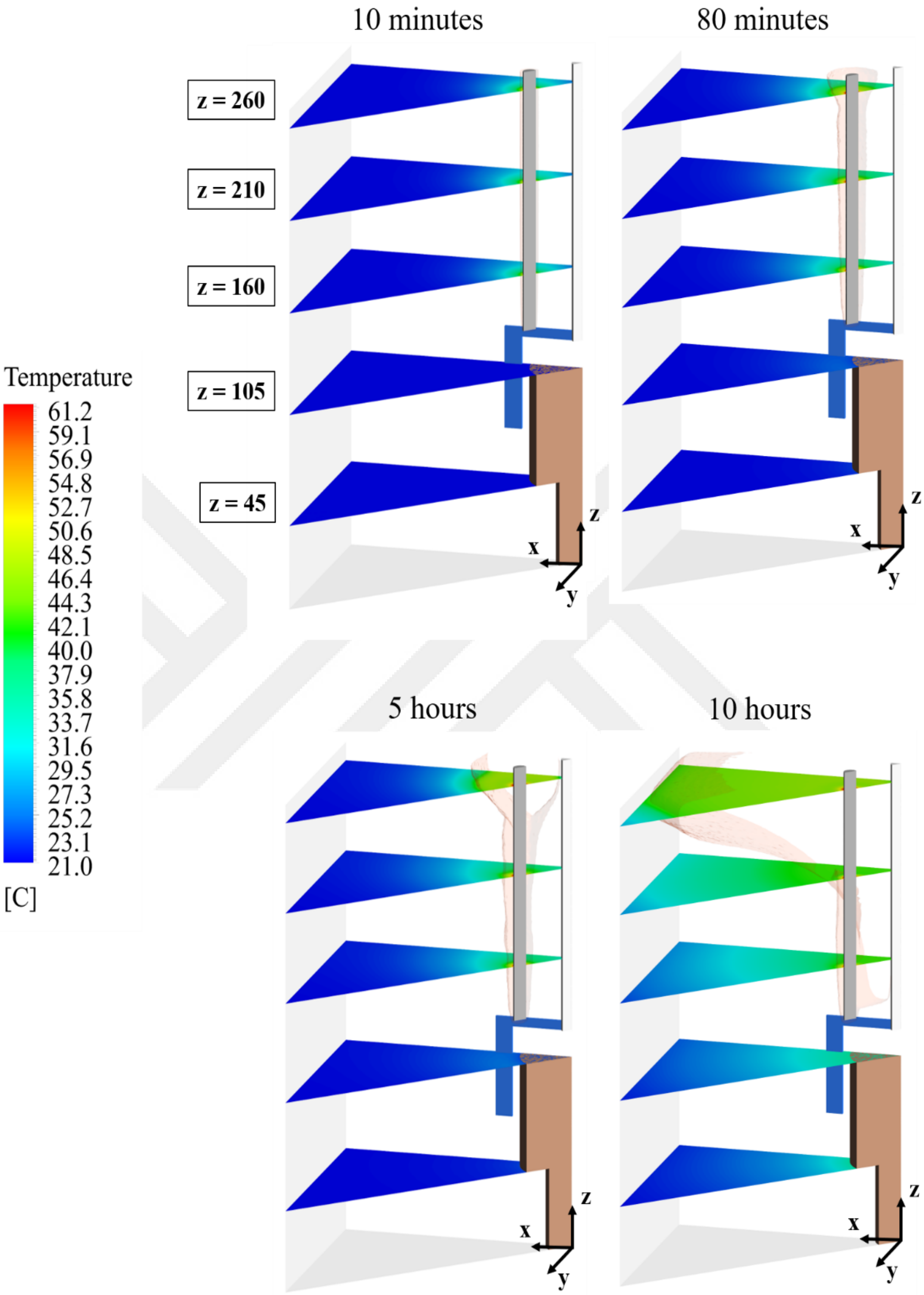

Figure 4.21 Temperature profiles for NR-20

An observation from Figure 4.21 is the significant delay in temperature rise. The slower temperature increase in simulations compared to experiments is mainly due to limitations in modeling transient thermal and convective behaviors. Numerical models often simplify natural convection by assuming laminar flow or using coarse spatial discretization, which underestimates internal fluid motion that accelerates heat transfer during melting. These factors lead to slower thermal responses and lower predicted peak temperatures. Additionally, lowering the heater's heat transfer rate results in about an $8°C$ reduction in peak temperature within the domain. As a result, even near the main heater, melting does not occur because the temperature remains below the PCM's melting point, preventing the use of the mixer in the NR-20 case. The setup analyzed involves constrained melting, where the solid PCM cannot fall under gravity to contact the heating surfaces. In contrast, unconstrained melting occurs when the solid PCM is free to fall, leading to the CCM phenomenon. Therefore, employing different modeling techniques becomes essential to accurately visualize such physical behavior while PCM melts in an unconstrained manner.

4.2.2 Validation of 2D Models & Compressibility Effect Investigation

4.2.2.1 Validation

The Boussinesq approximation is primarily utilized because it offers a significant computational benefit, making it a popular choice for researchers balancing efficiency and time. However, it is essential to acknowledge that certain limitations arise when employing the Boussinesq approximation. Specifically, the inability to capture the CCM effect results in mismatches between numerical predictions and experimental results.

The present study highlights that the CCM effect remains unrealized unless specific boundary conditions are explicitly defined and consistently applied. One of the boundary conditions that can lead to the observation of the CCM effect is when the wall temperature exceeds the temperature required to melt the PCM. In such a configuration, the CCM effect will be realized extensively, rendering the Boussinesq approximation an invalid method. On the other hand, without realizing the CCM effect, there is no stringent requirement or obligation to adopt the Boussinesq approximation in the numerical studies, thereby allowing for more flexibility in the choice of methodologies employed in similar circumstances. Herein, the differences that may arise while implementing the effect of compressibility are discussed. First, to validate the present numerical model that employs the Boussinesq approximation, a benchmark study is analyzed and rebuilt to ensure the reliability and repeatability of the built model [121].

As the VoF model is comparatively more complex, two benchmark studies are selected for validation. In the first benchmark study, a cylindrical cavity is considered, which is heated from vertical walls, insulated from the bottom, and has an opening to the atmosphere from above. A schematic of this study is illustrated in Figure 4.22.

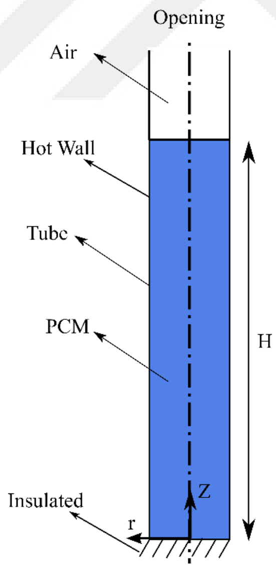

Figure 4.22 Adapted computational domain in Ref. [62]

The liquid PCM and the air are incompressible Newtonian fluids within the laminar regime. The relation for air density is $\rho = 1.2 \times 10^{-5} T^2 - 0.01134T + 3.4978$. VoF, along with the enthalpy porosity method, is used. The mentioned PCM in Table

4.2 is RT-27 from Rubitherm GmbH with a melting temperature range of 26°C to 28°C. The initial temperature of the whole system is maintained at 22°C.

Table 4.2 PCM properties in Ref. [62]

Phase	μ ($kg/(m.s)$)	$c_p(kJ/(kg.K))$	k ($W/(m.K)$)	ρ (kg/m^3)	L (kJ/kg)
Solid	−	2.5	0.24	870	179
Liquid	$-1.137439 \times 10^{-8}T^3 + 1.178188 \times 10^{-5}T^2 - 0.004111388T + 0.4857203$	2.5	0.15	879 @ 299 K 781.5 @ 301 K 750 @ 343 K	

The diameter of the cavity is 3 cm, and its height is 17 cm. The results are presented in Figure 4.23.

The evidence indicates that choosing a lower C_{mush} makes convection more dominant in the later stages of melting. In particular, after 4 minutes, the melt front starts to deviate from the reference study, and this trend worsens as time progresses. However, the general trends are remarkably similar to those in the experimental work of the benchmark study. Conversely, a higher C_{mush} leads to a longer melting time. This is due to the influence of the C_{mush} in the momentum equation, which suppresses natural convection until the end of the melting process.

A velocity vector is also demonstrated in Figure 4.23, clearly illustrating the flow direction at the onset of melting, where it flows upward adjacent to the hot wall and descends near the melt front, effectively ‘biting’ the solid PCM. The flow of liquid PCM is attributed to the density difference resulting from the temperature gradient within the liquid phase of the PCM.

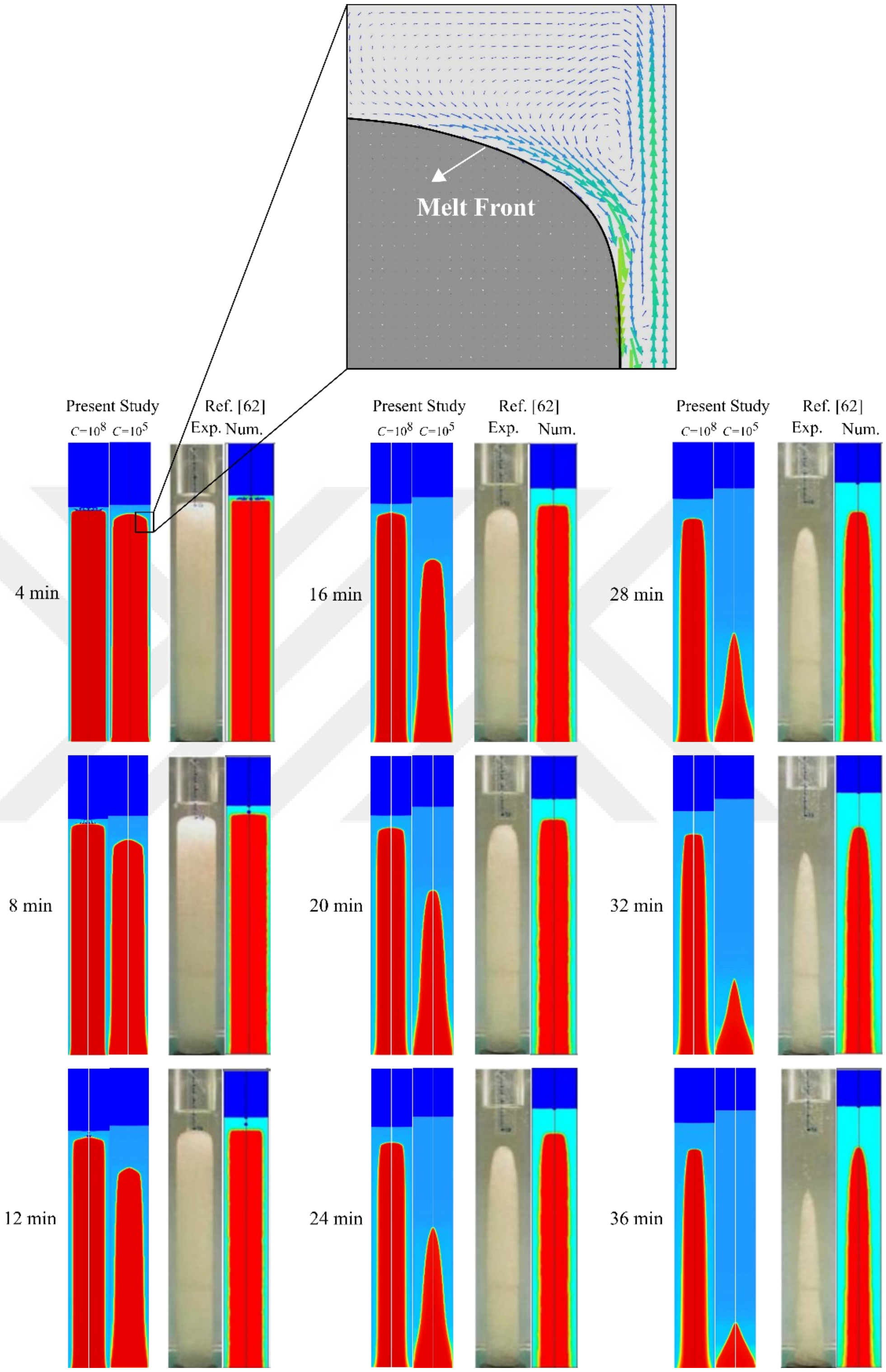

Figure 4.23 Comparison of present model with Ref. [62]

The second benchmark study examines a sphere filled with 85% PCM by volume. The rest of the sphere consists of air, with a density similar to that of the previous study. The computational domain is illustrated in Figure 4.24.

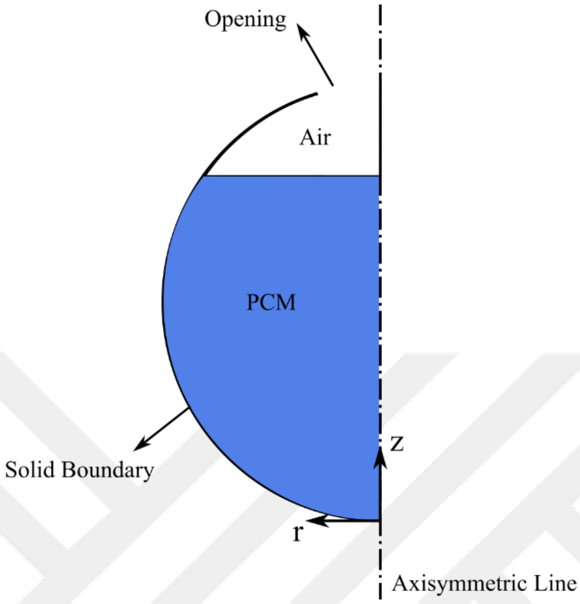

Figure 4.24 Adapted computational domain in Ref. [63]

The initial temperature of the system is kept at $23°C$, so the PCM is slightly sub-cooled. The PCM in Table 4.3 is RT-27 from Rubitherm GmbH, with a melting temperature range of $28°C$ to $30°C$. In this case, the thermal resistances due to the glass thickness are also considered with the thermal conductivity of 0.81 $W/(m.K)$ and thickness of 2 mm.

Table 4.3 PCM properties in Ref. [63]

Phase	μ $(kg/(m.s))$	$c_p(kJ/(kg.K))$	k $(W/(m.K))$	ρ (kg/m^3)	L (kJ/kg)
Solid	–	2.4	0.24	870	179
Liquid	3.42×10^{-3}	1.8	0.15	760	

For the current benchmark study, the computational domain of the sphere is reduced to a 2D axisymmetric form. 38510 cells are considered for the modeling process. The VoF method, in conjunction with the enthalpy porosity model, is used to capture the CCM phenomenon effectively. The detailed results of this evaluation are presented in Figure 4.25, which illustrates the key findings derived from the employed methodologies.

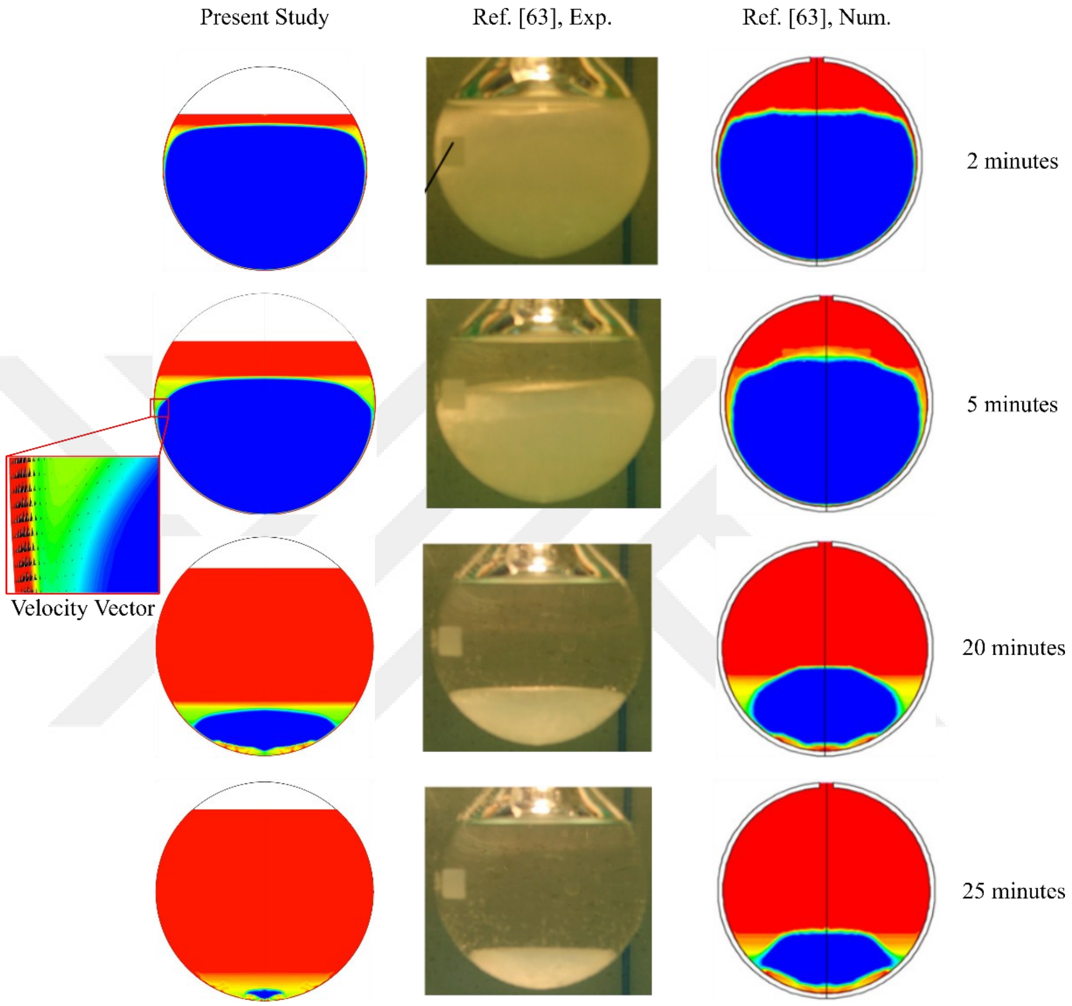

Figure 4.25 Comparison of present model with Ref. [63]

The melt front resembles the experimental work for up to 5 minutes. However, as the C_{mush} is very low, 2×10^4, its melting time is underestimated. In other words, it melted faster than it should have. The underlying reasons for the observed behavior and the necessity to select the lower C_{mush} are thoroughly examined in the sub-chapter dedicated to the simulations conducted using the VoF method. In addition, a detailed velocity vector has been included alongside Figure 4.25, providing further insights. Notably, the formation of the boundary layer adjacent to the hot wall and the characteristic descending flow pattern near the solid PCM are clearly depicted and analyzed in this context.

Experimental studies revealed the impact of CCM to be minimal with the current arrangement and boundary conditions. Therefore, to accurately depict this effect using the numerical study, some modifications are made to the numerical model. This phenomenon can be effectively traced and analyzed through the VoF modeling technique, which enables the introduction of the compressibility effect into the governing equations.

4.2.2.2 Compressibility Effect Investigation

First, the model with Plexiglass housing is comparatively studied and discussed. The configuration with plexiglass housing is considered as constrained melting in the field of research, where the solid PCM is not free to fall under the effect of gravity.

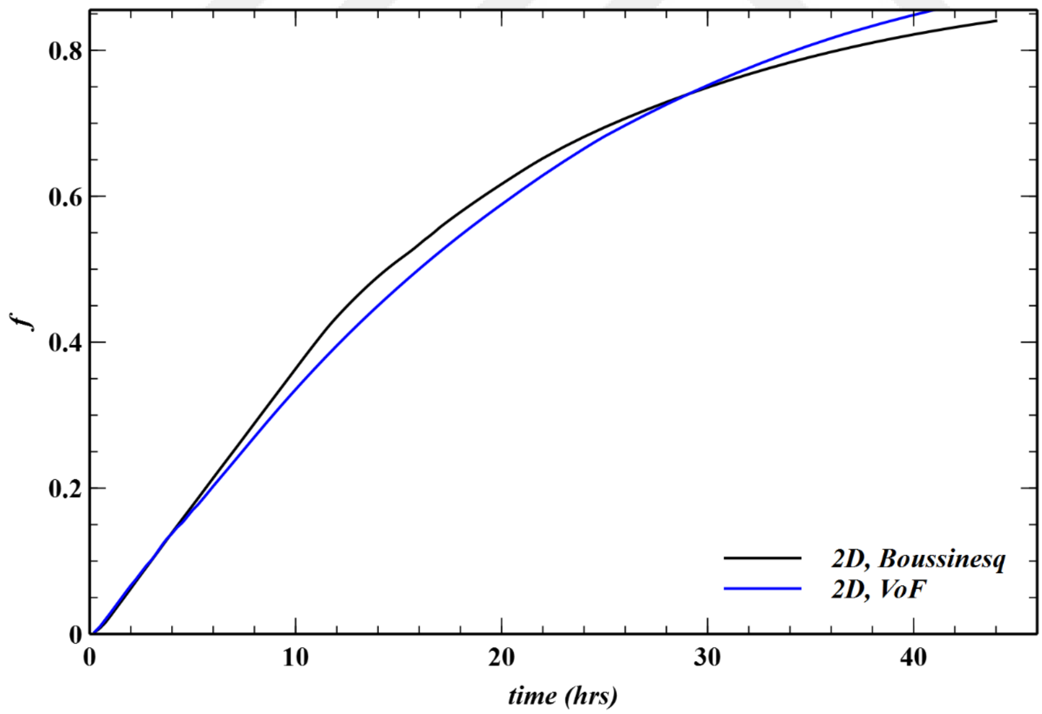

Figure 4.26 Effect of compressibility on liquid fraction evolution of PCM in Plexiglass housing

Figure 4.26 reveals that while both models demonstrate general agreement during the early and late melting stages, there is a notable deviation in the mid-stage, with the maximum error reaching about 8%. This difference arises from the distinct ways each method handles phase change dynamics and buoyancy-driven flow.

The VoF method, which explicitly monitors the solid–liquid interface, captures essential physical phenomena such as volumetric expansion, interface deformation, and localized flow in the vicinity of the melt front. This enables the model to represent the transition from conduction to convection accurately. Conversely, the Boussinesq approximation simplifies the process by assuming constant density (except within the buoyancy term) and does not explicitly resolve the melt front. Consequently, it neglects the thermal and momentum resistance at the phase boundary, allowing for more unrestricted movement of the flow. This results in an overestimation of the melting rate, especially during the convection-dominant mid-stage, despite underestimating localized convective structures. Notably, since the CCM is absent from this configuration, the influence of compressibility remains minimal and does not affect the overall melting behavior. Therefore, the Boussinesq approximation, which ignores compressibility, continues to perform adequately, although it omits certain details related to interfacial dynamics and localized flow transitions.

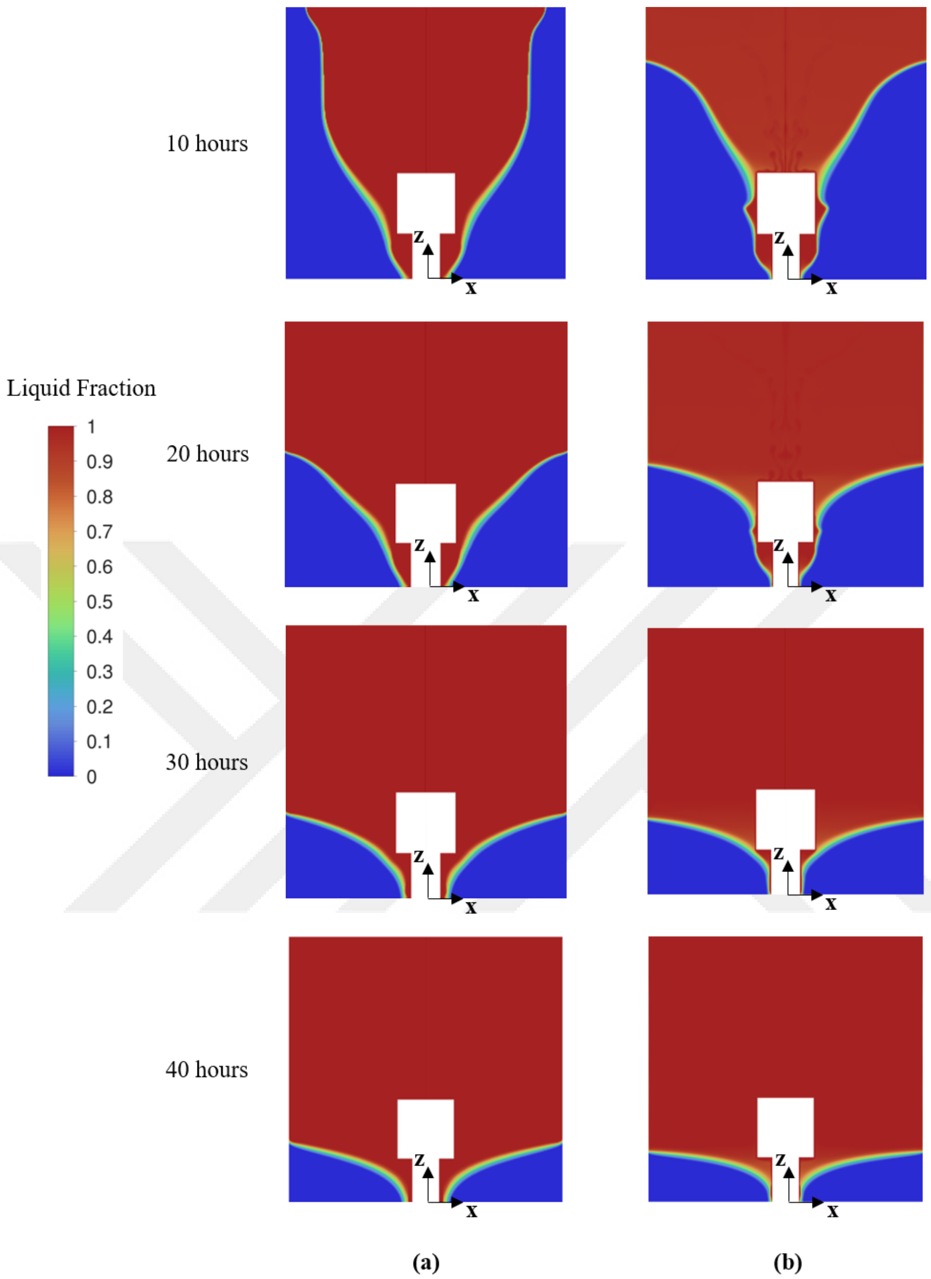

Figure 4.27 Effect of compressibility on melt front evolution of PCM in Plexiglass housing, **(a)** Boussinesq approximation and **(b)** VoF method

As presented in Figure 4.27, at 10 hours after the onset of the simulation, the solid PCM is wider and shorter when solved via the VoF method. Previously, to validate the experimental findings, the value of β, used in the Boussinesq approximation method, is reduced to 10^{-4} $1/K$, whereas, in the VoF method, density variations with temperature are considered. Reduction in β during the Boussinesq approximation lead to weak natural convection, therefore slower progression of the melt front.

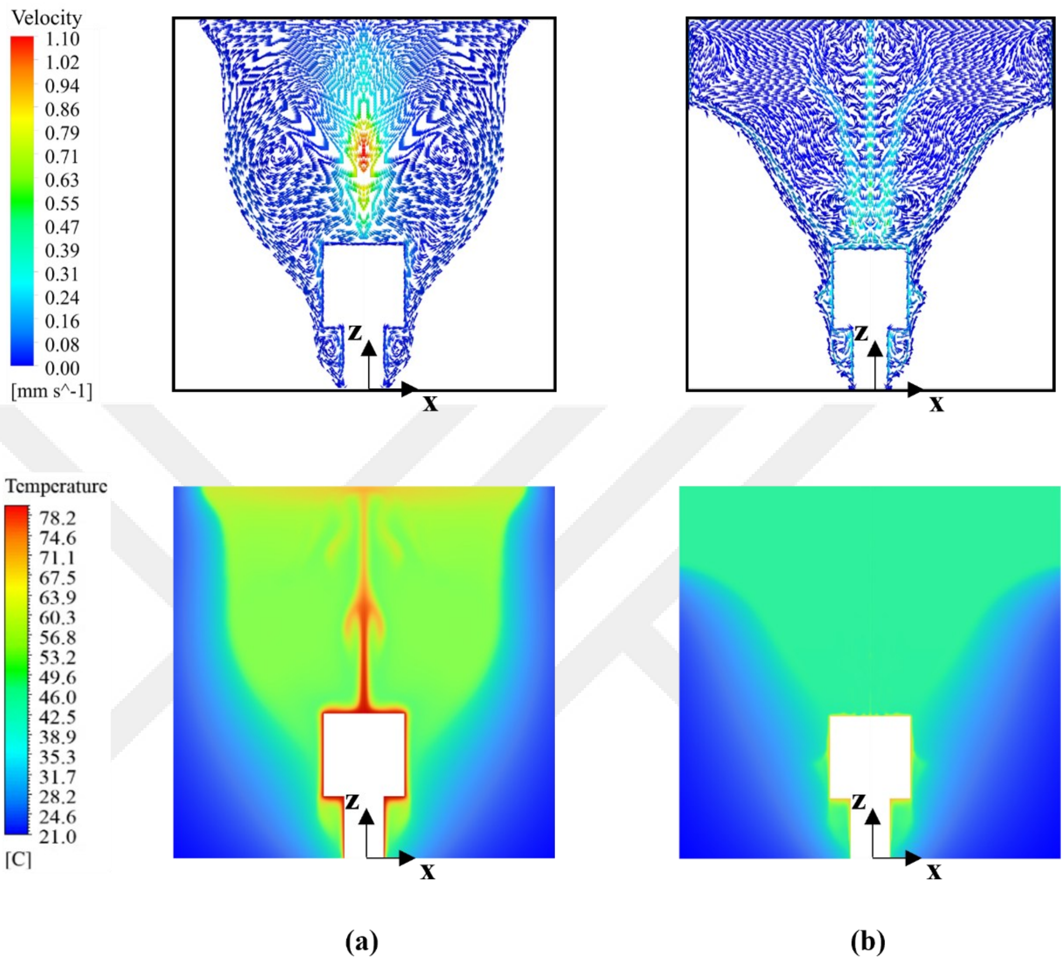

Figure 4.28 Effect of compressibility on velocity and temperature profiles of PCM in Plexiglass housing, **(a)** Boussinesq approximation and **(b)** VoF method

The velocity field reveals distinct differences between the Boussinesq and VoF formulations in modeling natural convection during PCM melting. In the Boussinesq model, velocity magnitudes are significantly higher, with peak values exceeding 1.1 mm/s, and the flow displays multiple, well-formed recirculation loops throughout the melted region. These loops occur because of how the approximation manages density changes with temperature across the entire fluid domain, enabling buoyant motion whenever thermal gradients exist, regardless of their proximity to the melt front.

The differences between these two analysis methods can also be visually observed by examining the relative temperature contours in the Figure 4.28, which presents the comparative study after 10 hours of melting onset. Although the same arrangement in terms of heat transfer rate is utilized in both models, considerable differences in the temperature contours are observed. When modeling with the Boussinesq approximation, the general temperature near the heater is approximately $20°C$ higher than in the same location when using the VoF method. This discrepancy also arises from the natural convection phenomenon and how each modeling method addresses it. Using the VoF method improves the spatial resolution of thermal gradients and captures dynamic interface-driven advection more effectively. As a result, natural convection is modeled more accurately. Consequently, sensible heat accumulation and peak temperature are reduced by spreading heat over a larger area. In the Boussinesq approximation model, the central thermal plume ascends owing to buoyancy and symmetry and subsequently disperses laterally near the top. As it cools, a portion of the flow recirculates downward along the central line, creating the narrow, downward-oriented branch.

The comparison between the two analysis methods demonstrates that, provided no CCM occurs within the domain, the differences in the predicted liquid fraction are negligible. Consequently, computational cost savings are achieved by employing the Boussinesq approximation. However, for capturing CCM, the VoF method offers a more realistic representation. To investigate the performance of the Boussinesq and VoF methods under CCM conditions, an additional model is developed with modified boundary conditions and cavity housing materials. To ensure the occurrence of CCM, the cavity walls are heated slightly above the melting temperature of the PCM, and stainless steel is selected as the housing material. The use of stainless steel promotes more uniform temperature distributions, thereby facilitating consistent melt front progression and enhancing the reliability of the comparative analysis. The liquid fraction evolution of the case study where CCM occurs is illustrated in Figure 4.29.

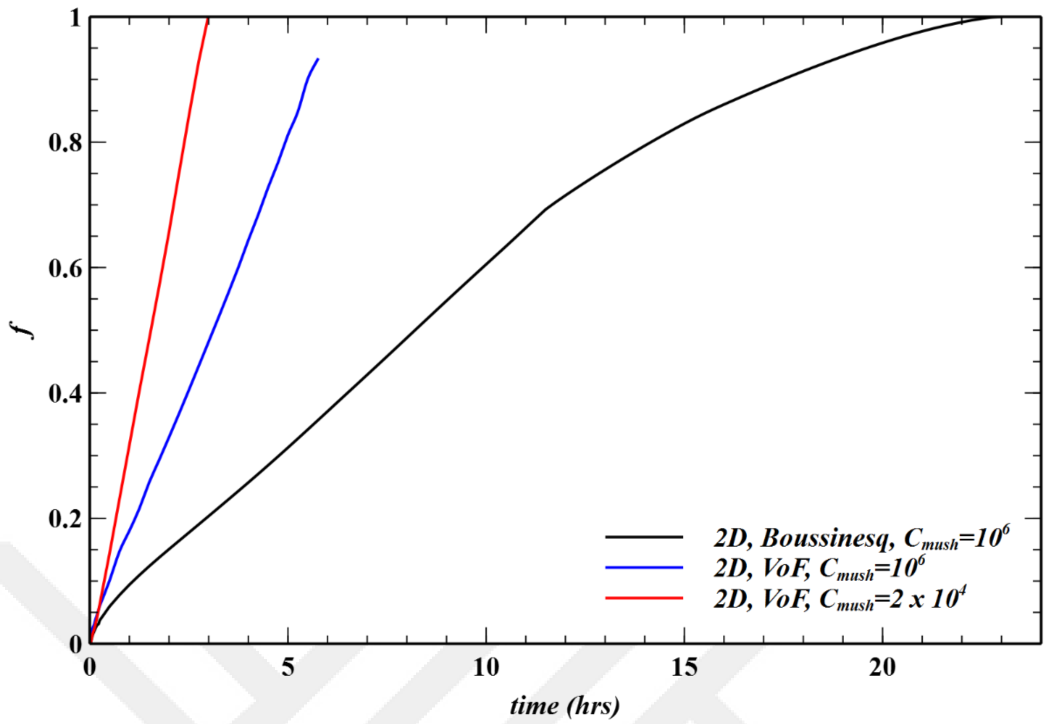

Figure 4.29 Effect of compressibility on liquid fraction evolution of PCM in stainless steel housing

There is a significant difference in the total melting time of the PCM when modeled using the VoF method, with a total melting time of approximately 3 hours compared to 23 hours for the same case when employing the Boussinesq approximation. This difference arises from the CCM phenomenon, which occurs when the boundary condition is sufficiently hot to melt the PCM immediately upon contact with the solid PCM.

It is important to note that the C_{mush} required to observe the CCM phenomenon is considered to be 2×10^4, however to have the same parameter of the C_{mush} of 10^6 as the Boussinesq approximation, another numerical study is carried out that results in slightly higher melting time, about 6 hours, compared to the lower C_{mush}.

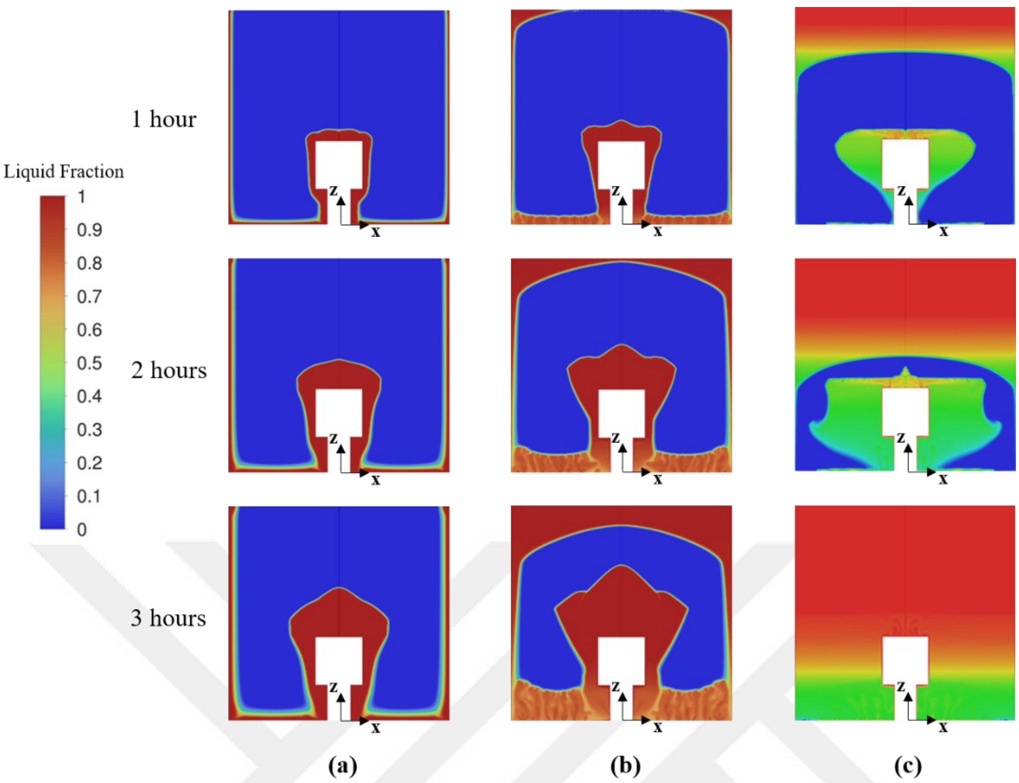

Figure 4.30 Effect of compressibility on melt front evolution of PCM in stainless steel housing, **(a)** Boussinesq approximation, **(b)** VoF method, and **(c)** VoF method with C_{mush} of 2×10^4

The implementation of the VoF method, particularly when the CCM effect is taken into account, results in a noticeable acceleration of the melting process, as evident in Figure 4.30. This acceleration effectively mirrors the behavior observed in real-world samples, providing a more realistic representation of melting phenomena as they occur in practical applications. Nevertheless, selecting a higher C_{mush} results in more intense damping of the solid phase PCM due to an increased source term in the momentum equation. The visualized outcomes indicate that unrealistic behavior occurs, whereby the solid PCM precipitates at comparatively lower speeds. The velocity contour of the side of the domain, where the CCM effect is clearly observable, is presented in Figure 4.31.

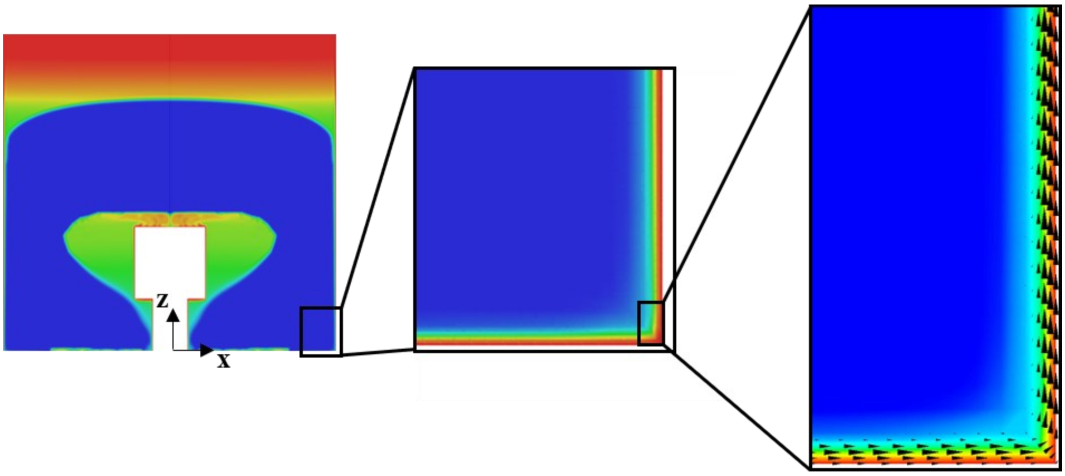

Figure 4.31 Effect of compressibility on the velocity profile of PCM in stainless steel housing

By considering the variation in density with temperature and confirming that the C_{mush} is low enough to prevent unrealistic damping of the solid PCM's motion, thin liquid film layers are observed to form between the solid PCM and the heated wall. This setup causes the liquid PCM to escape from the CCM region at relatively high velocities, reaching up to about 1 mm/s. As a result, the solid PCM stays largely in contact with the heated wall throughout the melting process.

CHAPTER 5

CONCLUSION AND FUTURE WORK

The present research provides a comprehensive investigation into how forced convection affects the transient melting behavior of a PCM contained within a cavity. By examining the melting dynamics under various conditions, the study has revealed important insights into the heat transfer processes governing PCM melting. In particular, the introduction of forced convective flow fundamentally alters the melting regime compared to pure conduction or natural convection scenarios. The analysis also considers the potential influence of fluid compressibility on simulation accuracy, recognizing that even small deviations from the incompressible assumption can introduce local density variations, alter flow patterns, and subsequently impact predicted heat transfer rates. Instead of providing a chapter-by-chapter summary, this conclusion consolidates the main findings and scientific contributions of the work, emphasizing how forced convection and compressibility affect melting dynamics and transient thermal responses, and then concludes with recommendations for future research.

An experimental setup is constructed to closely resemble a generic cavity filled with PCM and equipped with a mixer. The mixer plays a critical role by facilitating forced convection within the experimental domain, thereby enhancing heat transfer efficiency. To investigate the influence of forced convection on heat transfer processes, several experimental studies are conducted. These studies not only examine the effectiveness of forced convection but also provide a comparative analysis of the results with cases in which the mixer operates in still mode, under which conditions natural convection becomes the primary mechanism for heat transfer. In cases where the mixer is not rotating, both 2D and 3D numerical models are employed for analysis. The results demonstrate a reasonable agreement with the corresponding experimental findings and literature, indicating the robustness of the methodologies used in the current study and the validity of the results obtained.

Results indicate that incorporating the mixer reduced the melting time by up to 22%. An additional factor to be considered is the liquid fraction at steady state, which corresponds to the condition in which the system reaches equilibrium and no further variation in the liquid fraction occurs over time. For the NR-40 case, the liquid fraction at steady state is approximately 0.85. However, for both the R-25 and R-100 cases, the liquid fraction reaches 1 due to the influence of forced convective currents within the cavity. Even at the lowest rotational speed, R-5, although complete melting is not achieved, a slight improvement is observed, with the liquid fraction increasing by approximately 4% compared to the NR-40 case. The improvement in the melting is interpreted as a measure of how effectively the latent heat potential of the PCM is utilized, with the R-25 and R-100 cases representing scenarios in which the latent heat capacity is fully exploited.

Additionally, the effect of compressibility is studied, and it is concluded that the Boussinesq approximation remains valid as long as the CCM phenomenon is not realized. However, it is worth noting that the melt front would be modeled more realistically using the VoF method due to its more accurate representation of natural convection. Where the CCM phenomenon is evident, the VoF method should be employed, as solid PCM precipitation cannot be modeled otherwise, rendering the results highly unreliable. In the current configuration, the calculated melting time using the VoF method is approximately one-eighth that of the melting time estimated with the Boussinesq approximation. However, it is worth noting that the difference in melting rate stems from the emergence of the CCM, driven by the density difference between the solid and liquid phases of the PCM. To realize the effects of CCM in the simulations, C_{mush} needs to be modified, as at higher values of C_{mush}, the solid PCM motion is damped, and thus sinking of solid PCM is unrealistically slow.

The results of the current study have broader implications for both scientific and engineering fields. The observed decrease in melting time via forced convection indicates a promising route for developing more efficient latent heat storage systems. These can be applied in renewable energy integration, building climate control, and thermal management for electronic or industrial applications. Systems that require quick thermal charging and discharging would greatly benefit from mixer-assisted setups. Additionally, by systematically contrasting incompressible and compressible formulations, this research questions the common dependence on simplified assumptions in PCM studies. It promotes a more critical approach to understanding when these approximations are appropriate, thereby aiding the improvement of theoretical models for phase change heat transfer. Finally, combining experimental validation with advanced numerical methods creates a template for future research aiming to explore the complexity of PCM systems. In particular, the comparison of 2D/3D models, the Boussinesq approximation, and VoF simulations provides methodological benchmarks to choose the suitable modeling complexity based on specific problem needs.

Following the discussion of the principal outcomes of the present study, it is important to consider several key suggestions for future research. These recommendations aim to build upon the findings presented and explore new avenues that can contribute to a deeper understanding and advancement within the related area of study.

- <u>Experimental Study:</u> Incorporating CCM into the cavity requires specific cavity housing materials other than plexiglass, which would most likely be an opaque material. Future experiments should prioritize such visibility issues by employing advanced diagnostic methods, such as infrared thermography, fiber-optic sensing, or embedded thermal sensors, which should be integrated.
- <u>Numerical Study:</u> Modeling phase change and forced convection in PCM remains challenging due to current computational limitations. Newer

methods like cell-splitting and effective heat capacity are more accurate and efficient but less explored, especially in turbulent flows, moving solids or complex geometries. To improve predictive accuracy, future studies should develop turbulence models that better represent eddy structures and convective instabilities, which are frequently overlooked under laminar assumptions. C_{mush}, which is an important factor in modeling the PCM melting, is suggested to be studied adaptively for further studies. Also, a proposed research direction is to develop hybrid formulations that modify the enthalpy porosity method by incorporating additional momentum source terms, thereby enabling the simultaneous treatment of mushy zone damping and rigid body motion under external forces.

- <u>PCM thermophysical characteristics:</u> Experiments revealed discrepancies in PCM property literature. A comprehensive investigation is crucial, especially for key thermophysical properties like dynamic viscosity, liquid PCM thermal conductivity, and specific heat capacity.

In summary, the present study highlights the significant impact of forced convection on speeding up PCM melting and also points out the methodological sensitivities involved in simulating PCM melting. By integrating well-planned experiments with validated numerical models, it enhances understanding of PCM thermal behavior under forced convection and compressibility effects. More generally, it emphasizes the need to match physical assumptions with the actual mechanisms studied, helping to connect simplified models with practical applications.

Ultimately, this research's contributions go beyond just the immediate results, providing both conceptual understanding and methodological direction for future studies. By integrating experimental, numerical, and theoretical approaches, the study establishes a basis for developing next-generation latent heat storage systems that are both efficient and scientifically well-founded.

REFERENCES

[1] P. Raghavan, J. H. Ahn, and M. Shelke, "The role of 2D material families in energy harvesting: An editorial overview," *Journal of Materials Research*, vol. 37, no. 22, pp. 3857–3864, Nov. 2022.

[2] A. Laidoudi, S. Duchesne, F. Morganti, and G. Velu, "High-power density induction machines with increased windings temperature," *Open Physics*, vol. 18, no. 1, pp. 642–651, Jan. 2020.

[3] C. AJ, M. A. Salam, Q. M. Rahman, F. Wen, S. P. Ang, and W. Voon, "Causes of transformer failures and diagnostic methods – A review," *Renewable and Sustainable Energy Reviews*, vol. 82, pp. 1442–1456, Feb. 2018.

[4] M. I. Hasan, "Improving the cooling performance of electrical distribution transformer using transformer oil–based MEPCM suspension," *Engineering Science and Technology, an International Journal*, vol. 20, no. 2, pp. 502–510, Apr. 2017.

[5] M. I. Hasan and A. A. Abduladheem, "Modifying the thermal performance of electrical distribution transformers using phase change materials (paraffin wax)," *Heat Transfer - Asian Research*, vol. 48, no. 6, pp. 2440–2455, Sep. 2019.

[6] E. Buyukbicakci, I. Temiz, H. Edral, and Z. Buyukbicakci, "A new approach for transformer cooling systems: Application of phase change materials (PCM)," *Acta Physica Polonica A*, vol. 127, no. 4, pp. 1013–1015, Apr. 2015.

[7] Z. An, L. Jia, Y. Ding, C. Dang, and X. Li, "A review on lithium-ion power battery thermal management technologies and thermal safety," *Journal of Thermal Science*, vol. 26, no. 5, pp. 391–412, 2017.

[8] J. R. Patel and M. K. Rathod, “Recent developments in the passive and hybrid thermal management techniques of lithium-ion batteries,” *Journal of Power Sources*, vol. 480, p. 228820, 2020.

[9] P. Tirkey, R. K. Pandey, S. Kumar, and J. N. Mahto, “A detailed review on battery cooling systems for electric vehicles,” in *Proceedings of 2022 1st IEEE International Conference on Industrial Electronics: Developments and Applications, ICIDeA 2022*, Institute of Electrical and Electronics Engineers Inc., 2022, pp. 45–50.

[10] S. Fertahi, A. Samaouali, T. Bouhal, and A. Arid, “Thermal energy storage enhancement of a forced circulation solar water heater’s vertical tank unit using phase change material,” *Applied Thermal Engineering*, vol. 215, p. 118972, 2022.

[11] L. F. Cabeza, A. Castell, C. Barreneche, A. De Gracia, and A. I. Fernández, “Materials used as PCM in thermal energy storage in buildings: A review,” *Renewable and Sustainable Energy Reviews*, vol. 15, no. 3, pp. 1675–1695, 2011.

[12] P. Gadhave, F. Pathan, S. Kore, and C. Prabhune, “Comprehensive review of phase change material based latent heat thermal energy storage system,” *International Journal of Ambient Energy*, 2021.

[13] E. K. Gøtske, G. B. Andresen, and M. Victoria, “Cost and efficiency requirements for a successful electricity storage in a highly renewable European energy system,” *PRX Energy*, no. 2, p. 023006, May 2023.

[14] C. Luerssen, O. Gandhi, T. Reindl, K. W. D. Cheong, and C. Sekhar, “Levelised cost of thermal energy storage and battery storage to store solar PV energy for cooling purpose,” *Applied Energy*, pp. 1–10, Feb. 2019.

[15] M. Sun, T. Liu, H. Sha, M. Li, T. Liu, X. Wang, G. Chen, J. Wang, and D. Jiang, “A review on thermal energy storage with eutectic phase

change materials: Fundamentals and applications," *Journal of Energy Storage*, vol. 68, p. 107713, Sep. 2023.

[16] N. I. Ibrahim, F. A. Al-Sulaiman, S. Rahman, B. S. Yilbas, and A. Z. Sahin, "Heat transfer enhancement of phase change materials for thermal energy storage applications: A critical review," *Renewable and Sustainable Energy Reviews*, vol. 74, pp. 26–50, 2017.

[17] A. M. Abdulateef, S. Mat, J. Abdulateef, K. Sopian, and A. A. Al-Abidi, "Geometric and design parameters of fins employed for enhancing thermal energy storage systems: a review," *Renewable and Sustainable Energy Reviews*, vol. 82, pp. 1620–1635, 2018.

[18] K. K. Pillai and B. J. Brinkworth, "The storage of low grade thermal energy using phase change materials," *Applied Energy*, vol. 2, pp. 205–216, 1976.

[19] A. Abhat, "Low temperature latent heat thermal energy storage: heat storage materials," *Solar Energy*, vol. 10, no. 4, pp. 313–332, 1983.

[20] A. Sharma, V. V. Tyagi, C. R. Chen, and D. Buddhi, "Review on thermal energy storage with phase change materials and applications," *Renewable and Sustainable Energy Reviews*, vol. 13, no. 2, pp. 318–345, Feb. 2009.

[21] Y. Lin, G. Alva, and G. Fang, "Review on thermal performances and applications of thermal energy storage systems with inorganic phase change materials," *Energy*, vol. 165, pp. 685–708, Dec. 2018.

[22] D. Liu, K. Xie, H. Zhang, Y. Qiang, D. Yang, Z. Wang, L. Zhu, N. Akkurt, Y. Du, M. Shen, L. Zhong, F. Yu, and Q. Xu, "Numerical evaluation of convective heat transfer properties of two-dimensional rotating PCM melt in the unilaterally heated rectangular container," *Renewable Energy*, vol. 193, pp. 920–940, 2022.

[23] M. K. Rathod and J. Banerjee, "Thermal stability of phase change materials used in latent heat energy storage systems: A review," *Renewable and Sustainable Energy Reviews*, vol. 18, pp. 246–258, 2013.

[24] S. S. Magendran, F. S. Ahmed Khan, N.M. Mubarak, M. Vaka, R. Walvekar, M. Khalid, E.C. Abdullah, S. Nizamuddin, and R. R. Karri, "Synthesis of organic phase change materials (PCM) for energy storage applications: A review," *Nano-Structures and Nano-Objects*, vol. 20, Oct. 2019.

[25] S. S. Chandel and T. Agarwal, "Review of current state of research on energy storage, toxicity, health hazards and commercialization of phase changing materials," *Renewable and Sustainable Energy Reviews*, vol. 67, pp. 581–596, Jan. 2017.

[26] M. Ghorbani, H. Wang, and N. Roberts, "Analytical modeling of PCM in the melting process and numerical modeling of hybrid PCMs integrated with heat sink for wireless super-fast charging of EVs," *International Communications in Heat and Mass Transfer*, vol. 154, May 2024.

[27] H. K. Jalghaf and E. Kovács, "Simulation of phase change materials in building walls using effective heat capacity model by recent numerical methods," *Journal of Energy Storage*, vol. 83, p. 110669, Apr. 2024.

[28] G. K. Marri and C. Balaji, "Liquid crystal thermography based study on melting dynamics and the effect of mushy zone constant in numerical modeling of melting of a phase change material," *International Journal of Thermal Sciences*, vol. 171, p. 107176, Jan. 2022.

[29] M. M. Hasan and A. A. Luthfie, "Melting process investigation of KCl salt as a PCM by enthalpy-porosity simulation model with temperature-

dependent physical properties," *Journal of Power, Energy, and Control*, vol. 1, no. 2, pp. 58–67, Sep. 2024.

[30] V. Van Riet, T. Shockner, W. Beyne, G. Ziskind, M. De Paepe, and J. Degroote, "Limitations of the enthalpy-porosity method for numerical simulation of close-contact melting on inclined surfaces," *Journal of Physics: Conference Series*, vol. 2766, no. 1, p. 012214, May 2024.

[31] Z. Wang, H. Zhang, and X. Xia, "Experimental investigation on the thermal behavior of cylindrical battery with composite paraffin and fin structure," *International Journal of Heat and Mass Transfer*, vol. 109, pp. 958–970, 2017.

[32] X. Hu, H. Wu, X. Lu, S. Liu, and J. Qu, "Improving thermal conductivity of ethylene propylene diene monomer/paraffin/expanded graphite shape-stabilized phase change materials with great thermal management potential via green steam explosion," *Advanced Composites and Hybrid Materials*, vol. 4, no. 3, pp. 478–491, 2021.

[33] S. Motahar, N. Nikkam, A. A. Alemrajabi, R. Khodabandeh, M. S. Toprak, and M. Muhammed, "A novel phase change material containing mesoporous silica nanoparticles for thermal storage: A study on thermal conductivity and viscosity," *International Communications in Heat and Mass Transfer*, vol. 56, pp. 114–120, 2014.

[34] T. Zhou, Y. Zhao, and Z. Rao, "Fundamental and estimation of thermal contact resistance between polymer matrix composites: A review," *International Journal of Heat and Mass Transfer*, vol. 189, p. 122701, 2022.

[35] X. Gao, P. Wei, J. Yu, X. Huang, X. Yang, and B. Sundén, "Design and assessments on graded metal foam in heat storage tank: An

experimental and numerical study," *International Communications in Heat and Mass Transfer*, vol. 146, p. 106902, Jul. 2023.

[36] H. C. Tien and C. C. Wang, "Solidification of a liquid metal with natural convection in a thick-walled container," *The Chinese Journal of Mechanics*, vol. 15, no. 2, 1999.

[37] J. Tombrink and D. Bauer, "Simulation of a rotating drum heat exchanger for latent heat storage using a quasistationary analytical approach and a numerical transient finite difference scheme," *Applied Thermal Engineering*, vol. 194, Jul. 2021.

[38] J. Tombrink, H. Jockenhöfer, and D. Bauer, "Experimental investigation of a rotating drum heat exchanger for latent heat storage," *Applied Thermal Engineering*, vol. 183, Jan. 2021.

[39] J. Tombrink and D. Bauer, "Demand-based process steam from renewable energy: Implementation and sizing of a latent heat thermal energy storage system based on the Rotating Drum Heat Exchanger," *Applied Energy*, vol. 321, Sep. 2022.

[40] N. Maruoka, T. Tsutsumi, A. Ito, M. Hayasaka, and H. Nogami, "Heat release characteristics of a latent heat storage heat exchanger by scraping the solidified phase change material layer," *Energy*, vol. 205, Aug. 2020.

[41] A. Egea, A. García, R. Herrero-Martín, and J. Pérez-García, "Experimental performance of a novel scraped surface heat exchanger for latent energy storage for domestic hot water generation," *Renewable Energy*, vol. 193, pp. 870–878, Jun. 2022.

[42] S. Baghaei Oskouei, Z. R. Li, Ö. Bayer, and L. W. Fan, "Close-contact melting and natural convection in unconstrained melting: A parametric study," *International Journal of Heat and Mass Transfer*, vol. 218, p. 124795, Jan. 2024.

[43] M. Kirincic, A. Trp, and K. Lenic, “Influence of natural convection during melting and solidification of paraffin in a longitudinally finned shell-and-tube latent thermal energy storage on the applicability of developed numerical models,” *Renewable Energy*, vol. 179, pp. 1329–1344, Dec. 2021.

[44] T. S. Saitoh and A. Hoshi, “Experimental investigation on combined close-contact and natural convection melting in horizontal cylindrical and spherical capsules,” in *IECEC 96. Proceedings of the 31st Intersociety Energy Conversion Engineering Conference*, 1996.

[45] N. S. Dhaidan and J. M. Khodadadi, “Melting and convection of phase change materials in different shape containers: A review,” *Renewable and Sustainable Energy Reviews*, vol. 43, pp. 449–477, 2015.

[46] M. A. Hamdan and F. A. Elwerr, “Thermal energy storage using a phase change material,” *Solar Energy*, vol. 56, no. 2, pp. 183–189, 1996.

[47] Z.-X. Gong and A. S. Mujumdart, “Flow and heat transfer in convection-dominated melting in a rectangular cavity heated from below,” *International Journal of Heat and Mass Transfer*, vol. 41, no. 17, pp. 257–2580, 1998.

[48] D. Pal and Y. K. Joshi, “Melting in a side heated tall enclosure by a uniformly dissipating heat source,” *International Journal of Heat and Mass Transfer*, vol. 44, pp. 375–387, 2001.

[49] H. Shokouhmand and B. Kamkari, “Experimental investigation on melting heat transfer characteristics of lauric acid in a rectangular thermal storage unit,” *Experimental Thermal and Fluid Science*, vol. 50, pp. 201–212, 2013.

[50] B. Binet and M. Lacroix, “Numerical study of natural-convection-dominated melting inside uniformly and discretely heated rectangular

cavities," *Numerical Heat Transfer; Part A: Applications*, vol. 33, no. 2, pp. 207–224, 1998.

[51] S. Huang, J. Lu, Y. Li, L. Xie, L. Yang, Y. Cheng, S. Chen, L. Zeng, W. Li, Y. Zhang, and L. Wang, "Experimental study on the influence of PCM container height on heat transfer characteristics under constant heat flux condition," *Applied Thermal Engineering*, vol. 172, p. 115159, Mar. 2020.

[52] F. A. Hamad, E. Egelle, S. Gooneratne, and P. Russell, "The effect of aspect ratio on PCM melting behaviour in rectangular enclosure," *International Journal of Sustainable Engineering*, vol. 14, no. 5, pp. 1251–1268, 2021.

[53] A. Gadgil and D. Gobin, "Analysis of two-dimensional melting in rectangular enclosures in presence of convection," *Journal of Heat Transfer*, vol. 106, no. 1, pp. 20–26, 1984.

[54] C. Benard, D. Gobin, and F. Martinez, "Melting in rectangular enclosures: Experiments and numerical simulations," *Journal of Heat Transfer*, vol. 107, no. 4, pp. 794–803, 1985.

[55] M. A. Hamdan and I. Al-Hinti, "Analysis of heat transfer during the melting of a phase-change material," *Applied Thermal Engineering*, vol. 24, no. 13, pp. 1935–1944, Sep. 2004.

[56] T. J. Scanlon and M. T. Stickland, "A numerical analysis of buoyancy-driven melting and freezing," *International Journal of Heat and Mass Transfer*, vol. 47, no. 3, pp. 429–436, 2004.

[57] P. Lamberg, R. Lehtiniemi, and A. M. Henell, "Numerical and experimental investigation of melting and freezing processes in phase change material storage," *International Journal of Thermal Sciences*, vol. 43, no. 3, pp. 277–287, Mar. 2004.

[58] M. Fadl and P. Eames, “A numerical investigation into the heat transfer and melting process of lauric acid in a rectangular enclosure with three values of wall heat flux,” in *Energy Procedia*, Elsevier Ltd, 2019, pp. 4502–4509.

[59] M. K. Moallemi, B. W. Webb, and R. Viskanta, “An experimental and analytical study of close-contact melting,” *Journal of Heat Transfer*, vol. 108, no. 4, pp. 894–899, 1986.

[60] Y. Hu and M. Shi, “Close-contact melting around a hot sphere,” *Journal of Thermal Science*, vol. 6, no. 1, Nov. 1996.

[61] A. F. Regin, S. C. Solanki, J. S. Saini, and S. Francisco, “Experimental and numerical analysis of melting of PCM inside a spherical capsule,” in *9th AIAA/ASME Joint Thermophysics and Heat Transfer Conference*, 2006.

[62] H. Shmueli, G. Ziskind, and R. Letan, “Melting in a vertical cylindrical tube: Numerical investigation and comparison with experiments,” *International Journal of Heat and Mass Transfer*, vol. 53, no. 19–20, pp. 4082–4091, Sep. 2010.

[63] E. Assis, L. Katsman, G. Ziskind, and R. Letan, “Numerical and experimental study of melting in a spherical shell,” *International Journal of Heat and Mass Transfer*, vol. 50, no. 9–10, pp. 1790–1804, May 2007.

[64] F. L. Tan, “Constrained and unconstrained melting inside a sphere,” *International Communications in Heat and Mass Transfer*, vol. 35, no. 4, pp. 466–475, Apr. 2008.

[65] A. R. Archibold, J. Gonzalez-Aguilar, M. M. Rahman, D. Yogi Goswami, M. Romero, and E. K. Stefanakos, “The melting process of storage materials with relatively high phase change temperatures in

partially filled spherical shells," *Applied Energy*, vol. 116, pp. 243–252, Mar. 2014.

[66] N. Sharifi, C. W. Robak, T. L. Bergman, and A. Faghri, "Three-dimensional PCM melting in a vertical cylindrical enclosure including the effects of tilting," *International Journal of Heat and Mass Transfer*, vol. 65, pp. 798–806, 2013.

[67] L. W. Fan, Z. Q. Zhu, Y. Zeng, Q. Ding, and M. J. Liu, "Unconstrained melting heat transfer in a spherical container revisited in the presence of nano-enhanced phase change materials (NePCM)," *International Journal of Heat and Mass Transfer*, vol. 95, pp. 1057–1069, Apr. 2016.

[68] F. E. Moore and Y. Bayazitoglu, "Melting within a spherical enclosure," *Journal of Heat Transfer*, vol. 104, pp. 19–23, Feb. 1982.

[69] A.G. Tkachev, "Heat exchange in melting and freezing of ice in problem of heat transfer during change of phase," *A collection of Articles AEC-te-3405, translated from Russian, State Power Press*, pp. 169–178, 1953.

[70] A. Chaboki and E. M. Sparrow, "Melting in a vertical tube rotating about a vertical, colinear axis," *International Journal of Heat and Mass Transfer*, vol. 30, no. 4, pp. 613–622, 1987.

[71] G. T. Geiger and E. M. Sparrow, "Effect of rotation on melting in a horizontal tube rotating about a vertical axis," *International Journal of Heat and Mass Transfer*, vol. 30, no. 8, pp. 1567–1575, 1987.

[72] A. Jaberi Khosroshahi and S. Hossainpour, "Investigation of storage rotation effect on phase change material charging process in latent heat thermal energy storage system," *Journal of Energy Storage*, vol. 36, p. 102442, Apr. 2021.

[73] R. Hassanzadeh, R. Rahimi, A. Khosravipour, S. Mostafavi, and H. Pekel, “Analysis of natural convection in a square cavity in the presence of a rotating cylinder with a specific number of roughness components,” *International Communications in Heat and Mass Transfer*, vol. 116, p. 104708, Jul. 2020.

[74] C. Yang, Z. J. Zheng, X. Cai, and Y. Xu, “Experimental study on the effect of rotation on melting performance of shell-and-tube latent heat thermal energy storage unit,” *Applied Thermal Engineering*, vol. 215, p. 118877, Jun. 2022.

[75] Y. Zhang, S. Liu, L. Yang, X. Yang, Y. Shen, and X. Han, “Experimental study on the strengthen heat transfer performance of PCM by active stirring,” *Energies*, vol. 13, no. 9, May 2020.

[76] F. Selimefendigil and H. F. Öztop, “Mixed convection in a PCM filled cavity under the influence of a rotating cylinder,” *Solar Energy*, vol. 200, pp. 61–75, Apr. 2020.

[77] M. I. Fathi and M. A. Mussa, “The effect of whole system rotation on the thermal performance of a phase change energy storage,” *Journal of Energy Storage*, vol. 68, p. 107732, Sep. 2023.

[78] L. Kolsi, F. Selimefendigil, and M. Omri, “Effects of surface rotation on the phase change process in a 3D complex-shaped cylindrical cavity with ventilation ports and installed PCM packed bed system during hybrid nanofluid convection,” *Mathematics*, vol. 9, no. 20, Oct. 2021.

[79] W. Li, J. Wang, X. Zhang, X. Liu, and H. Dong, “Experimental and numerical investigation of the melting process and heat transfer characteristics of multiple phase change materials,” *International Journal of Energy Research*, vol. 44, no. 14, pp. 11219–11232, Nov. 2020.

[80] M. Fadl and P. C. Eames, “An experimental investigations of the melting of RT44HC inside a horizontal rectangular test cell subject to uniform wall heat flux,” *International Journal of Heat and Mass Transfer*, vol. 140, pp. 731–742, Sep. 2019.

[81] M. Akgün, O. Aydin, and K. Kaygusuz, “Experimental study on melting/solidification characteristics of a paraffin as PCM,” *Energy Conversion and Management*, vol. 48, no. 2, pp. 669–678, Feb. 2007.

[82] M. Rathod and S. Vallabhbhai, “Numerical investigation on latent heat storage unit of different configurations,” *International Journal of Mechanical and Mechatronics Engineering*, vol. 5, no. 3, pp. 652–657, 2011.

[83] C. Ding, J. Pei, S. Wang, and Y. Wang, “Evaluation and comparison of thermal performance of latent heat storage units with shell-and-tube, rectangular, and cylindrical configurations,” *Applied Thermal Engineering*, vol. 218, p. 119364, Jan. 2023.

[84] B. Zivkovic and I. Fujii, “An analysis of isothermal phase change of phase change material within rectangular and cylindrical containers,” *Solar Energy*, vol. 70, no. 1, pp. 51–61, 2001.

[85] N. R. Vyshak and G. Jilani, “Numerical analysis of latent heat thermal energy storage system,” *Energy Conversion and Management*, vol. 48, no. 7, pp. 2161–2168, Jul. 2007.

[86] Z. Meftah and K. Razzaghi, “Enhancing heat transfer in a single-phase laminar forced convection flow using low-pressure drop motionless mixers,” Jan. 2024.

[87] S. Ali, S. Menanteau, C. Habchi, T. Lemenand, and J. L. Harion, “Heat transfer and mixing enhancement by using multiple freely oscillating flexible vortex generators,” *Applied Thermal Engineering*, vol. 105, pp. 276–289, Jul. 2016.

[88] M. Zlokarnik, *Stirring : theory and practice*, 1st ed. Weinheim, Germany: Wiley-VCH, 2001.

[89] Z. Qin, C. Ji, Z. Low, S. Dubey, F. Hoong Choo, and F. Duan, "Effect of fin location on the latent heat storage: A numerical study," in *Energy Procedia*, Elsevier Ltd, 2017, pp. 320–326.

[90] M. Ghamari, C. H. See, D. Hughes, T. Mallick, K. S. Reddy, K. Patchigolla, and S. Sundaram, "Advancing sustainable building through passive cooling with phase change materials, a comprehensive literature review," *Energy and Buildings*, vol. 312, p. 114164, Jun. 2024.

[91] W. Phukaokaew, A. Suksri, and T. Wongwuttanasatian, "The modification of thermal conductivity of phase change material using nano metal-oxide particles," *Materials Science Forum*, vol. 1113, pp. 69–74, Feb. 2024.

[92] D. Martheleur and D. Groulx, "Thermal management of high-powered short-duration electronics aided by a phase change material thermal energy storage," *Journal of Physics: Conference Series*, vol. 2766, no. 1, p. 012213, May 2024.

[93] B. Prabhu, A. Valan Arasu, S. Nižetić, and M. Arıcı, "An experimental investigation on thermal energy storage characteristics of nanocomposite particles dispersed phase change material for solar photovoltaic module cooling," *Journal of Energy Storage*, vol. 73, p. 109221, Dec. 2023.

[94] A. R. Bais, D. G. Subhedar, and S. Panchal, "Critical thickness of nano-enhanced RT-42 paraffin based battery thermal management system for electric vehicles: A numerical study," *Journal of Energy Storage*, vol. 52, p. 104757, Aug. 2022.

[95] A. R. Bais, D. G. Subhedhar, N. C. Joshi, and S. Panchal, “Numerical investigation on thermal management system for lithium ion battery using phase change material,” *Materials Today: Proceedings*, vol. 66, pp. 1726–1733, 2022.

[96] S. Loem, T. Deethayat, A. Asanakham, and T. Kiatsiriroat, “Thermal characteristics on melting/solidification of low temperature PCM balls packed bed with air charging/discharging,” *Case Studies in Thermal Engineering*, vol. 14, Sep. 2019.

[97] T. Sathe and A. S. Dhoble, “Thermal analysis of an inclined heat sink with finned PCM container for solar applications,” *International Journal of Heat and Mass Transfer*, vol. 144, Dec. 2019.

[98] Rubitherm GmbH, “Technical data sheet: RT-42.,” https://www.rubitherm.eu/en/productcategory/organische-pcm-rt, [Accessed: August, 2025].

[99] F. R. Martínez, E. Borri, S. Mani Kala, S. Ushak, and L. F. Cabeza, “Phase change materials for thermal energy storage in industrial applications,” *Heliyon*, vol. 11, no. 1, p. e41025, Jan. 2025.

[100] J. V. Christy, A. Balwani, H. Mehling, and N. Agrawal, “Optimization of DSC measurements for organic phase change materials,” *Journal of Energy Storage*, vol. 73, Dec. 2023.

[101] T. C. Ong, E. Graham, G. Will, and T. A. Steinberg, “High-temperature phase change material (PCM) selection for concentrating solar power tower applications,” *Advanced Sustainable Systems*, vol. 3, no. 2, Feb. 2019.

[102] S. R. L. da Cunha and J. L. B. de Aguiar, “Phase change materials and energy efficiency of buildings: A review of knowledge,” *Journal of Energy Storage*, vol. 27, p. 101083, Feb. 2020.

[103] M. J. Richardson, "Quantitative aspects of differential scanning calorimetry," *Thermochimica Acta*, vol. 300, pp. 15–28, 1997.

[104] E. Günther, S. Hiebler, H. Mehling, and R. Redlich, "Enthalpy of phase change materials as a function of temperature: Required accuracy and suitable measurement methods," *International Journal of Thermophysics*, vol. 30, no. 4, pp. 1257–1269, Aug. 2009.

[105] "Guide for Use of the Petroleum Measurement Tables ASTM D1250-08," Oct. 01, 2013, *ASTM International, West Conshohocken, PA*.

[106] W. A. Dukhan, N. S. Dhaidan, and T. A. Al-Hattab, "Experimental investigation of the horizontal double pipe heat exchanger utilized phase change material," in *IOP Conference Series: Materials Science and Engineering*, Institute of Physics Publishing, Jan. 2020.

[107] J. Kirchner, "Data analysis toolkit #5: Uncertainty analysis and error propagation," University of California, Berkeley, Department of Earth and Planetary Science, 1995.

[108] M. Talebzadegan, M. Moravej, E. Assareh, and M. Izadi, "Melting performance enhancement of ferro-hydrodynamic carreau non-Newtonian PCM in porous media: A geometrical evaluation," *Thermal Science*, vol. 27, no. 2B, pp. 1355–1366, 2023.

[109] A. Boroojerdian, H. Nemati, and E. Selahi, "Direct and non-contact measurement of liquid fraction in unconstrained encapsulated PCM melting," *Energy*, vol. 284, p. 129359, Dec. 2023.

[110] Y. Kim, A. Hossain, and Y. Nakamura, "Numerical study of melting of a phase change material (PCM) enhanced by deformation of a liquid–gas interface," *International Journal of Heat and Mass Transfer*, vol. 63, pp. 101–112, Aug. 2013.

[111] M. Bucci, J. Gratien, T. Faney, T. Nakano, and G. Charpiat, “Using graph neural network for gas-liquid interface reconstruction in volume of fluid methods,” in *8th European Congress on Computational Methods in Applied Sciences and Engineering*, CIMNE, 2022.

[112] S. Arena, G. Cau, and C. Palomba, “CFD simulation of melting and solidification of PCM in thermal energy storage systems of different geometry,” *Journal of Physics: Conference Series*, vol. 655, p. 012051, Nov. 2015.

[113] V. Shatikian, V. Dubovsky, G. Ziskind, and R. Letan, “Simulation of PCM melting and solidification in a partitioned storage unit,” in *Heat Transfer: Volume 2*, ASMEDC, Jan. 2003, pp. 347–353.

[114] H. Behi, M. Ghanbarpour, and M. Behi, “Investigation of PCM-assisted heat pipe for electronic cooling,” *Applied Thermal Engineering*, vol. 127, pp. 1132–1142, 2017.

[115] V. R. Voller and C. Prakash, “A fixed grid numerical modelling methodology for convection diffusion mushy region phase change problems,” *International Journal of Heat Mass Transfer*, vol. 30, no. 8, pp. 1709–1719, 1987.

[116] A. Memon and A. K. Gupta, “Effects of aspect ratio and mushy-zone parameter on melting performance of a thermal energy storage unit filled with phase change material,” *International Journal of Chemical Reactor Engineering*, vol. 19, no. 8, pp. 817–827, 2021.

[117] V. R. Voller, N. C. Markatos, and M. Cross, “An enthalpy method for convection/diffusion phase change,” *International Journal for Numerical Methods in Engineering*, vol. 24, pp. 271–284, Jan. 1987.

[118] A. D. Brent, V. R. Voller, and K. J. Reid, “Enthalpy-porosity technique for modeling convection-diffusion phase change: Application to the

melting of a pure metal," *Numerical Heat Transfer*, vol. 13, no. 3, pp. 297–318, Apr. 1988.

[119] J. M. Khodadadi and Y. Zhang, "Effects of buoyancy-driven convection on melting within spherical containers," *International Journal of Heat and Mass Transfer*, vol. 44, no. 8, pp. 1605–1618, Apr. 2001.

[120] N. S. Dhaidan, J. M. Khodadadi, T. A. Al-Hattab, and S. M. Al-Mashat, "Experimental and numerical investigation of melting of phase change material/nanoparticle suspensions in a square container subjected to a constant heat flux," *International Journal of Heat and Mass Transfer*, vol. 66, pp. 672–683, 2013.

[121] S. Baghaei Oskouei and Ö. Bayer, "Experimental and numerical investigation of melting and solidification enhancement using Fibonacci-inspired fins in a latent thermal energy storage unit," *International Journal of Heat and Mass Transfer*, vol. 210, p. 124180, Aug. 2023.

APPENDICES

A. Construction Process of the Experimental Setup

Considering the initial dimensions of the Plexiglas sheet, which is measured 980 × 980 mm^2, it is first segmented into the required pieces with a tolerance of 5 mm on each side. Following the segmentation of the Plexiglas sheets, they are forwarded to the CNC machine for subsequent precise processing, as illustrated in Figure A.1.

Figure A.1 CNC machine operation

After completing the assembly of the six walls and four flanges of the cavity, it is secured using bar clamps, as illustrated in Figure A.2.

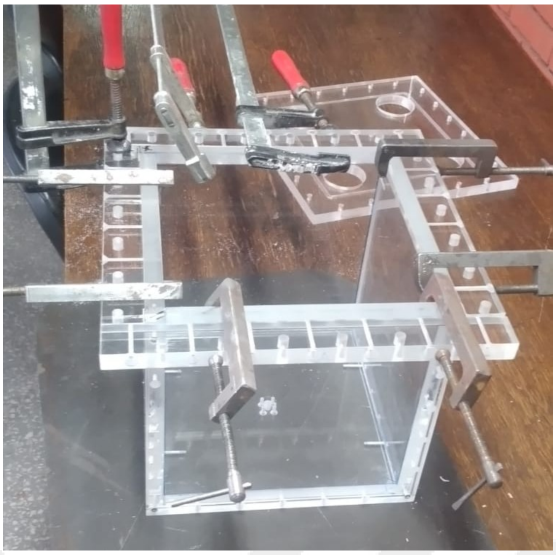

Figure A.2 Fixing the cavity with some bar clamps

Additionally, it is worth noting that to overcome the difficulties that may arise while building up the cavity, some threaded holes are incorporated into the cavity walls due to the non-uniformity in thickness of the sheets. Some of them are realized in Figure A.2.

Meanwhile, the copper heater housing, mixer, and shaft are prepared, which would be installed in the final version of the experimental setup. Dichloromethane is supplied to ensure the cavity's sealing ability. However, precautions are taken due to its highly toxic nature. Before using Dichloromethane, the joint areas of the walls are sanded with sandpaper to reduce the connection area and create “micro gaps." Dichloromethane is then injected into the gaps using a syringe, as depicted in Figure A.3.

Figure A.3 Sealing the cavity

However, after leakage testing, it is observed that the sealing is not perfect, so Chloroform is also applied to the cavity gaps, resulting in a complete seal. The copper heater housing is also bolted to the bottom wall with four bolts, and some water-resistant glue is injected into the joint spaces of the housing, which might cause the liquid PCM to leak. Its finalized revision is demonstrated in Figure A.4.

Figure A.4 Copper heater housing placement

B. Control Mechanism of the Experimentation

An electronic control unit is designed and built to address the needs of the current study. 4 TCs are considered the main inputs to the electronic control unit. The main motivations and working principles of the electronic control unit are summarized and outlined as follows:

- Feed the electrical heat source with the prescribed voltage and current amounts.
- Finding out the right time to start the rotation of the mixer. Two TCs (No. 14 and 17) will be monitored, and the signal for the rotation process will be sent once the lower temperature of these two TCs reaches the specified temperature. Three rotation speeds (5, 25, and 100 rpm) are anticipated.
- As TC No. 7, which is mounted on the heater housing, reaches 65ºC, the input power for the mixer and heaters will be immediately turned off.
- A TC (No. 4) will be placed at the internal corners of the cavity (in the lowest possible position). After reaching a temperature of $43°C$, the blade will stop rotating, and the heat source will be turned off. The experiment will be concluded.
- Utilizing the energy analyzer to analyze the energy input for the heaters and the mixer. These analyses would be crucially important while conducting the calculations that satisfies the first law of Thermodynamics.

The schematic illustrating the working principle of the electronic control unit is displayed in Figure B.1.

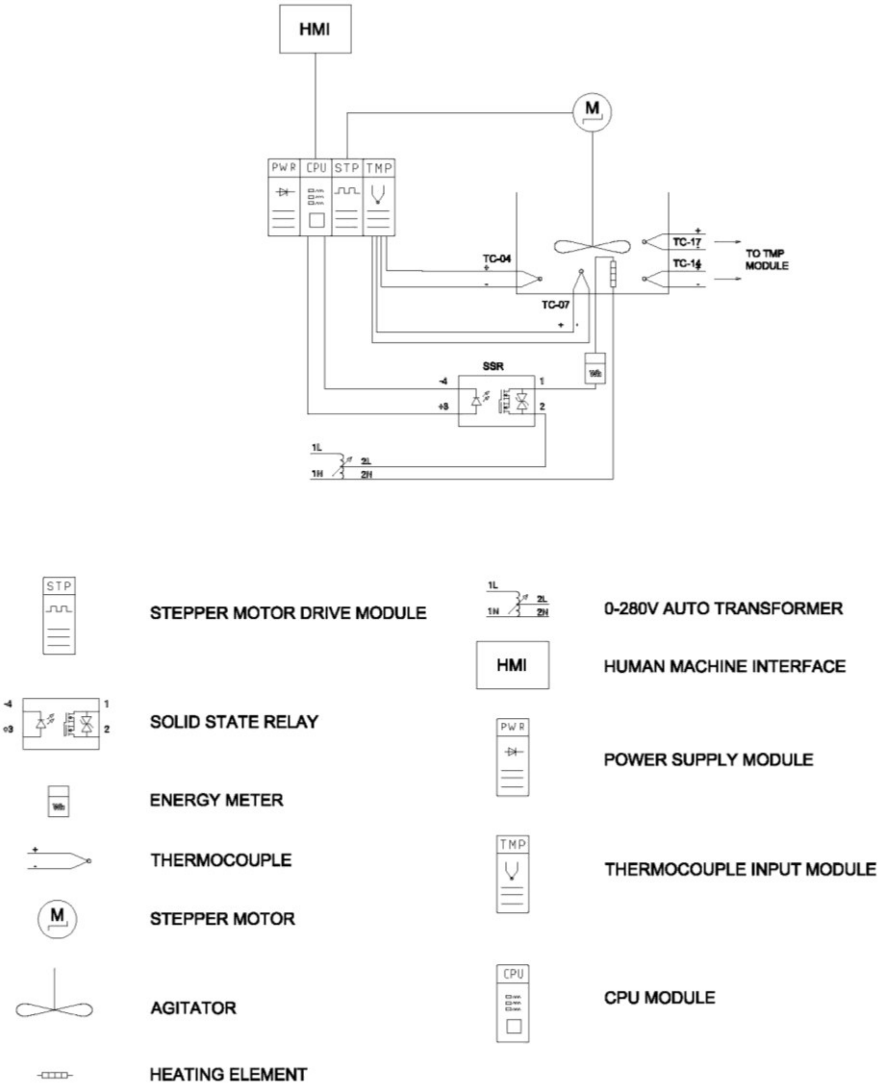

Figure B.1 Working principle of the electronic control unit

The readings from four TCs are directed to the thermocouple input module (TMP). According to the guidelines set forth by the HMI, tasks related to the stepper motor and heating element are assigned through the stepper motor driver module (STP) and central processing unit (CPU), respectively. The specifications of the components used in the electronic control unit are listed in Table B.1.

Table B.1 Specification of the electronic control unit sub-items

No.	Brand	Description	Model No.
1	Siemens	Cpu Module	6ES7 214-1AG40-0XB0
2	Siemens	Analog Input 4xtc Module	6ES7 231-5QD32-0XB0
3	Siemens	24Vdc 2.5A Power Supply	6EP1332-2BA20
4	Kinco	4.3" HMI	GL043E
5	Kinco	Stepper Motor Drive	-
6	Klemsan	Energy Analyzer	-
7	Enda	SSR Relay	EPDA1-240Z
8	Eaton	2A MCB	2A SP MCB
9	Eaton	10A MCB	10A SP MCB

C. Determination of Heat Transfer to the Environment

To calculate the heat transfer through the walls more accurately, it is decided to divide the lateral walls into six different regions when calculating the convective heat transfer coefficient, h, which are illustrated in Figure C.1.

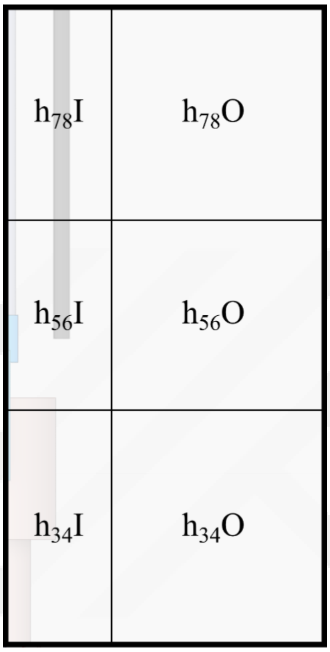

Figure C.1 Patching the outer surface of cavity walls for local convective heat transfer coefficient determination

h profiles derived from the Eqn. (3.8) are presented as charts in Figure C.2 2, region by region. For example, $h_{34}I$ is assigned for the region that encompasses planes 3 and 4. “I” represents the inner part of the wall, whereas “O” represents the outer part of the wall.

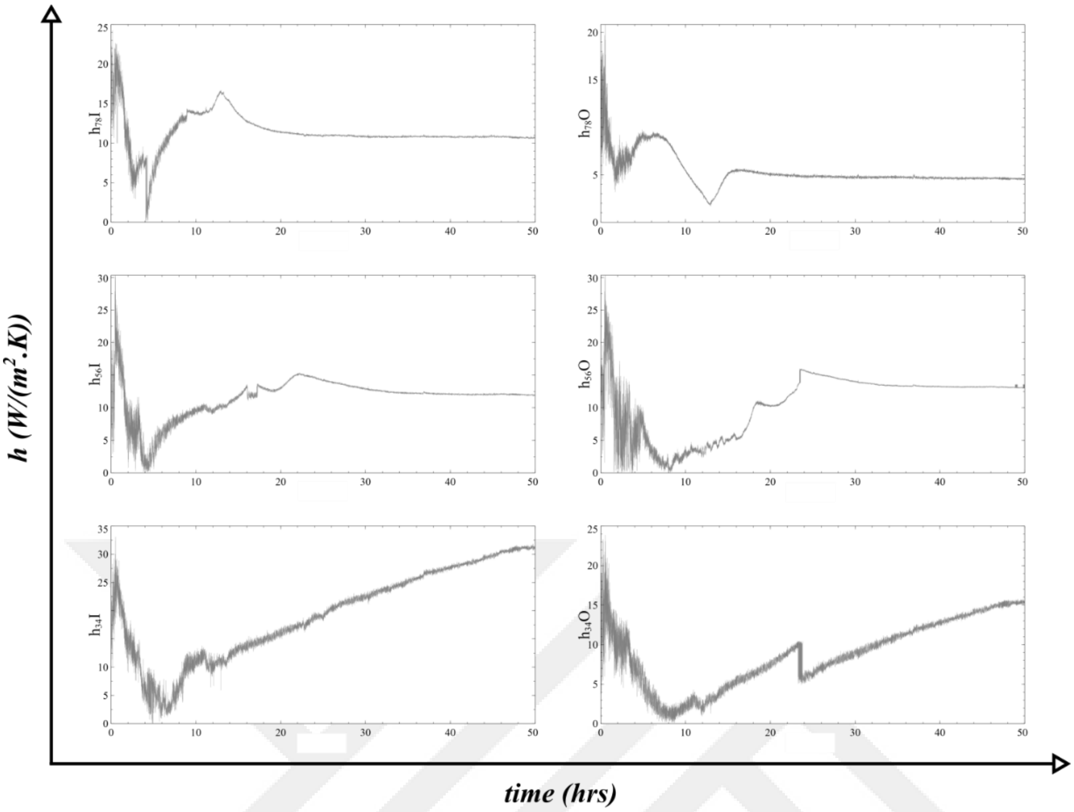

Figure C.2 Time-dependent convective heat transfer coefficient variation on the outer surface of cavity walls

Since the temperature on the inner side of the cavity stays low during the first five hours for the $_{34}$I region, the temperature of the outer wall adjusts more easily (8.5 hours in $_{34}$O). As a result, in some cases, h is nearly zero. Afterwards, the temperature of the PCM increases rapidly, making it difficult for the temperature of the outer wall to adapt. The h peaks approximately when the melt front contacts the wall. After this point, the heat transfer coefficient remains relatively steady until the end of the experiment.

It is worth noting that the humidity is controlled by a fan inside the experiment room, and the velocity of the ambient air is monitored using an anemometer, which records a maximum velocity of 0.1 m/s during the experiment. As a result, this ensures the accuracy of the coefficients for the convective heat transfer rate through the walls. The temperatures of the upper and lower walls are monitored. Table C.1 presents the convective heat transfer coefficients for the top and bottom walls, designated as h_{top} and h_{bottom}, respectively.

Table C.1 Time-averaged convective heat transfer coefficients of the top and bottom walls

Convective heat transfer coefficient	Process	Value $(W/(m^2.K))$
h_{top}	Non rotating	7
	Rotating	5
h_{bottom}	Non rotating	9
	Rotating	8

CURRICULUM VITAE

PERSONAL INFORMATION

Surname, Name: Farshineh Adl, Houman

EDUCATION

Degree	Institution	Year of Graduation
MS	University of Tehran Energy Systems Engineering	2019
BS	Sharif University of Technology Mechanical Engineering	2016
High School	Alborz High School, Karaj, Iran	2011

WORK EXPERIENCE

Year	Place	Enrollment
2023 – Present	Stadia Engineering Company	Project Engineer
2022 – 2023	ITAS – Intelligent Systems	Analysis Department Team Leader
2021 – 2022	Europower Energy Company	Design Engineer
2020 – 2021	Middle East Technical University (METU)	Early-Stage Researcher
2018 – 2018	Siemens AG	Marketing Intern
2016 – 2018	Tehran Air Quality Control Company	Air Pollution Specialist

FOREIGN LANGUAGES

Advanced English, Native Persian, Turkish, and Azeri

PUBLICATIONS

CONFERENCE PAPERS

1- Houman Farshineh Adl, Younes Noorollahi, and Aziz Aghazadeh. "Design and Simulation of Shrouded Wind Turbine." 24th Electrical Power Distribution Conference, Khoram Abad, Iran.